5-2017

Mechanical Behavior of a Bio-Inspired Chondrichthyan Feeding Mechanism: Influence of Dentition Patterns

Garrett Hall
Clemson University, gjhall@g.clemson.edu

MECHANICAL BEHAVIOR OF A BIO-INSPIRED CHONDRICHTHYAN FEEDING MECHANISM: INFLUENCE OF DENTITION PATTERNS

A Thesis
Presented to
the Graduate School of
Clemson University

In Partial Fulfillment
of the Requirements for the Degree
Master of Science
Mechanical Engineering

---

by
Garrett Hall
May 2017

Accepted by:
Dr. Michael Porter, Committee Chair
Dr. Richard Blob
Dr. Suyi Li

ABSTRACT:

Despite the relative compliance of cartilage compared to bone, many chondrichthyans are capable of thriving at a variety of extremes, including: living in high-pressure environments, supporting massive body weights and muscular loads, or feeding on hard-bodied prey. Although there is extensive literature on shark feeding mechanics, cranial anatomy, and tooth structure and function, questions still surround the structural foundation of the chondrichthyan feeding mechanism in polydontic models. Consequently, the efficacy of shark jaws to withstand loads experienced during feeding is a topic of interest among biologists and engineers alike. Polydontic bio-inspired models were developed through additive manufacturing and tested in bending and compression, and the stress distribution through each was approximated to investigate the structural significance of different dentition patterns. This study could provide further insight into design elements in biological systems and their influence on the mechanical behavior through a novel investigation of a rigid staggered element pattern. The results of this research reveal the potential utility of the system with flexible armor engineering applications. We hypothesized that our results would reveal a common theme in biological systems; the staggered dentition patterning in the chondrichthyan jaws will provide an increase in rigidity that is demonstrated by the overlapping elements found in other biological systems, such as abalone nacre, mineralized collagen fibrils, and multilayered silica glass sponges. However, our results proved otherwise. While factors such as tooth depth and file spacing had an influence on the stiffness of the system, the dentition patterning had a minimal impact.

ACKNOWLEDGEMENTS:

I would like to thank Dr. Michael Porter for his guidance and support throughout this research. I would like to thank Dr. Mason Dean from the Max Planck Institute for Colloids and Interfaces for his knowledge and input related to the biology of shark jaws and Maria Laura Habegger of the Florida Fish & Wildlife Research Institute for providing the bonnethead shark jaw sample that we used for our modeling. I would like to thank Tim Pruett of Clemson University for his assistance with additive manufacturing and for printing all of the models that were used during testing. I would also like to thank Travis Pruitt of the Godley-Snell Research Center for allowing access to and assisting with micro-CT scans. Finally, I would like to thank the other members of the Natural Engineering Lab Pooya Niksiar, Nakul Ravikumar, and Justin Holt for their support and assistance throughout the research.

TABLE OF CONTENTS:

Page

TITLE PAGE i
ABSTRACT ii
ACKNOWLEDGEMENTS iii
LIST OF FIGURES vi
LIST OF TABLES ix
1. INTRODUCTION 1
1.1 BIO-INSPIRED DESIGN 2
1.2 STAGGERED PATTERNS IN NATURE 3
1.3 RESEARCH MOTIVATION 6
2. BACKGROUND ON CHONDRICHTHYES 8
2.1 FEEDING MECHANISM 10
2.2 COMPONENT MATERIAL PROPERTIES 18
3. METHODS AND MATERIALS 21
3.1 THREE-DIMENSIONAL MODELING OF A SHARK JAW 21
3.2 MATERIAL SELECTION 39
3.3 MODEL PRINTING 43
3.4 MODEL TESTING 46
3.5 MODULUS APPROXIMATION 54
3.6 THEORETICAL STIFFNESS CALCULATIONS 61
4. RESULTS AND DISCUSSION 69
4.1 ANATOMICAL CROSS-SECTION MODEL RESULTS 69
4.2 RECTANGULAR MODEL RESULTS AND DISCUSSION 72
5. CONCLUSIONS 86
5.1 IMPACT OF RESULTS 87

TABLE OF CONTENTS (CONTINUED):

Page

5.2 IMPACT OF TESTING PARAMETERS 91
5.3 IMPACT OF MODELING METHODS 93
5.4 INTELLECTUAL MERIT 94
5.5 BROADER IMPACT 94
5.6 FUTURE WORK 96
REFERENCES 100

LIST OF FIGURES:

Page

Figure 1 4
Figure 2 5
Figure 3 9
Figure 4 11
Figure 5 12
Figure 6 13
Figure 7 14
Figure 8 15
Figure 9 17
Figure 10 18
Figure 11 22
Figure 12 22
Figure 13 23
Figure 14 23
Figure 15 24
Figure 16 25
Figure 17 27
Figure 18 28
Figure 19 29
Figure 20 31
Figure 21 33
Figure 22 33
Figure 23 35

LIST OF FIGURES (CONTINUED):

Page

Figure 24 37
Figure 25 38
Figure 26 38
Figure 27 39
Figure 28 44
Figure 29 45
Figure 30 46
Figure 31 47
Figure 32 47
Figure 33 50
Figure 34 51
Figure 35 52
Figure 36 55
Figure 37 56
Figure 38 63
Figure 39 64
Figure 40 65
Figure 41 68
Figure 42 69
Figure 43 70
Figure 44 73
Figure 45 74

LIST OF FIGURES (CONTINUED):

Page

Figure 46 77

Figure 47 78

Figure 48 80

Figure 49 81

Figure 50 84

Figure 51 96

Figure 52 98

LIST OF TABLES:

Page

Table 1 19

Table 2 34

Table 3 36

Table 4 40

Table 5 53

Table 6 61

Table 7 65

Table 8 66

1. INTRODUCTION

Increased demands for improved performance requirements is a continual process that steers research for lighter, tougher, and stronger materials [1]. Years of research have gone into this topic, and while advances have been made, it appears that many structural materials are approaching their performance limits [2]. An impasse has been reached in which simple monolithic materials are no longer capable of meeting the ever increasing structural performance demands. Consequently, material scientists and engineers have shifted their focus more toward composite material systems. These composites can combine materials with a series of desired properties that can behave in a synergistic manner [1]. When the appropriate materials are utilized in a composite system with an optimized structural arrangement, the composite material will outperform the sum of its parts [2]. This opens up a whole new design space and introduces a range of new variables that can be manipulated to optimize the composite, such as combinations of materials, sizes, geometry, and patterning. Typically, one must trade strength for toughness or vice versa; however, these composite systems allow soft deformable materials to be coupled with hard, brittle materials to generate unique blends of strength and toughness that can be tailored to the desired purpose [1,2]. Tightly governing the microstructure of the system regarding geometry, size, and the arrangement has an enormous influence on the structural performance of composite materials and has been a major research focus [1].

1.1 BIO-INSPIRED DESIGN

A growing interest in biomimicry and bio-inspired design has sparked research in biological systems for advanced materials and structural devices [3-5]. Nature and biology have strongly emerged as primary sources of inspiration in recent years for advanced materials research. This applies in particular to the development of novel synthetic structural composites, as many biological systems are fundamentally composed of composite structures [6]. The complex and intricate construct of natural materials serves as a principal source of inspiration for bio-inspired research as it relates to advanced materials and structural components. These qualities allow for the creation of lightweight and cost-effective components that offer an array of mechanical properties that surpass those of simple polymeric, metallic, or ceramic constituents by sometimes several orders of magnitude [2,5-7]. Within these complex constructs, it is the architecture of the materials at varying lengths of scale that is of particular interest [1,2]. The architectures found in natural materials combine constituents in intricate orientations ranging from the nano- to macro-scale. This myriad of possibilities for building blocks on a full spectrum of scales maximizes the potential properties of the system and allows the system to respond to or withstand external stimuli more efficiently [2,6,8].

To further understand the influence of design elements in biological systems, it is necessary to understand the elements responsible for the desired mechanical properties. There is no comprehensive list of design elements, as individual researchers may tend to have their own categorizations of design elements and tend to group the information based on their own definitions [1,2,6,8]. Nonetheless, design elements may consist of material

structures like cellular, fibrous, helical, tubular, layered, and gradient structures, or joints like sutures (interlocking elements) and overlapping interfaces [1,8]. An additional design element of particular interest for this research is the staggered rigid element pattern. It is common for organisms with structures comprised of different materials to utilize the same design elements to achieve the same mechanical advantage [8]. Therefore, we are trying to expand upon this to see if a staggered rigid element pattern will produce the same effect as an overlapping design element. Therefore, a few other systems will be discussed before investigating the staggered rigid element pattern in the chondrichthyan feeding mechanism.

1.2 STAGGERED PATTERNS IN NATURE

A staggered pattern of relatively hard structural units embedded in a softer substrate is frequently studied due to its nature of combining relatively weak constituents to form dramatically more tough and stiff composite systems [2,4]. Strength and toughness are a requirement in almost all structural materials, yet tend to be mutually exclusive. This is why the overlapping design element has received so much attention [9]. It has been found on the nano- and micro-scale that the overlapping configuration brings about unique stiffness and toughness properties within a composite system [10]. This occurs in two ways. First, soft components may be inserted into stiff layers to increase toughness and stop crack propagation. Contrarily, stiff segments may be inserted into a softer base to increase stiffness, as will be studied in this research.

Nacre has become one of the most studied bio-composites and is one that has garnered a lot of attention recently due to the tough, strong, and lightweight nature of its

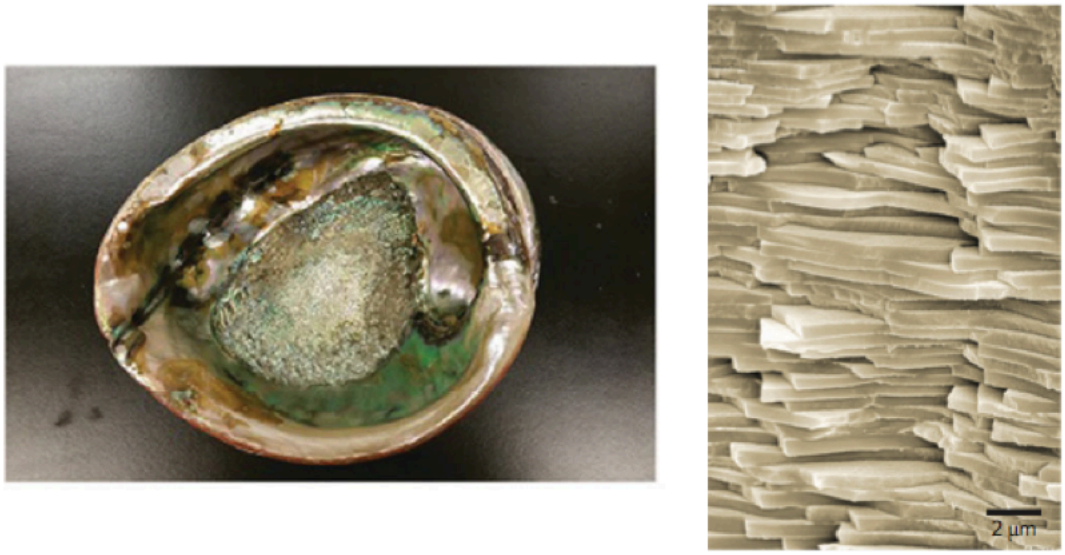

Figure 1: An abalone shell and the brick-and-mortar structure of the aragonite platelets found in abalone nacre [2,8].

overlapping structural design [11,12]. Nacre typically forms the inner layer of oyster, mussel, or abalone shells. It is a highly mineralized material that is 95 vol.% aragonite ($CaCO_3$) platelets that are ~0.5 μm thick and ~5-10 μm wide [1,2,9,13]. The aragonite presents a mineralized structure that is high in strength and toughness [1,9]. The platelets are accompanied by a softer organic layer comprised of chitin and acidic proteins that absorb local stresses and acts as a means of stress redistribution, subsequently increasing the overall toughness of the inherently brittle mineral [1,9,12-14]. The aragonite platelets and organic material are arranged into a complex architecture that spans multiple lengths of scale [15]. They are staggered in both the length and width direction to form the brick-and-mortar structure that can be seen in **Figure 1** [9,10]. The combination of materials and the staggered structural design element creates a very stiff and hard structure with a toughness that is many orders of magnitude greater than its constituents [1,2,12-14].

Compact bone is another natural material that presents a structure and toughening mechanism that is comparable to nacre [1]. Bone has a complex staggered structure of collagen fibrils that give it a unique blend of strength, toughness, and stiffness [1,2]. Its microstructure is designed with enhanced toughness and reasonable stiffness to withstand cyclic impact loading; whereas, nacre is designed to withstand constant hydrostatic pressure and attacks from predators, so it has a greater emphasis on stiffness. This demonstrates how nature can utilize the same design element and just vary the materials and their ratios to make small adjustments to the performance of the bio-composite [11]. However, this staggered design element is not limited to these two systems. In fact, it is found throughout a number of other biological systems. It is present in tooth dentine tubules [8,10], mineralized collagen fibrils [1,2], multilayered silica glass sponges [17], the carapace of certain insects [8,20], and abalone nacre [8,10,18], some of which can be seen

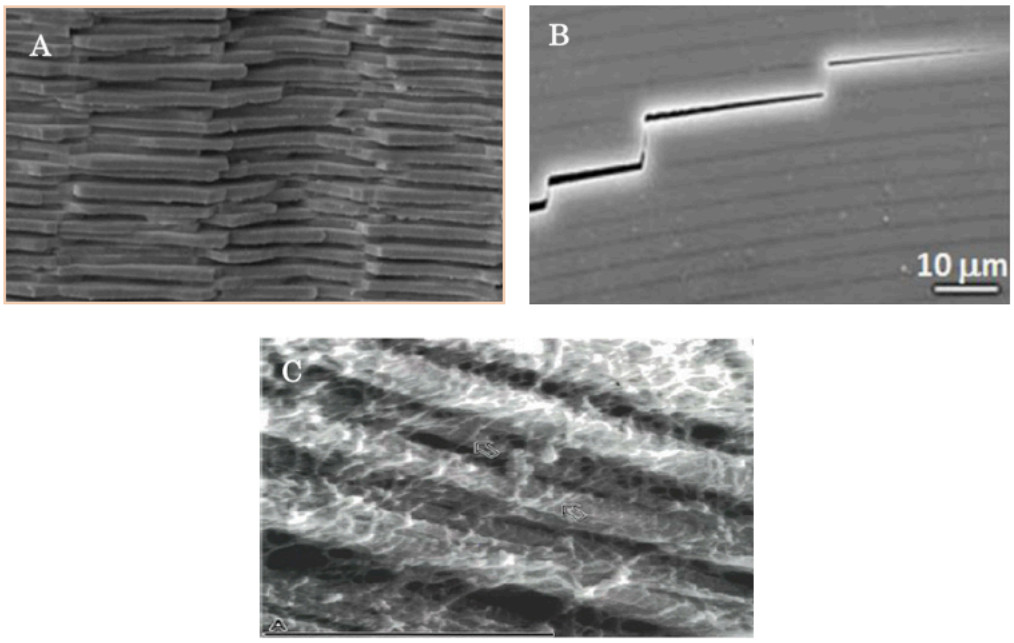

Figure 2: The overlapping structural design element in different biological systems. **A:** Abalone nacre **B:** Multilayered silica glass sponge **C:** Mineralized collagen fibrils [1,8,10]

in **Figure 2** [1,8,10,16-22]. This speaks greatly to the utility and versatility of this arrangement. This one structural design element has been incorporated throughout the animal kingdom in all types of environments to accomplish the common goal of influencing the stiffness, strength, and toughness of bio-composites.

1.3 RESEARCH MOTIVATION

When investigating mechanical properties, the full range of length scales from nano- to macro- must be considered to prevent limiting the possible contributing factors and to find the local optimum for a set of constraints [2]. However, in the study of many biological systems, the length scale between the nano/micro-scale and the macro-component scale is often overlooked, but contributes significantly to a system's performance. This characteristic millimeter length scale often requires concepts from both mechanical engineering and material science; it may be referred to as the study of architecture materials. By one definition [1], architecture materials lay within the 100 μm – 100 mm range and are smaller than the component yet larger than the microstructure. One of the significant challenges associated with producing synthetic composites that compare with natural materials is the difficulty related to replicating the complex nano- and micro-structures of the system [6]. Modern nanoscale manufacturing techniques are overcoming some of these issues; however, further researching in the area of architecture materials could have a more immediate and direct impact on practical applications due to ease of replication and manufacturing at this scale [8].

These factors led to the following research on chondrichthyan dentition patterns. It is an effort to bridge the knowledge gap between the component level (feeding mechanism) and microstructure level (tesserae) in chondrichthyan research by investigating its structural design elements at an intermediate level. There have been vast amounts of chondrichthyan research performed at the micro- and macro- levels [23-37], yet little research has been performed at this intermediate range. Some chondrichthyans possess staggered dentitions, which may create a stiffening effect on the feeding mechanism. We hypothesize that the staggered dentitions serve the same purpose as the staggered structural design elements found in abalone nacre and the mineralized collagen fibrils found in bone [8]. Many studies have investigated the structure-function relationships of biological composites; however, this study is taking a new approach. It investigates a bio-inspired design element in the form of a rigid staggered element pattern in a three-dimensional (3D) printed composite material. It is our hope that this research will provide a more macro-level representation of the staggered structural design elements mentioned above and likewise improve stiffness and toughness in the system. Subsequently, this could allow for a more efficient means of incorporating the staggered structural design element into engineered systems.

2. BACKGROUND ON CHONDRICHTHYES

Chondrichthyes are a class of fishes, including sharks, skates, rays, and chimaeras, that possess a cartilaginous skeleton that is maintained throughout their lifetime, unlike other vertebrates whose embryonic cartilaginous skeletons convert to bone as they mature [23,38]. Nonetheless, these fish are capable of functioning at a variety of extremes including: growing to extreme sizes, surviving at extreme depths with exceptionally high pressures, and consuming foods with exceptionally hard components [24]. Chondrichthyes are among some of the largest and fastest animals in the ocean and have the ability to feed on hard-shelled and larger prey. In addition, the cartilaginous jaws of these fishes are cyclically loaded up to 10^{10} times over a lifetime [39]. The jaws cannot afford to fail due to their inability to self-repair because the cartilaginous tissue lacks vasculature [39-41]. Consequently, fracture resistance is of the utmost importance [38-41]. The cartilaginous tissue of chondrichthyans primarily consists of hyaline cartilage partially calcified into mineralized blocks known as tesserae [23-38]. The orientation of regions of calcified tesserae prisms interrupted by regions of uncalcified cartilage associated with the jaws of chondrichthyans is believed to provide three main advantages: support, flexibility, and provide for growth without the need for continuous remodeling [25,42].

Elasmobranchii is a subclass of chondrichthyes, under which sharks, the primary focus of this study, are classified [24,26]. Elasmobranchs are polydonts, meaning they have multiple rows and files of teeth [24,38]. These teeth lay within a thick connective tissue sheet composed mostly of collagen and do not directly contact the underlying surface of the jaw [38]. The tooth attachment is thus flexible and elastic [27], which allows for

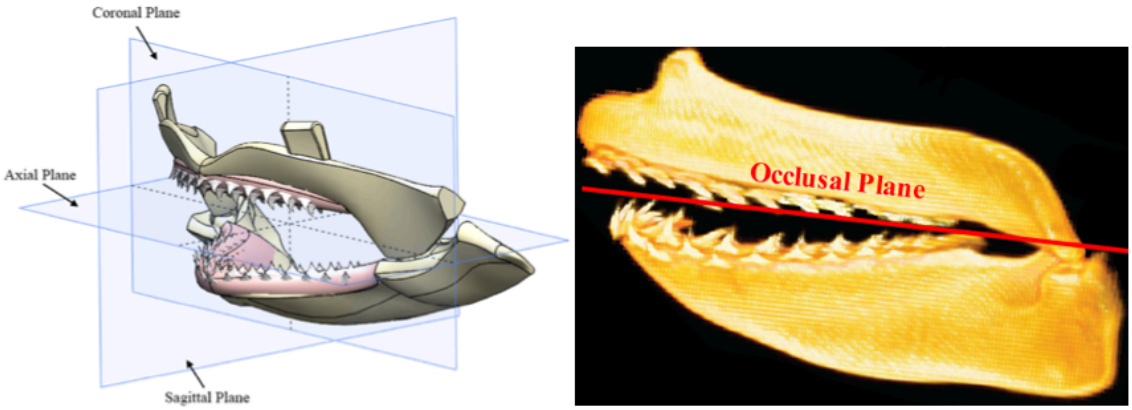

Figure 3: Anatomical reference planes in relation to chondrichthyan jaws. [44,45, Image Courtesy of Mason Dean]

movement of the teeth in the coronal and sagittal planes, providing a mechanism to replace teeth lost from the functional layer [27,38]. The cartilaginous jaws of sharks form the basis for their feeding mechanism, yet calcified vertebral bone is inherently more stiff as compared to chondrichthyan cartilage [28, 43]. Consequently, this raises questions regarding the efficiency of the chondrichthyan feeding mechanism (jaw, dental ligament, and files of teeth) to withstand certain loads. Based on this information, it becomes important to investigate the influences of comparatively compliant cartilage, when compared with vertebral bone, and determine the factors that contribute to the effectiveness of the feeding mechanisms of elasmobranchs [28]. Numerous studies have investigated the feeding mechanism of chondrichthyans, including: the analysis of the tessellated jaw cartilage [24,30], muscles function [28], and bite force mechanics [25,28,31] among others [29]. However, very little work has focused on how the patterning of teeth may affect the mechanics of a jaw. Dietary and feeding studies that have investigated elasmobranch teeth have mainly focused on single tooth models [25,29,32]. While this may be acceptable for

establishing general feeding behavior and classifying dentitions, it excludes interactions that occur between teeth during feeding. Consequently, there exist no polydontic models for the mechanical behavior of the elasmobranch feeding mechanism that include the effects of tooth-tooth interactions. That is the topic of this thesis: investigating the mechanical behaviors of different dentition patterns on composite jaw-inspired models.

2.1 FEEDING MECHANISM

The feeding mechanism performs a vital role in the survival of chondrichthyans [25]. It is a unique and inspiring system that is more than a simple resting place for the fishes' dentitions. It is a dynamic system that is capable of withstanding cyclic loading under extreme conditions, while continuously replacing functional teeth to remain in peak working condition. There are three primary components found within the feeding mechanism: teeth, dental ligament, and cartilaginous jaw. While previous studies have investigated the structure and function of various aspects of the feeding mechanism, the field is still lacking in research surrounding the collective influences of the teeth within the feeding mechanism [24, 25, 28-31].

2.1.1 TEETH

The dentitions of chondrichthyans possess a flexible and elastic tooth attachment within the dental ligament, as can be seen in **Figure 4** [27], that allows for movement in the sagittal and coronal planes. This means that the dentitions of chondrichthyans reside

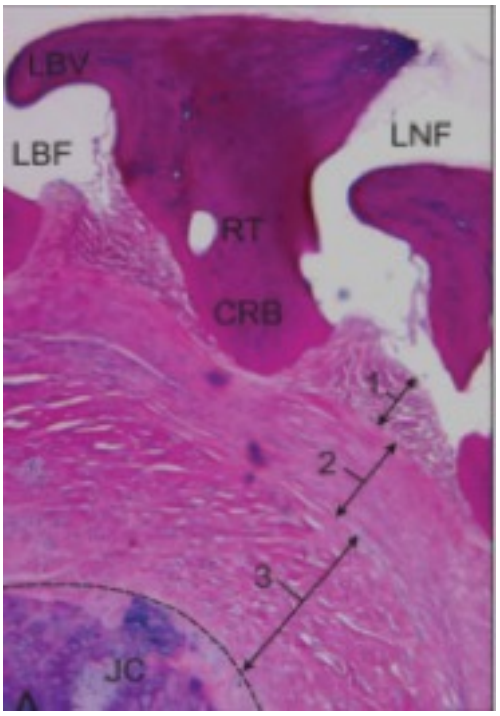

Figure 4: Cross-section of the feeding mechanism from a whitespotted bamboo shark (*Chiloscyllium plagiosum)* specimen. This image shows a tooth embedded within the first of the three dense connective tissue layers of the dental ligament. This clearly shows the separation between the teeth and the jaw cartilage. CRB, central root base; JC, jaw cartilage; LBF, labial face; LBV, labial visor; LNF, lingual face; RT, root; 1, superficial layer of dental ligament; 2, middle layer of dental ligament; 3, deep layer of dental ligament [27].

within the dental ligament and possess no direct contact to the underlying tessellated jaw cartilage. Rather, an indirect fibrous attachment is responsible for anchoring the teeth in the feeding mechanism [27, 33, 34,46]. One of the primary functionalities of this flexible tooth attachment is for the continual replacement of teeth as the chondrichthyan grows and ages. The teeth progress from a lingual to a labial position until they reach the functional layer of teeth (functional teeth are the outermost teeth that are erect and possess a fully mineralized root [32]), as can be seen in **Figure 5**. All the while, the teeth mineralize and mature to form the final functional tooth. This continuous replacement of teeth serves to

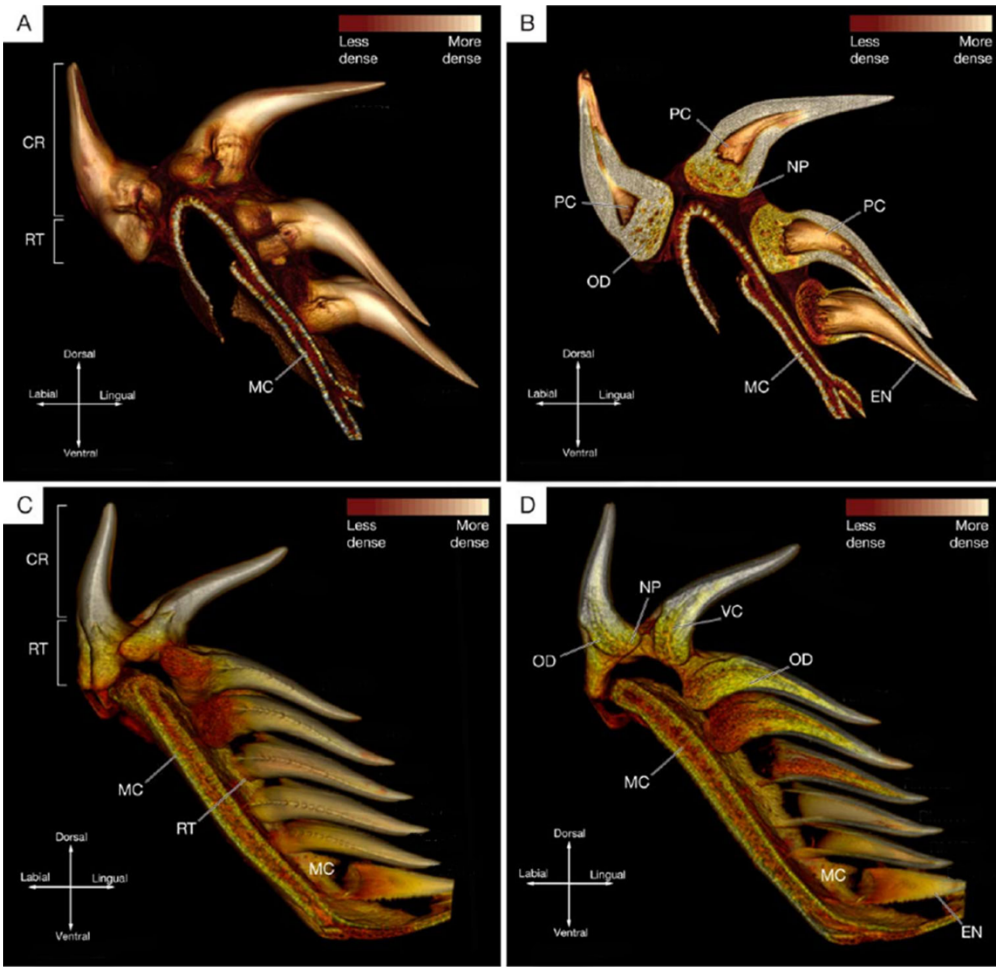

Figure 5: CT-scan renderings of a blue shark (*Prionace glauca*) and white shark (*Carcharodon carcharias*). Each image shows a single file of teeth and provides insight into the different stages of tooth growth and mineralization. **A:** This image shows the stages of root and crown development in the blue shark. **B:** Digitally sectioned view to show the mineralization occurring in the crown of the tooth in the blue shark. **C:** This image shows the stages of root and crown development in the white shark. **D:** Digitally sectioned view to show the mineralization occurring in the crown of the tooth in the white shark. CR, crown; EN, enameloid; MC, Meckel's cartilage (jaw cartilage); NP, nutritive pore; OD, osteodentine; PC, pulp cavity; RT, root; VC, vascular canal [32].

provide a continuous supply of new teeth to replace worn, damaged, or lost teeth in the functional layer and is a process that exists at variable rates among different species [32, 33, 36, 46]. During feeding, elasmobranch teeth may potentially encounter tremendous loads. To withstand these loads, the teeth must be strong enough to resist breaking until

they are shed from the functional layer [29]. When in contact with hard, impenetrable prey, the flexible attachment allows the teeth to passively depress and rotate inward in the direction of the oral cavity [27, 34, 35]. This produces a crushing surface by allowing the broader labial face to contact the prey rather than the point of the tooth. Consequently, this same attachment mechanism provides the ability for dentitions in certain shark species to become erect during the capture of prey, enabling better tooth penetration [27, 34, 35]. The proposition has also been made that the flexible tooth attachment may provide the ability for lateral teeth to shift within the tissue of prey to prevent the hindrance of the cutting action created by the anterior teeth during head shaking [27]. Thus, the means of attachment and replacement mechanism of elasmobranch dentitions has the potential to cross-over into the versatility of its functionality that heightens its ability to process prey [33].

According to Whitenack et al. [29], there are six major dentition types found in chondrichthyans, as seen in **Figure 6**: clutching, tearing, cutting, crushing, grinding, and

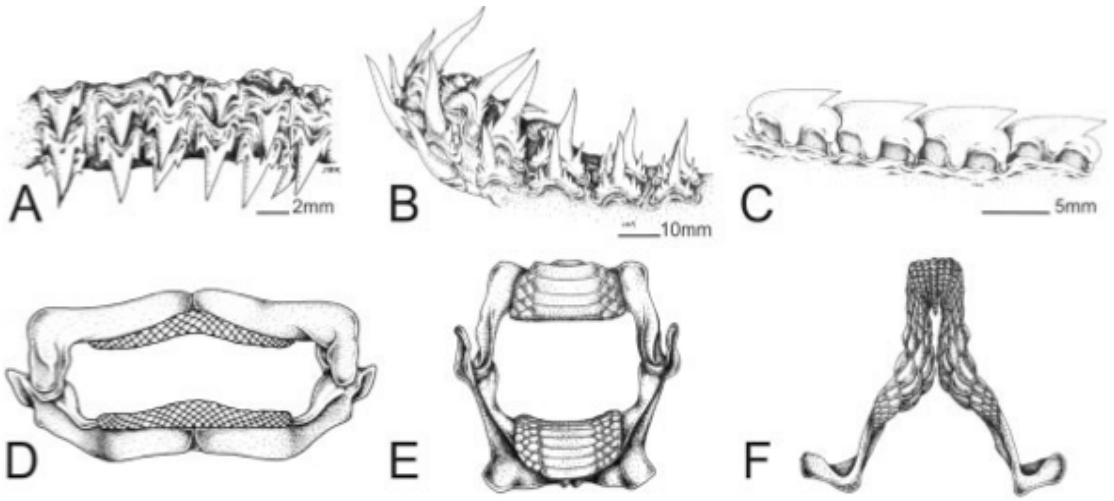

Figure 6: Morphologies of chondrichthyan dentitions. **A:** Clutching **B:** Tearing **C:** Cutting **D:** Crushing **E:** Grinding **F:** Clutching-grinding [27]

clutching-grinding. Chondrichthyan tooth morphology is believed to be evolutionarily dependent upon the stresses imposed by feeding on various types of prey. Consequently, this tooth morphology has conventionally been used as a sign of prey selection [27, 32, 37]. Many anatomical and dietary/feeding studies have drawn conclusions that support this correlation between the tooth form and prey type in many chondrichthyans [25, 27].

The teeth of sharks form a composite structure comprised primarily of mineralized calcium and phosphate [47]. This composite structure consists of three potential materials in variable amounts: enameloid, orthodentine, and osteodentine [29, 32, 48, 49]. There are two arrangements of mineralized tissues found in the dentitions of elasmobranch fishes, orthodont and osteodont found in **Figure 7** [32]. While some debate remains surrounding this topic, it is traditionally specified that orthodont dentitions retain their pulp cavity during tooth development and progression toward the functional layer, while the functional

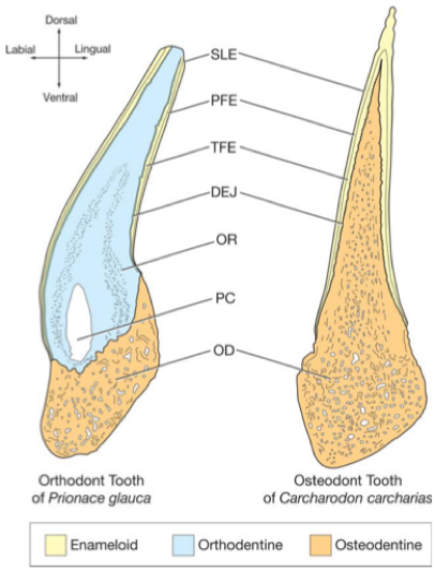

Figure 7: Depiction of orthodont and osteodont histotypes. OD, osteodentine; OR, orthodentine; PC, pulp cavity; PFE, parallel-fibered enameloid; SLE, shiny layer enameloid; TFE, tangled-fibered enameloid; DJE, dentine-enameloid junction [32].

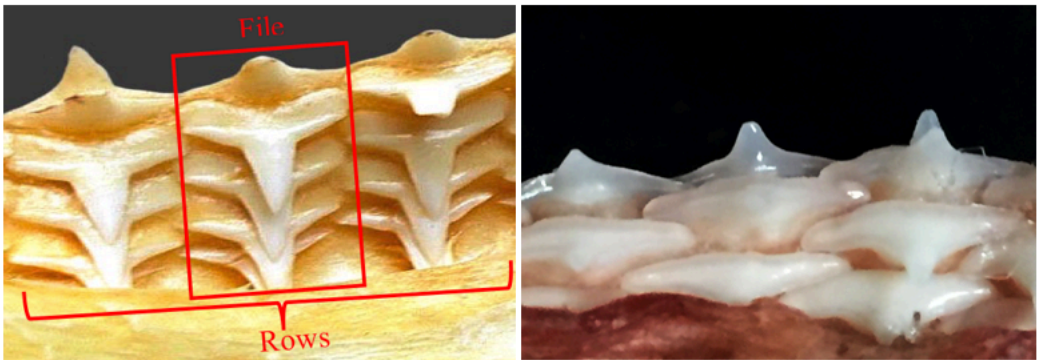

Figure 8: Left: The accepted nomenclature for referencing files and rows of teeth within the jaws of chondrichthyans on a parallel dentition pattern in a bull shark (*Carcharhinus leuca)*. **Right:** Staggered dentition pattern in a bonnethead shark (*Sphyrna tiburo)*.

layer of osteodont dentitions lacks a pulp cavity [29, 32, 48, 49]. The enameloid crown is the first element of the tooth to develop, and it reaches its maximum thickness early in the development process. The osteodentine and orthodentine are slower to mineralize and occur throughout the tooth's labial movement toward the functional layer [32]. The crown of the tooth may be composed primarily of orthodentine (orthodont) or osteodentine (osteodont), but it always possesses an outermost enamel covering [29].

Shown in **Figure 8**, rows of teeth run horizontally while files of teeth run from a lingual to labial position with the number of teeth per file varying among species [27, 32]. The files of teeth are present in a series that exists with the lesser developed teeth in the lingual-most position that progressively develop and move toward the occlusal plane during tooth ontogeny until reaching the functional layer at the labial-most position. This lingual to labial progression of teeth as they develop allows for the continuous replacement of worn or damaged teeth in the functional layer at variable rates between species [32, 33, 36, 46]. The arrangement of files of teeth in different species of sharks is of particular interest and a topic of focus in this thesis. The files may be completely parallel, or they

may be staggered to varying degrees. Since little research has been done on polydontic chondrichthyan jaw models; the influence of the file patterning on the mechanical properties of the feeding mechanism remains unclear.

2.1.2 DENTAL LIGAMENT

The dental ligament is a dense connective tissue layer that is composed primarily of collagen fibers. This connective tissue tends to be divided into distinct layers with different thicknesses, orientations, and arrangements of the fibers [27]. Within the *Chiloscyllium plagiosum* species, as seen in **Figure 4**, the dental ligament is divided into three distinct layers. The superficial layer has a variable thickness with irregular bundles of collagen fibers [27]. This layer is often referred to as the tooth bed or sub-odontal layer [42]. These irregular fiber bundles are similar to Sharpey's fibers found within mammalian bone and act as indirect fibrous attachments that retain the teeth in the feeding mechanism [27, 42]. Deep into this layer is a region of dense collagen fibers that runs parallel to the basal surface of the tooth and the jaw cartilage. This layer has a more uniform thickness and fiber orientation. The deep layer is known as the supra-tessral layer. This final layer of irregular collagen fibers is continuous with both the middle layer and the perichondrium of the jaw [27,42].

2.1.3 JAW CARTILAGE

As noted above, the skeletons of chondrichthyans are purely cartilaginous, and it is referred to as Meckel's cartilage in the jaw [42]. This cartilage may be either calcified or

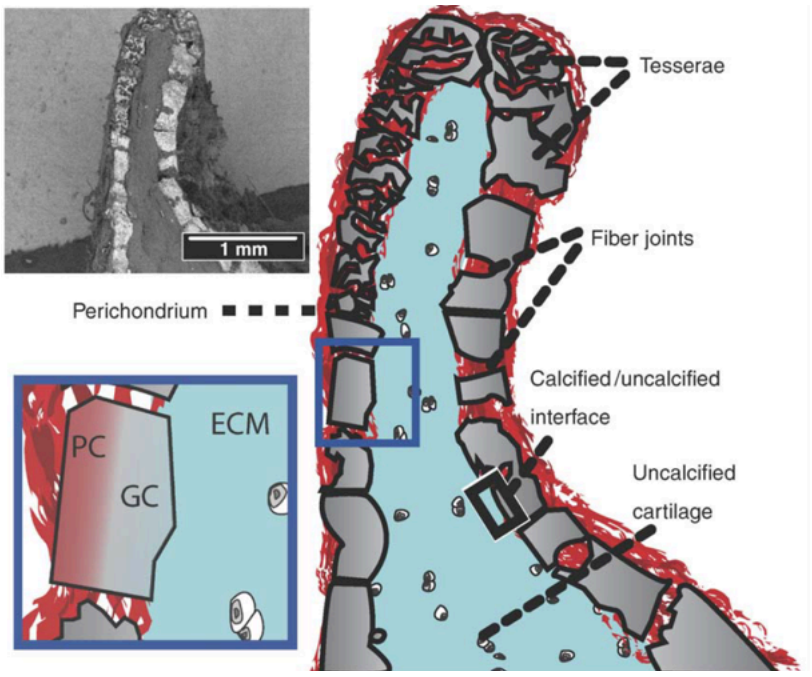

Figure 9: Mineralized tesserae overlying a core of uncalcified cartilage. The mineralized tesserae appear white in the upper left image. The lower left image shows an expanded view of the interface between the calcified and uncalcified cattilage. PC, prismatic calcification; GC, globular calcification; ECM, extracellular matrix (uncalcified cartilage); red fibers, fibrous perichondrium [23].

uncalcified, but chondrichthyans never possess a boney structure [42]. The cartilaginous endoskeleton has calcified morphologies that vary across species, prey type, age, and position on the body [23]. The cartilaginous skeleton is present throughout the life of chondrichthyans, separating them from other teleosts and higher order vertebrates [42]. The endoskeleton is comprised of small segmented blocks of calcified cartilage, called tesserae, overlaying unmineralized cartilage, as seen in **Figure 9** [23,42]. **Figure 10** shows the polygonal-shaped nature of mineralized tesserae [23,42]. These tesserae may vary in size and expand in all directions as they grow [42]. There are two forms of calcification, prismatic and globular, that occur simultaneously as the cartilage mineralizes to form the hydroxyapatite mineral component. The mineralization creates a continuous bridge

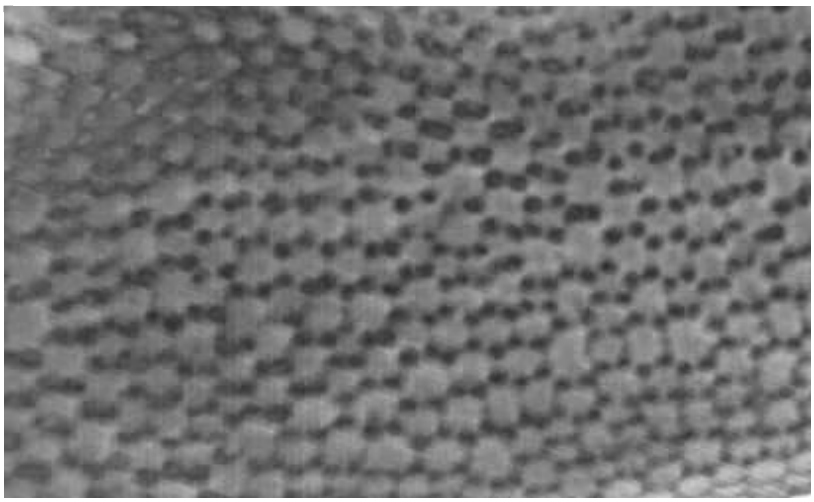

Figure 10: Micro-CT image showing the polygonal structure of the mineralized tesserae from a *Sphyrna tiburo* specimen. Image taken using the Bruker SkyScan 1176: High-Resolution *In-Vivo* Micro-CT.

between the perichondrium and the uncalcified core [23,42]. The presence of the tesserae and the uncalcified cartilaginous core are much less stiff than bone (with Young's' Moduli 4.05 GPa and 55.1 MPa respectively compared to 27.8 GPa for cortical bone), yet they provide enough rigidity to not significantly diminish their bite force during feeding [23,28, 42, 50, 51].

2.2 COMPONENT MATERIAL PROPERTIES

When studying the feeding mechanism, especially in regards to its material properties, the structure can be thought of as a composite system with the three aforementioned components: teeth, dental ligament, and jaw cartilage. Each of the components has very distinct material properties, and these properties vary significantly among species. The stiffness properties of each of these in turn are as follows.

The teeth themselves are a composite system composed of enameloid, orthodentine and/or osteodentine depending on the tooth type. Whitenack et al. [29] tested the hardness and Young's modulus of individual teeth from an orthodont and osteodont specimen; the results are displayed in **Table 1**.

Because of a lack of literature, data, and available specimens for experimental characterization, we used values provided by Chen et al. [52] for oral mucosa in *Homo sapiens* to approximate the stiffness of the dental ligament material. Oral mucosa has a similar multi-layered structure with similar orientation and collagen compositions to that of the chondrichthyan dental ligament. Chen et al. [52] found that the Young's modulus for oral mucosa is within the range of 0.9-1.1 MPa; these values were used to approximate the stiffness of the dental ligament in chondrichthyes.

In contrast, there are a number of studies investigating the mechanical properties of the cartilaginous jaws of chondrichthyes. Stiffness values for calcified tessellated cartilage range from 20.5 MPa – 4.05 GPa, and uncalcified cartilage from 12.16 MPa – 78.79 MPa, corresponding to approximately six different species [23, 24, 28, 37]. This is believed to be in part due to the variable collagen and proteoglycan content of the jaws. An increase in

Table 1: Hardness and modulus values for enameloid, orthodentine, and osteodentine. [29]

	***Sphyrna tiburo* (Bonnethead Shark)**		***Carcharias taurus* (Sand Tiger Shark)**	
	Orthodentine	Enameloid	Osteodentine	Enameloid
Hardness (GPa)	0.97±0.07	3.53±0.30	1.21±0.16	3.20±0.02
Young's Modulus (GPa)	22.49±1.72	68.88±1.50	28.44±2.21	72.61±4.37

the collagen content decreases the stiffness of the jaw. Likewise, an increase in collagen content decreases the proteoglycan content. Consequently, chondrichthyan jaws with higher collagen content have lower stiffness values [24].

3. METHODS AND MATERIALS

The methods used in this study included using computer aided design (CAD) to generate 3D models of feeding mechanisms with different dentition patterns, printing the models using a multi-material 3D printer, and then testing the printed models under quasi-static loading conditions. There were a number of reasons why 3D printed models were chosen for testing over natural jaw samples. First, by modeling the system in a CAD software, we were able to create an idealized model representative of the chondrichthyan feeding mechanism, which allowed for precise control over the independent variables. Moreover, creating our own models of the feeding mechanism allowed for the inclusion of variables that lay outside of the natural design space. This should provide a more complete understanding of why the variables exist as they do in nature and allow for the creation of an optimized model that can then be adapted for engineering applications.

3.1 THREE-DIMENSIONAL MODELING OF A SHARK JAW

To begin the modeling process, the NextEngine ScanStudio 3D Laser Scanner in **Figure 11** was utilized to obtain a general solid body outline of the jaw from a bonnethead shark. To scan the full jaw, two scans were necessary. The first scan was taken with the jaw positioned with the dorsal region on top and the ventral region on the bottom, and the second scan was taken at a 90-degree rotation as shown in, **Figure 12**. As the imaging platform of the NextEngine Scanner only rotates in a two-dimensional plane, the 90-degree rotation allowed for imaging of the dorsal and ventral regions of the jaw. Once the

Figure 11: NextEngine ScanStudio 3D Laser Scanner utilized to scan the jaw for the beginning of the 3D modeling process. Produced by NextEngine, Inc. in Santa Monica, California.

individual scans were complete, we used the ScanStudio software to fuse the two images and fill any minor holes and imperfections present in the model. Then, the models were exported to RapidWorks, a CAD software produced by NextEngine, for further modeling. In RapidWorks, a series of splines were sketched about the sagittal cross-sections to match

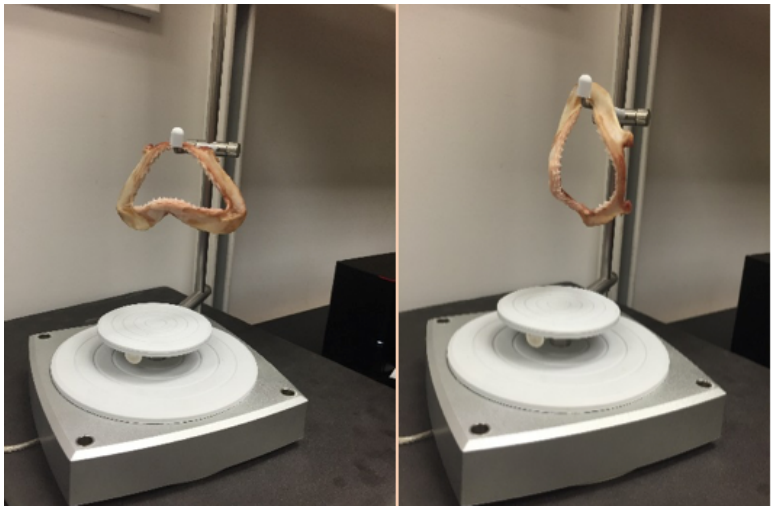

Figure 12: Left: the jaw is positioned for a scan with the dorsal region on top and the ventral region oriented on the bottom. **Right:** The jaw has been rotated 90-degress for a second scan.

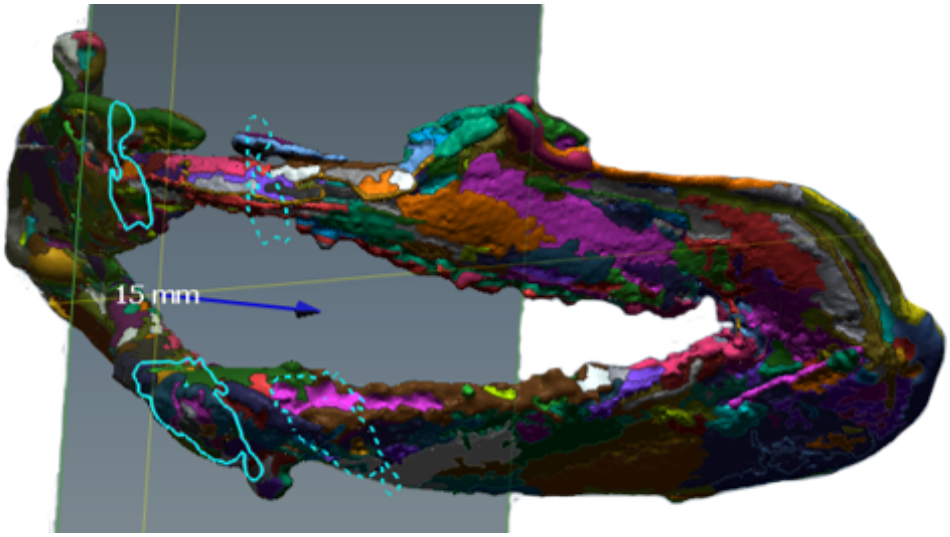

Figure 13: Extraction of cross-sectional sketches from the jaw model in RapidWorks at 5 mm increments.

the profiles. The sketches of the jaw were then taken from the model and exported to SolidWorks (Dassault Systems, Vélizy-Villacoublay, France), shown in **Figure 13**. We took cross-sectional sketches at 5 mm increments across the entire profile of the jaw. The center of the jaw was denoted as 0 mm, and the sketches ranged from ± 45 mm, with the

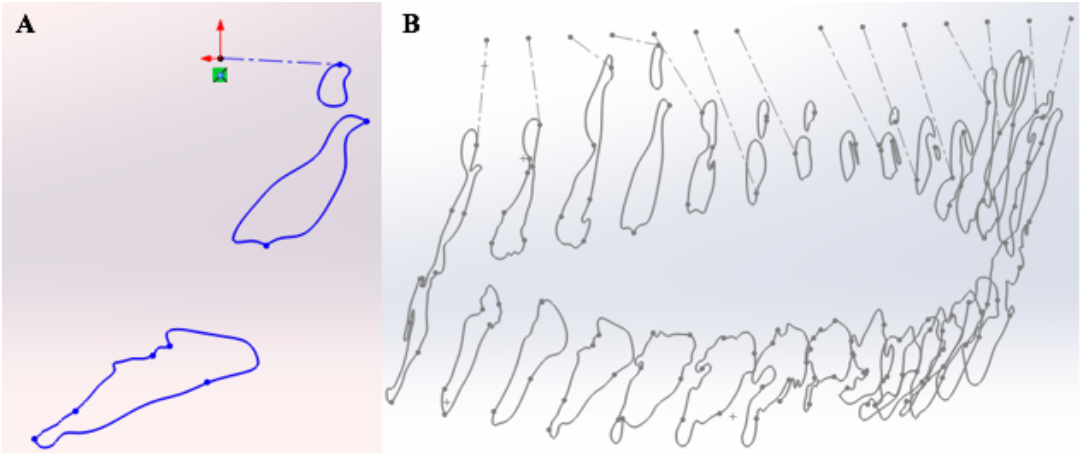

Figure 14: A: Aligning the sketch on the reference plane through the use of a guide line. **B:** All of the sketches after being imported into SolidWorks from RapidWorks.

anatomical right being positive, for a total of nineteen sketches. Each sketch was individually imported into SolidWorks and correctly positioned using a series of guidelines and reference planes in a process that can be seen in **Figure 14A**.

3.1.1 REPRESENTATIVE ANATOMICAL MODEL

After all sketches were placed and properly aligned into a single part file (**Figure 14B**), we divided the dorsal and ventral sections of the jaw into their own files, which allowed each section to be treated as independent models and facilitated the use of simpler, yet more precise methods. This modeling was an iterative process. The first generations of the models were crude, non-symmetrical, and possessed many sharp transitions. With the ultimate goal to create an idealized representative model of an "average" jaw, progressive simplification of the model through the use of guide curves was performed by lofting between sketches, mirroring components in the jaw for symmetry, and simplifying their geometries. To produce the final anatomical jaw structure, the original sketches were simplified by averaging 4-5 sketch landmark points, depending on the complexity of the

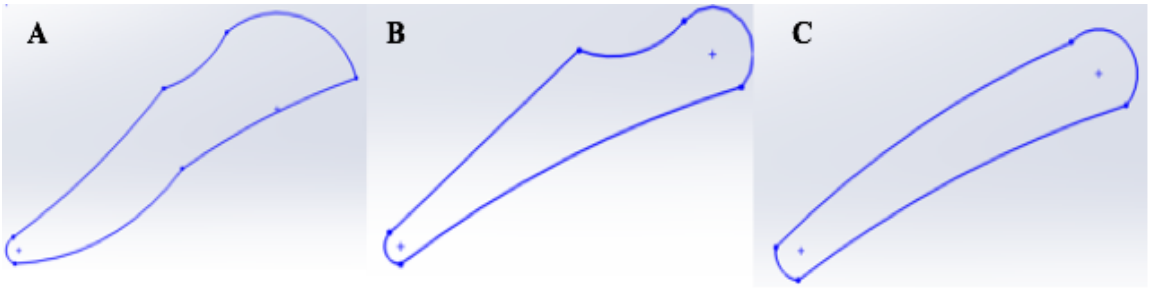

Figure 15: The progressive simplification of the sketch taken from the +25 mm position of the ventral jaw section. **A:** The original outline of the sketch. **B:** The sketch simplified to 5 sketch points. **C:** The final simplification of the sketch. The four sketch points were chosen at points of distinct geometric features.

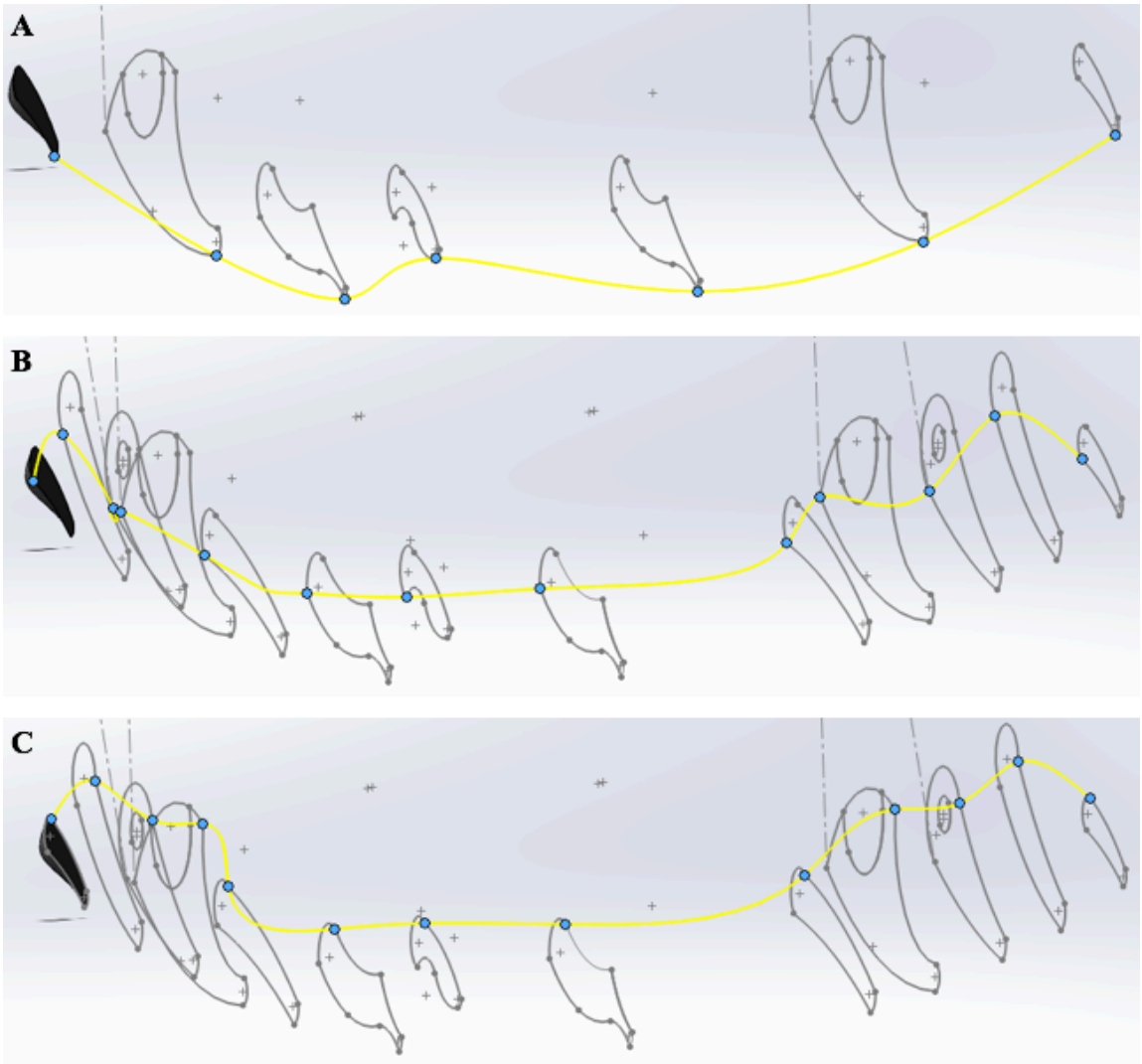

Figure 16: The three guide curves used for the ventral jaw section. **A:** This first guide curve runs along the lower anterior edge of the sketches. **B:** This second curve runs along the upper labial edge of the sketch. **C:** This guide curve runs along the upper lingual edge of the sketch.

native geometry (**Figure 15**). The sketches from the anatomical right of the jaw were mirrored to the left, creating a symmetrical jaw structure. Finally, the ventral and dorsal jaw regions were produced using a single loft for each region. The ventral region was bound by three guide curves. The first curve was produced along the lower anterior edge of the sketches (**Figure 16A**). The second and third curves were generated by selecting reference points from the same sketches along the top labial and lingual surfaces, respectively (**Figure 16B-C**). The frequency of reference points for the guide curves was increased in certain regions to account for more complex and dramatic changes in geometry. The three reference curves produce a triangular bounding region by which to guide the loft feature. The original sketches were then overlaid on the lofted feature to ensure the proper profile had been created. The dorsal section of the jaw was generated in a similar manner with a few slight procedural changes. We used four reference curves, due to the nature of its geometry, to produce a rectangular bounding region by which to guide the loft feature. After the selection of the appropriate sketches and curves, the loft feature could be completed. Again, the original sketches were then overlaid on the lofted feature to ensure the proper profile had been created. The progress of the beams through these iterations can be seen in **Figure 17A-C**. **Figure 17A** shows the nonsymmetrical models with multiple sharp transition regions. Then, **Figure 17B** shows the symmetrical model that still possesses the sharp transition regions, but finally, **Figure 17C** shows the final anatomical model with symmetry and smooth transition regions.

Because RapidWorks only models single solid bodies and does not decipher between the cartilaginous jaws, dental ligament, and small teeth, it was necessary to use

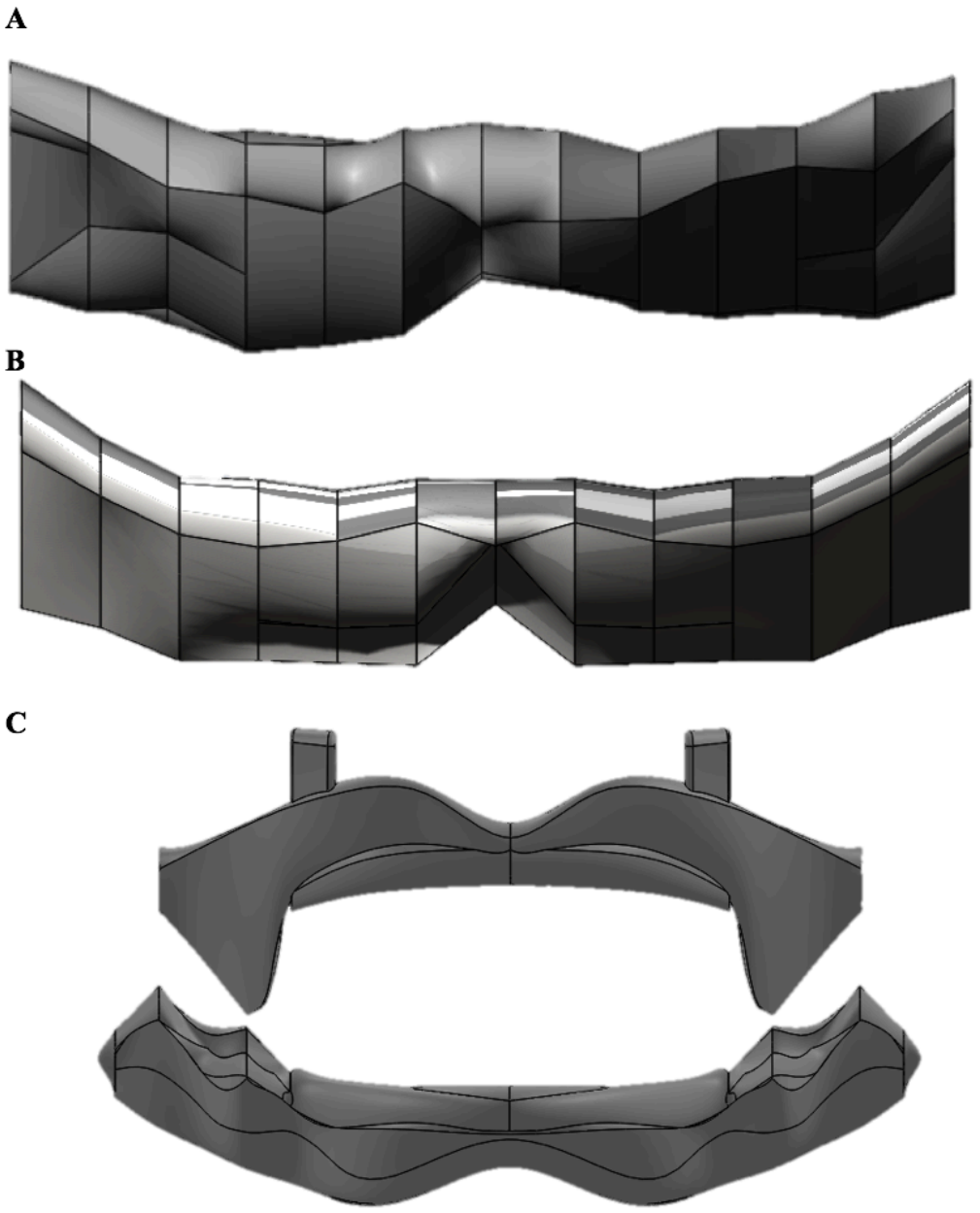

Figure 17: The results of the progressive simplification of the jaw structure. **A:** Frontal view of the ventral section of the first generation model. Note there is an absence of symmetry and smooth transition between the lofted regions. **B:** Frontal view of the ventral section of the second generation model. Note there is now symmetry in the model, but the areas of stress concentration have not yet been corrected. **C:** Ventral and dorsal jaw sections after the final sketch simplification.

Figure 18: Micro-CT image referenced to generate the dental ligament. The gap between the teeth and the calcified cartilage of the jaw is the soft tissue of the dental ligament that is not captured with CT imaging. Image taken using the Bruker SkyScan 1176: High-Resolution *In-Vivo* Micro-CT.

micro-computed tomography (micro-CT) as a reference for the outlines and boundaries of each (**Figure 18**). This was particularly true for the modeling of the soft tissues of the dental ligament. However, once we determined the outline, a solid body was generated from the sketches using the same symmetric lofting technique as previously described to loft the feature between $\pm$ 25 mm. This was also an iterative process where the geometry was progressively simplified. For the final iteration, we made simplified profile sketches consisting of three reference points from the aforementioned dental ligament sketches and lofted it over the $\pm$ 25 mm region.

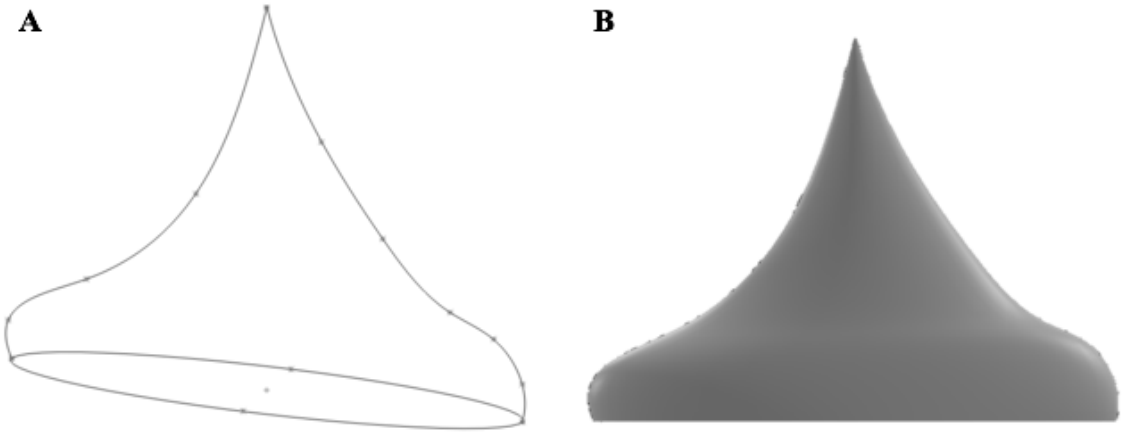

Figure 19: **A:** Shows the elliptical base and the two spline guide curves that were used to create the profile for the teeth. **B:** Shows the completed model of a tooth.

The teeth were modeled by taking measurements of the functional row of teeth of the *Sphyrna tiburo* specimen, as many of the rest were not accessible without damaging the jaw. The dimensions of the teeth were as follows: a 4 mm wide x 1 mm thick elliptical base, and a height of 3 mm. **Figure 19A-B** shows the tooth profile which was created in SolidWorks through the use of the loft function with the aid of guide curves to ensure the proper loft geometry. These flexibly attached teeth typically maintain a consistent shape throughout the feeding mechanism, meaning a large number of chondrichthyans are homodonts [33]. One notable exception to this is *Sphyrna tiburo*, which was used to generate the model for this study. *Sphyrna tiburo* has flatter teeth in the posterior regions of its jaw when compared to the sharp anterior teeth. However, this characteristic was disregarded, and a consistent tooth shape was kept throughout the files of teeth to make the models more representative of most elasmobranch species [33]. After the initial tooth had been modeled, additional teeth outside of the functional row were scaled to their

appropriate size (80%, 70%, 60%, and 50% of the original size, with the teeth in the functional layer being the largest and the lingual-most teeth being the smallest) [32].

3.1.2 MODEL SIMPLIFICATION FOR MECHANICAL TESTING

While the procedure mentioned above was beneficial for creating a representative anatomical model capable of characterizing multiple specimens, its complex geometry presented some challenges for testing. The first challenge is the complex moments of inertia generated during bending. Due to the overall shape of the jaw and the variable cross-sectional geometries, the moment of inertia would vary at different locations in the model. This factor could produce secondary torsional and shear forces that would complicate our goal to test the models in pure bending. Also, due to the desire to test and change multiple variables associated with dentition placement and orientation, the complex geometry of the above-noted model would present significant challenges regarding keeping consistency in the controlled variables. Consequently, we further simplified the models to allow for precise control of variables during bending and compression tests.

To further simplify the models, an average cross-sectional sketch was taken from both the ventral and dorsal jaw regions. Each of the sketches used in making the original ventral and dorsal jaw regions were placed on their own respective sketch plane, distinguishing geometric features were marked, and a cross-sectional geometry was determined from these key geometric features. After determining the cross-sectional geometry, an extrusion was performed to create a beam of the averaged geometry equivalent to the overall length of the original jaw model (80 mm). The same process was

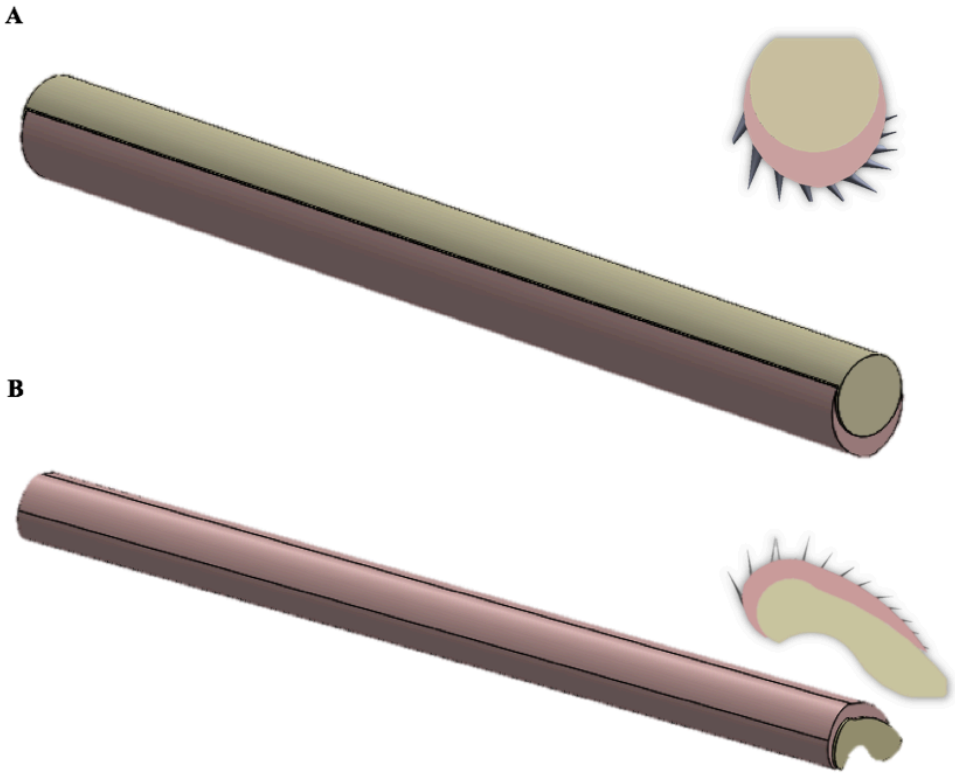

Figure 20: **A:** The average cross-sectional beam for the dorsal jaw region. **B:** The average cross-sectional beam for the ventral jaw region.

followed to create a dental ligament for the beam models. **Figure 20** shows the assembled models with the average jaw cross-section and dental ligament; from this image, it is possible to see the average profile that was used to make each of the beams.

After creating the jaw and dental ligament beams, we altered the patterning of the teeth. The first arrangement modeled was a parallel dentition pattern with a 1 mm gap between files (similar to the natural spacing for the *Sphyrna tiburo*). For the ventral beam 12 teeth (4x100% size, 2x80%, 2x70%, 2x60%, and 2x50%, to mirror the size of the native teeth) were equally spaced at angles varying from 120 degrees to -10 degrees along a sketch mirroring the curvature of the dental ligament. The model arrangement for the dorsal beam

followed a similar process except for the number of teeth, 10 for this beam instead of 12 (2x100% size, 2x80%, 2x70%, 2x60%, and 2x50%). The difference in the number of teeth was strictly due to size constrains associated with the number of teeth that could fit onto a single beam. However, it is still a reasonable approximation as some files had an equivalent number of teeth due to teeth lost during feeding. After producing these assemblies of teeth, they were repeated along a linear pattern for the respective jaw beams to create the complete models that can be seen in **Figure 21 A**. In addition, **Figure 21 C** shows an exploded model view of the ventral region of the model and better illustrates how the components fit together.

Following a similar process, a staggered dentition pattern with a 1 mm gap between like files was modeled for the ventral and dorsal beams. For each file of the ventral beam, there were six teeth (2x100% size, 1x80%, 1x70%, 1x60%, and 1x50%) equally spaced at the same angles described above. Similarly, the dorsal beam had 5 teeth in each file (1x100% size, 1x80%, 1x70%, 1x60%, and 1x50%). Again, these assemblies of teeth were repeated along a linear pattern for their respective jaw beam to produce the complete model for the staggered tooth pattern that can be seen in **Figure 21 B**. The process above was then repeated for an arrangement with no gap between the files for both the parallel and staggered patterns. Finally, before printing, all of the models were scaled up 2x their original size to better visualize the appearance of any cracks in the models during bending and gave the model a total length of 160 mm. **Figure 22** shows a closer look at the parallel and staggered dentition patterns, and all of the parameters used in this set of models can be seen below in **Table 2**.

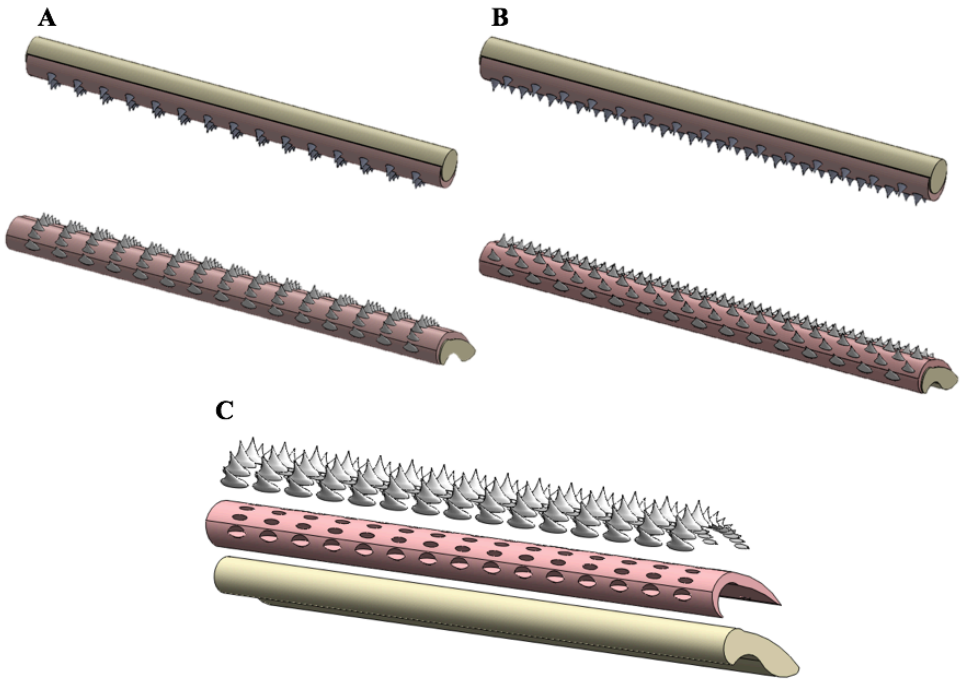

Figure 21: **A:** The ventral and dorsal beams (top and bottom respectively) with a parallel dentition pattern with a 1 mm gap between the files. **B:** The ventral and dorsal beams (top and bottom respectively) with a staggered dentition pattern with a 1 mm gap between the files. **C:** An exploded model view of the teeth, dental ligament and jaw cartilage.

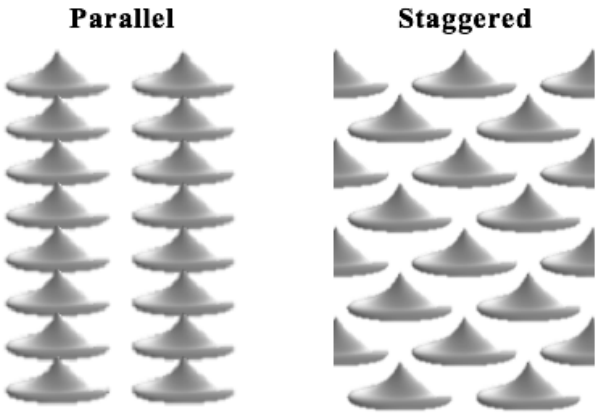

Figure 22: A closer look at the parallel and staggered tooth patterns.

Table 2: Tooth arrangement parameters for the average cross-sectional models.

Parameters for Average Cross-Section Beams		
File Spacing	**File Pattern**	**Jaw Region**
No Teeth	None	Dorsal
		Ventral
0 mm	Parallel	Dorsal
		Ventral
0 mm	Staggered	Dorsal
		Ventral
1mm	Parallel	Dorsal
		Ventral
1 mm	Staggered	Dorsal
		Ventral

3.1.3 SIMPLE GEOMETRIC MODELS

Upon seeing the results from the above mentioned models, which will be discussed in Chapter 3, we decided to further simplify the models to gain a more complete understanding of the variables influencing the mechanical behavior. The geometry was simplified to a rectangular cross-section equivalent to the average total volume of each of the jaw regions (**Figure 23)**. This further simplification allowed for two beneficial tasks to be accomplished. First, it allowed a more direct control over a number of variables and allowed for the introduction of new independent variables. Secondly, it allowed us to develop simple analytical models of the stress distributions through the beams during bending.

To create the models, the total volume of the ventral and dorsal beams was determined using the Mass Properties function in SolidWorks for the final jaw model described in Section 3.1.1. The volumes were then averaged, and the resulting total volume

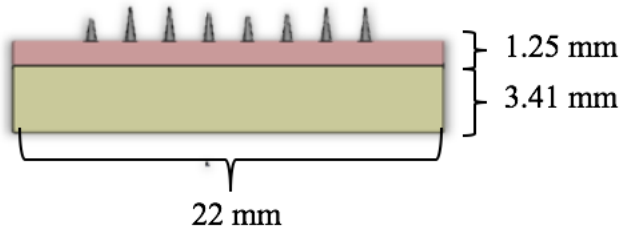

Figure 23: The rectangular cross-section representative of the ventral jaw region.

of the jaw was determined to be 6000 mm^3. With the total length of the models known, 80 mm, we knew that the cross-sectional area of the models must be equivalent to 75 mm^2.

With this information, we determined the width of the rectangular beam must be at least 22 mm to fit all of the teeth for the desired parameters. This, consequently, requires a 3.41 mm thickness for the rectangular beam to have the 75 mm^2 area. The dental ligament was then generated for the beams. Based off of previous CT scan data, we used an average thickness of 1.25 mm for the dental ligament. The dental ligament was modeled over the whole top surface of the rectangular beam, giving the model a total volume of 82000 mm^3.

The tooth modeled in Section 3.1.1 was used for the teeth in this set of models as well. However, in this case, the teeth were kept a constant size and normal to the surface of the jaw. This was done to remove any potential variability that could occur due to variations in size or angle and give clearer trends as they relate to file patterning with respect to one another. The teeth were patterned according to a number of variables, all of which can be seen in **Table 3**. The standard for the models was the medium stiffness jaw material, 1 mm file spacing, and 0 mm file depth. Each of the other variables was modeled around this control model. For each case, one variable was changed while the others were held constant, and a parallel and staggered dentition pattern was modeled for each set. A

closer look at the file spacing and file depth variables can be seen in **Figure 24**. Though not found in chondrichthyans in nature, the depth was tested at 0 mm and -1mm to show the implications that socketed teeth could potentially have on the feeding mechanism and if there is a mechanical advantage for chondrichthyans to have teeth with a loose superficial attachment.

Table 3: Parameters for the rectangular beams. The jaw material, file spacing and file depth were all treated as independent variable that were tested in three variations each in parallel and staggered dentition patterns. The variables highlighted in red are the ones being varied for that case, while all of the others are held constant.

Parameters for Rectangular Beams			
Jaw Material (Stiffness) [Printer Material]	**File Spacing**	**File Depth**	**File Pattern**
Soft (2MPa) [FLX9750]	1 mm	0 mm	Parallel
			Staggered
Medium (10 MPa) [FLX9770]	1 mm	0 mm	Parallel
			Staggered
Hard (30 MPa) [FLX9795]	1 mm	0 mm	Parallel
			Staggered
Medium (10 MPa) [FLX9770]	0 mm	0 mm	Parallel
			Staggered
Medium (10 MPa) [FLX9770]	1 mm	0 mm	Parallel
			Staggered
Medium (10 MPa) [FLX9770]	2 mm	0 mm	Parallel
			Staggered
Medium (10 MPa) [FLX9770]	1 mm	+1 mm	Parallel
			Staggered
Medium (10 MPa) [FLX9770]	1 mm	0 mm	Parallel
			Staggered
Medium (10 MPa) [FLX9770]	1 mm	-1 mm	Parallel
			Staggered

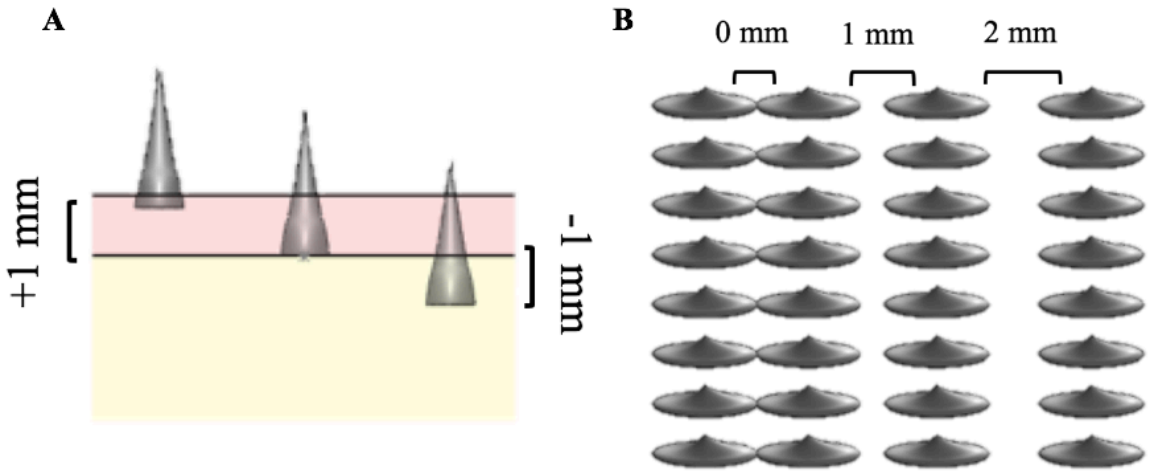

Figure 24: A: The variations in the depths of the teeth. The positions vary between 1 mm above the surface of the jaw cartilage (+ 1 mm), adjacent to the surface of the jaw cartilage (0 mm), and embedded 1 mm within the jaw cartilage (-1 mm). **B:** The variations in the spacing between like files.

3.1.4 MODELS FOR MATERIAL TESTING

In addition to the jaw beam models, a set of cubes and dog-bones were modeled for baseline compression and tension testing respectively. The testing of these models provided us with our own values for the material properties of each of the printer materials that were used. The dimensions for the compression cubes were 10 mm x 10 mm x 10 mm and can be seen in **Figure 25.** The dimensions for the dog-bone shaped samples were inspired by the Type III specimen from ASTM D638-14 the Standard Test Method for Tensile Properties of Plastics [53]. This specimen type was chosen due to the thicknesses of the models that were used for our beam testing, as the thickness of our model fell within its specifications. To facilitate the printing of multiple samples, the dimensions were scaled down to 20% of those specified in the ASTM standard. The resultant dimensions can be seen in **Figure 26**.

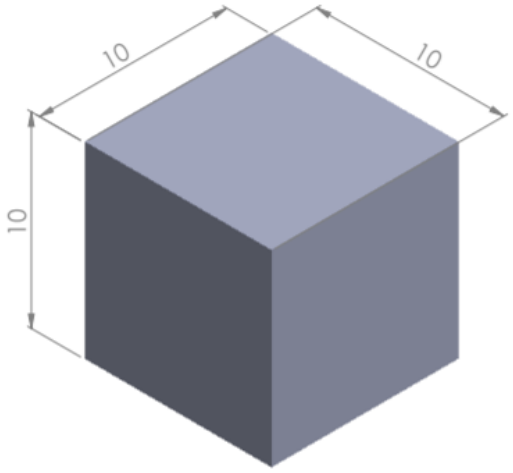

Figure 25: The dimensions for the compression cubes that were used to establish the baseline compression modulus.

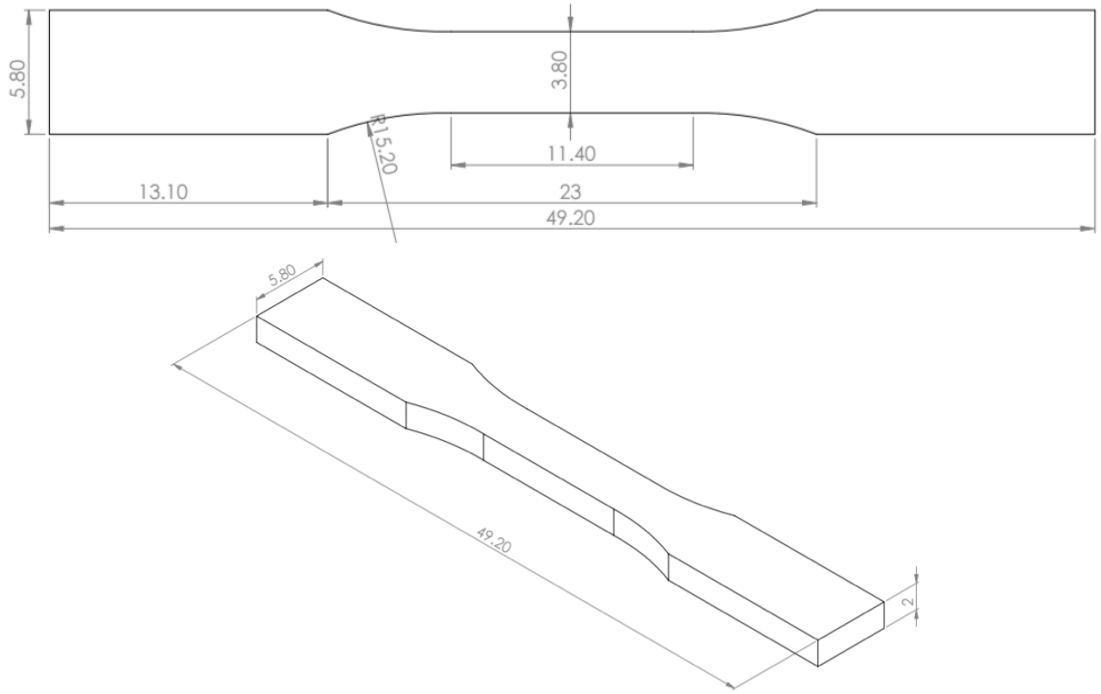

Figure 26: The dimensions for the tensile dog-bone specimen. The dimensions are 20% of those of the Type III specimen prescribed by ASTM D638-14.

3.2 MATERIAL SELECTION

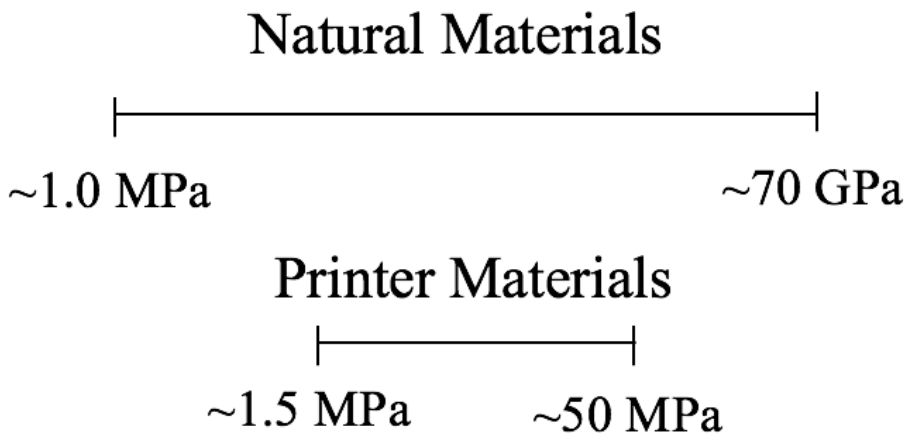

Figure 27: This depicts the difference in the range of properties of the natural materials as compared to the printer materials. **Note:** The lines are not scaled to actual size.

After generating the CAD models, it was then necessary to appropriately relate the natural materials in each region of the feeding mechanism to available synthetic materials that would allow the models to be printed using a multi-material 3D printer, as seen in **Figure 27**. The material selection process was a vital component to permit a reasonable comparison of the printed jaw models and the natural specimens. We completed two major tasks that allowed for more precise characterization of the native jaw tissue in the form of 3D printable material. The first task was the determination of the stiffness of the teeth, dental ligament, and jaw of a natural specimen. The second was to scale the material properties to the strengths of the printable materials. The printer used for this project was the Stratasys Object 350 Connex3 PolyJet 3D Multi-Material Printer. The available materials and their respective strengths can be seen in **Table 4**.

Table 4: The components of the feeding mechanism and their stiffness values related to the available printer materials and their respective strengths [24,28,29,32,52,54].

Component of Feeding Mechanism	Stiffness of Natural Material	Printer Material	Strength of Corresponding Printer Material
Teeth	27 GPa	VeroWhite	50 MPa
Jaw	400 MPa	FLX9795	8.5-10 MPa
		FLX9770	3.5-5 MPa
		FLX9750	1.9-3.0 MPa
Dental Ligament	1.12 MPa	TangoPlus	1.5 MPa

To determine the representative range of material properties, we conducted an extensive literature review. For the teeth, we gathered the material properties from research performed by Whitenack et al. [29] as can be seen in the material property chart shown earlier in **Table 1** in Chapter 1. Upon investigating images from Moyer et al. [32], we determined the distribution to be approximately 10% enameloid and 90% orthodentine for the *Sphyrna tiburo*. Following this, we applied the Voigt model for the rule of mixtures and determined that an equivalent single-material tooth would have a Young's Modulus of approximately 27 GPa. The Voigt model for the rule of mixtures is:

$$E_T = V_1E_1 + V_2E_2\,, \qquad \text{(Eq. 1)}$$

where *E_T: Young's Modulus of the homogeneous material, E_1: Young's Modulus of enameloid, E_2: Young's Modulus of orthodentine, V_1: Volume fraction of enameloid, V_2: Volume fraction of orthodentine*

Knowing that this would be the region of the model with the highest stiffness, we assigned this part to the VeroWhite material in **Table 4**. Next, we determined the lower bound of the strength of the model, corresponding to material properties of the oral mucosa. Chen et al. [52] found that the Young's Modulus of the oral mucosa was approximately 1.12 MPa. With this information, we were able to assign the Tango+ material to the dental ligament of the model.

The final step in the material selection process was to assign the material for the representative jaw cartilage. As was mentioned earlier, the jaw consists of calcified tesserae overlying an uncalcified cartilaginous core. We experienced some difficulty in determining the appropriate Young's Modulus for the jaw, as the properties seemed to vary widely between species, and we found little information on both the calcified and uncalcified cartilage. Consequently, we extrapolated some of the data to determine the Young's Modulus of the equivalent homologous pair. The most accurate data we could find for the uncalcified cartilage was from Porter et al. [24] on a shark from the same genus as the bonnethead shark, which was a Young's Modulus of 48.22 MPa for a smooth hammerhead shark (*Sphyrna zygaena*). Following this, we were able to loosely establish a ratio of the Young's Modulus of the calcified to uncalcified cartilage from data by Wroe et al. [28]. This information provided an estimation for the Young's Modulus of calcified cartilage in that it is approximately 73.5 times that of the uncalcified cartilage (4.05 GPa/55.1 MPa ratio of calcified to uncalcified cartilage). Consequently, using this ratio, we determined the Young's Modulus for calcified cartilage of the bonnethead shark would be approximately 3.54 GPa. Similar to the case above with the teeth, we examined CT images

from our specimen and determined that the jaw too had approximately 90%/10% relationship of uncalcified to calcified cartilage. Again, we applied the Voigt model for the rule of mixtures to determined that the homologous equivalent jaw has a Young's Modulus of 400 MPa.

Now that the upper bound, lower bound, and value of the homogeneous jaw are known, scaling the strength of the material for the representative jaw cartilage can be determined by:

$$\frac{\mathrm{X} - \mathrm{X_{min}}}{\mathrm{X_{max}} - \mathrm{X_{min}}} = \frac{X' - X'_{min}}{X'_{max} - X'_{min}}, \qquad \text{(Eq. 2)}$$

where X_{max} *: original range max,* X_{min}*: original range min, X: original value for the jaw,* X'_{max}*: new range max,* X'_{min}*: new range min,* X'*: unknown value of representative jaw cartilage material*

From **Eq. 2**, we calculated that the strength of the equivalent jaw cartilage material should be approximately 2.2 MPa. This value translates to the FLX9750 in **Table 4**. It is important to note, however, that due to the large variation in jaw properties found in literature and to compensate for the inexact approximation of the 90%/10% composition of the teeth and jaw, it was later decided to treat the jaw cartilage material as an additional variable during testing. Consequently, tests were run with samples containing the FLX9750, FLX9770, and FLX9795 materials from **Table 4**.

3.3 MODEL PRINTING

As noted above, all of the models were printed using the Stratasys Object 350 Connex3 PolyJet 3D Multi-Material Printer and Stratasys PolyJet photopolymer materials (Stratasys, Ltd., Eden Prairie, MN.) This printer provides a 342 x 342 x 200 mm build platform with an accuracy as high as 20 microns and layer thicknesses as small as 16 microns.

When 3D printing models, there is always the potential for some variability in the material properties. Because of this, we attempted to control as many variables as possible. First, all of the models were printed in the same orientation to ensure that there were no differences in the directionality of the layers in the composite material. The models were arranged end to end with the representative jaw material on the base. This allowed the layers of the model to be printed lengthwise with a 30-micron thickness of each layer. Secondly, each set of models was printed with the same printer material cartridges. There can be some variation in the material properties of the printer materials depending upon the batch in which the material was produced by the manufacturer, as can been seen in **Table 4**. Consequently, to minimize variability in the final models, we ensured that the models were printed from a single batch of each of the materials. Finally, the properties have the potential to vary somewhat if the resin has not had time to cure fully. Therefore, all of the models were tested 24 hours after printing to allow the samples to cure fully before testing.

For the average cross-sectional models described in Section 3.1.2, there were a total of 14 unique models printed. The first 10 beams followed the parameters stated in **Table 2** and utilized the materials Tango+, FLX9750, and VeroWhite, for the representative dental ligament, jaw cartilage, and teeth respectively. The final four models had parallel and staggered orientations with no gap between the file spacing. The only difference here was that the jaw cartilage was printed with the stiffer material, FLX9795, as compared to the original FLX9750. **Figure 28** shows some of the resulting prints for this set of models.

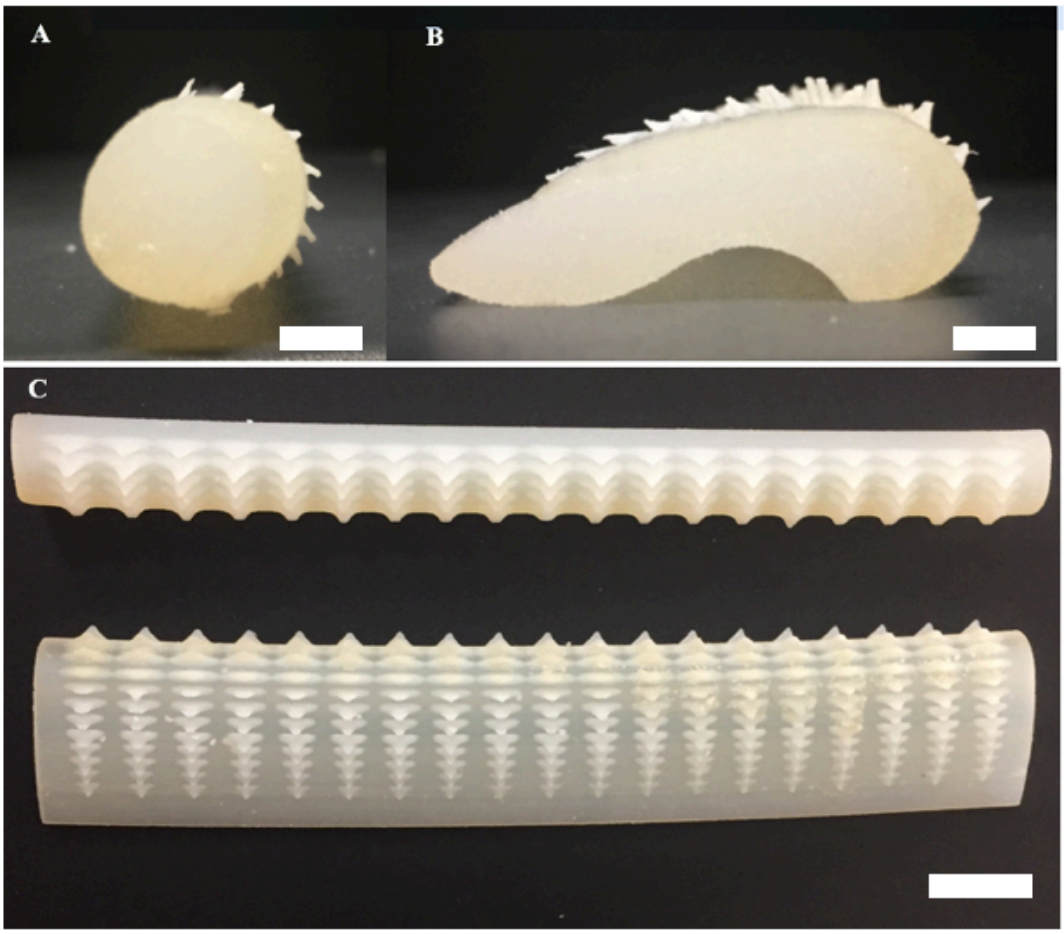

Figure 28: The printed average cross-section models. **A:** The representative average cross-section of the dorsal jaw region. Scale bar is 5 mm. **B:** The representative average cross-section of the ventral jaw region. Scale bar is 5 mm. **C:** View of both the dorsal and ventral jaw regions with a parallel dentition pattern. Scale bar is 10 mm

The next set of models printed were the rectangular cross-sectional beams (**Figure 29**) There were a total of 14 unique beams that were printed, and each of the parameters can be seen in **Table 3**.

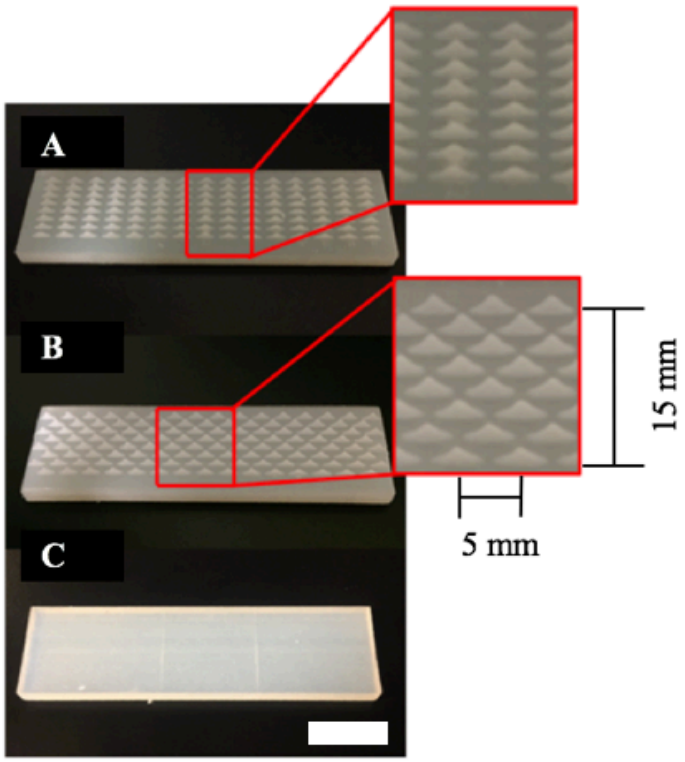

Figure 29: The printed rectangular models. **A:** Rectangular with the parallel dentition pattern. **B:** Rectangular with the staggered dentition pattern. **C:** Rectangular with no teeth. Scale bar is 10 mm

The final prints to discuss are the models for material testing. For these, three compression cubes and three tensile dog-bones were printed in Tango+, FLX9750, FLX9795, and VeroWhite to give a total of 12 cubes and 12 dog-bones for testing. **Figure 30** provides a look at the printed models. In addition, since the FLX9770 was added as a parameter late in the testing process, compression data were gathered on this material by dissecting the FLX9770 material out of two of the beam samples. These portions were then cut at 20 mm increments to provide 8 rectangular sections for compression testing.

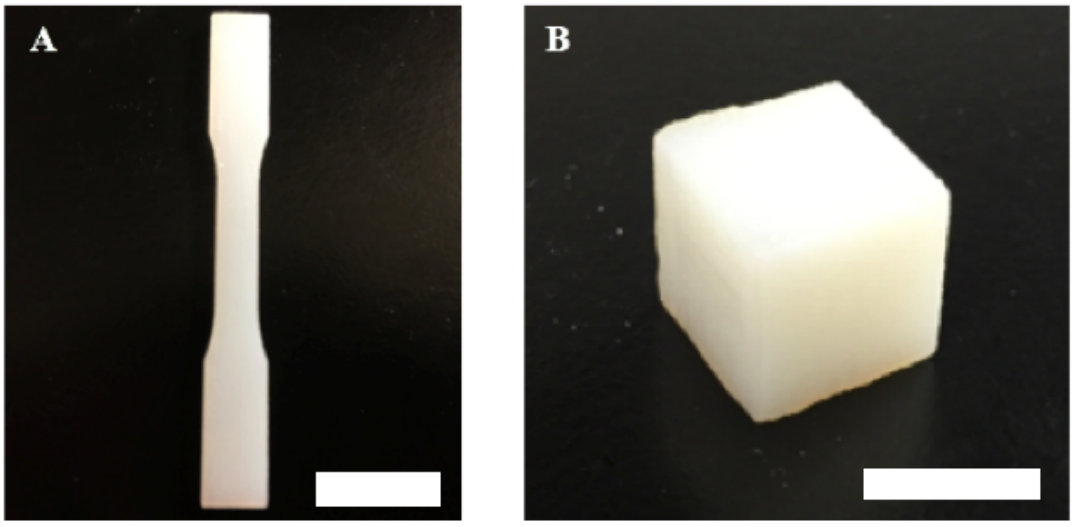

Figure 30: **A:** The 3D printed dog-bone shaped sample for the base-line tensile testing. **B:** The 3D printed cube for the base-line compression testing. Scale bars are 10 mm

3.4 MODEL TESTING

All of the models for this project were tested using the Shimadzu Autograph AGS-50kNXD Precision Universal Tester (**Figure 31)**, and the data were recorded on the Shimadzu Trapezium X Autograph Version 1.4.0 Software (Kyoto, Kyoto Prefecture, Japan). There were three separate types of mechanical tests run on samples throughout this project: three-point bending, compression, and tensile tests. All of the tests were run using either a 500 N or 50 kN load cell with a strain rate of 0.1 mm/sec. A safety cut-off was set for 450 N and 49 kN, respectively, to ensure that the loading never exceeded the capacity of the load cell. The other testing variables depended upon the type of mechanical testing being performed and the sample being tested. The exact testing procedures for each case will be outlined in the following sections.

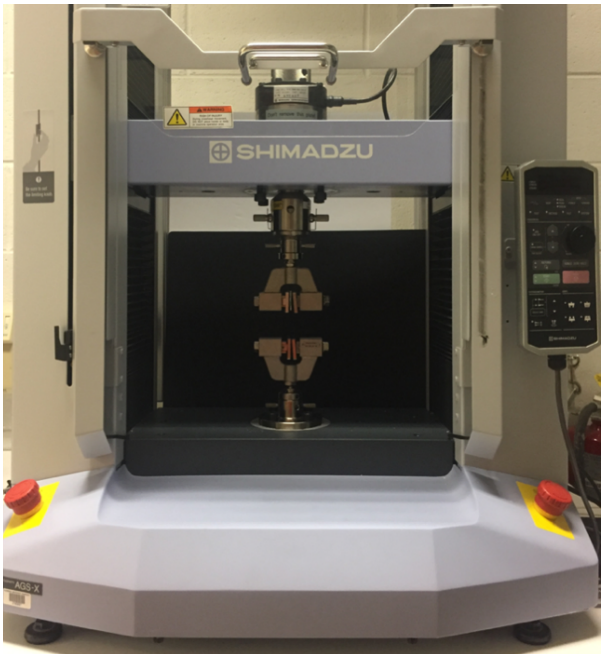

Figure 31: The Shimadzu Autograph AGS-X Series Precision Universal Tester.

3.4.1 THREE-POINT BENDING

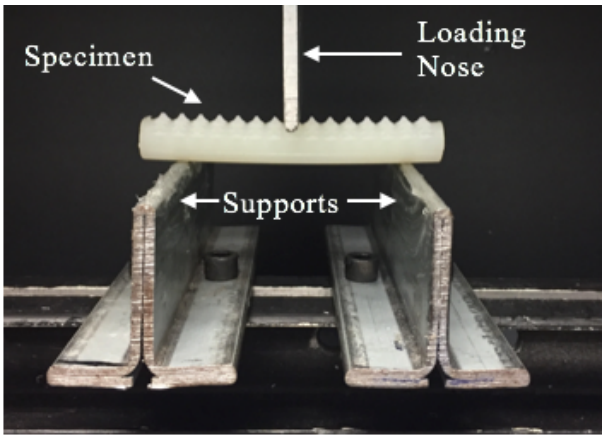

Figure 32: Setup for the three-point bend test. Beam is centered on the bottom supports with the teeth facing upward. The loading nose it lowered to where is just contacts the surface of the teeth. The radius of the supports and loading nose is 2.75 mm.

Three-point bend tests were performed to determine the apparent flexural modulus and maximum flexural strength for each of the modeled beams; the general setup can be seen in **Figure 32**. For every test, the beam was centered on the supports with the teeth facing upward to approximately orient the force as it might be during biting. The loading nose was then lowered onto the center file of teeth to the initial point of contact. The beams were then loaded with a 500 N load cell at a strain rate of 0.1 mm/sec.

Each average cross-section beam was tested twice. In the first test, the supports were set at 120 mm (75% the length of the beam) apart from one another. The beams were then displaced 20 mm. This was done to measure the flexural modulus within the elastic regime. Following this, in an effort to save money on an expensive material, the beams were cut in half. The supports were adjusted to be 40 mm apart from one another, and the specimen was displaced to 35 mm or until failure, whichever occurred first. The 35 mm was set as the maximum allowable displacement to prevent the loading nose from contacting the base of the machine.

The three-point bend test of the rectangular beams followed a combination of the methods above. For this set of tests, the supports were returned to 75% of the length of the 80 mm beam, or in this case 60 mm apart from one another. The specimens were centered on the supports, and the loading nose was lowered into position. These specimens were then displaced 35 mm or until failure.

To analyze the data for the rectangular beams, all of the force-displacement data were converted to stress-strain data. During three-point bending, the maximum stress

occurs at the middle of the span length. The resultant maximum flexural stress can be calculated at any point on the load-deflection curve through the use of **Eq. 3** [56]:

$$\sigma_f = \frac{3PL}{2bd^2}, \quad \text{(Eq. 3)}$$

where σ_f*: flexural stress [MPa], P: load at a given point on the load-defection curve [N], L: span of supports [mm], b: width of the specimen [mm], d: depth of the specimen [mm]*

The flexural strain experience by the models during the three-point bend testing can be calculated using **Eq. 4** [56]:

$$\varepsilon_f = \frac{6\delta d}{L^2}, \quad \text{(Eq. 4)}$$

where ε_f*: flexural strain [unitless],* δ*: deflection at center [mm], L: span of supports [mm], d: depth [mm]*

The dimensions are based off of those discussed in above in Section 3.1.3. The width of the beams is 22 mm and depth is 4.66 mm. Upon determining the stress and strain for each data point, the results were plotted and the flexural modulus calculated using Hooke's Law:

$$E = \frac{\sigma}{\varepsilon} \quad \text{(Eq. 5)}$$

where *E: slope of the linear region of the stress-strain curve [MPa],* σ*: engineering stress [MPa],* ε*: engineering strain [unitless]*

3.4.2 COMPRESSION TESTING METHODS

Compression tests were run on the rectangular models. **Figure 33** shows the general setup. The specimens were loaded with the 50 kN load cell at a strain rate of 0.1 mm/sec until the safety cutoff was reached. As with the three-point bend tests, the force-displacement data from the compression tests was converted to stress-strain data. The compressive stress was calculated using **Eq. 6**, where the area is a function of the length and width of the specimens: 80 mm x 22 mm for the rectangular specimen. The compressive strain was calculated using **Eq. 7**. Subsequently, the stress-strain data were plotted, and the plots were corrected for preload. Then the slope from the linear region (initial 10% strain) was used to determine the compressive modulus of the beams.

$$\sigma = \frac{F}{A}, \qquad \text{(Eq. 6)}$$

where σ*: engineering stress [MPa], F: uniaxial force [N], A: cross-sectional area [mm^2]*

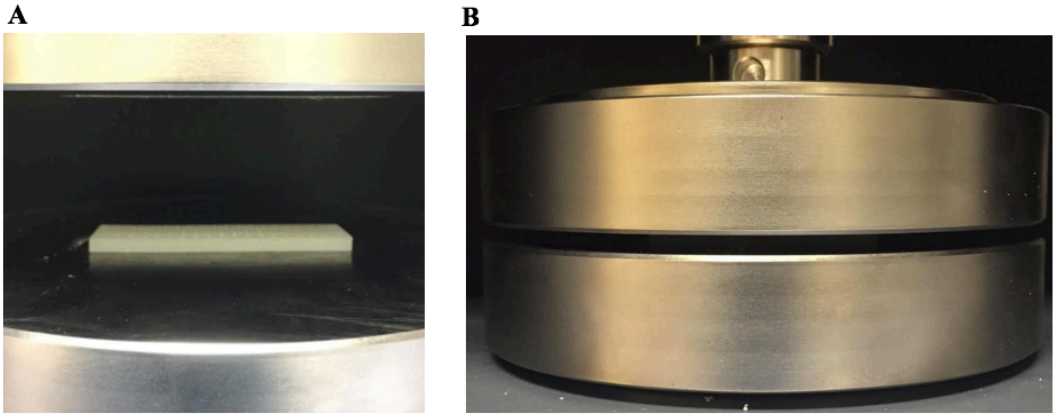

Figure 33: Setup for the compression tests. **A:** Specimen is centered on the bottom plate. **B:** The top plate is lowered until initial contact is made with the specimen. The tests proceeded until the safety cut-off load is met.

$$\varepsilon = \frac{\Delta l}{l_0} \quad \text{(Eq. 7)}$$

where ε*: engineering strain [unitless],* l_0*: original length [mm],* Δl*: change in length [mm]*

3.4.3 MATERIAL PROPERTIES TESTING

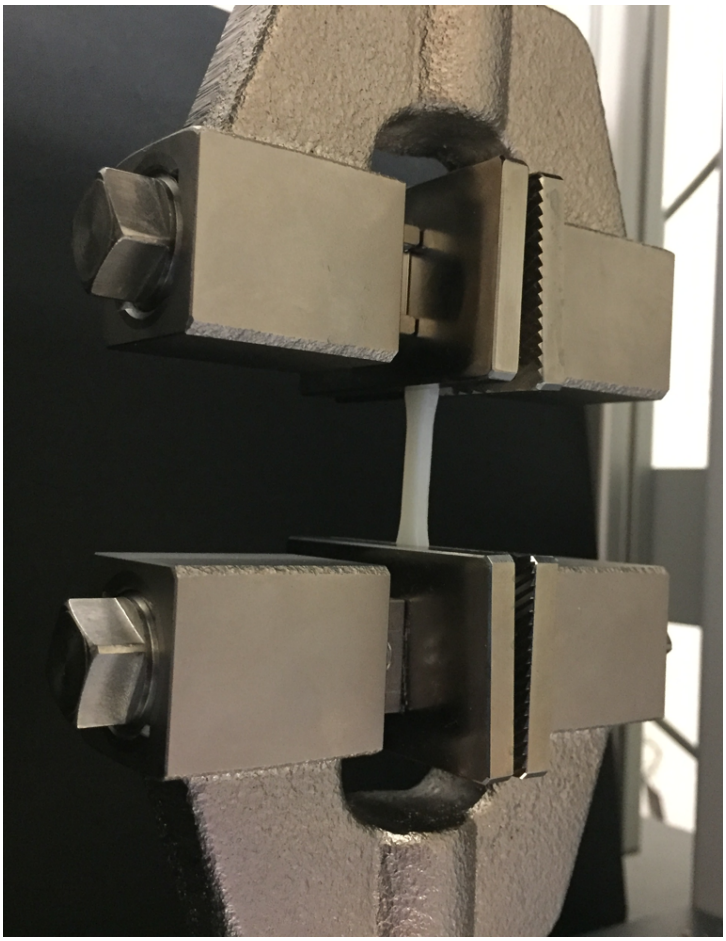

Figure 34: Setup for the tensile tests. The tensile dog-bone clamped with 23 mm between the grips.

When testing the compression cubes, they were placed in the center of the plate and loaded in the same manner as the beams discussed above. However, the compression cubes were loaded with the 500 N load cell. The stress and strain were again calculated using

Eq. 6 and **Eq. 7**, where the cross-sectional area is 10 mm x 10 mm. Likewise, the stress-strain data was plotted, and the plots were corrected for preload. Then the slope from the linear region (initial 10% strain) was used to determine the compressive modulus of the cubes.

When performing the tensile test, the dog-bone shaped tensile specimens were oriented as seen in **Figure 34**. The specimens were centered and clamped in the lower grips at the location marked in **Figure 35**. The upper grip was then lowered until it was 23 mm from the lower grip. The clamps on both of the grips were aligned with one another and tightened by hand until they were snug. This ensured that there would be no slippage of the specimen and that all of the force would be applied parallel to the vertical axis of the specimen. The specimens were loaded in tension at a displacement rate of 0.1mm/sec with the 500 N load cell until fracture.

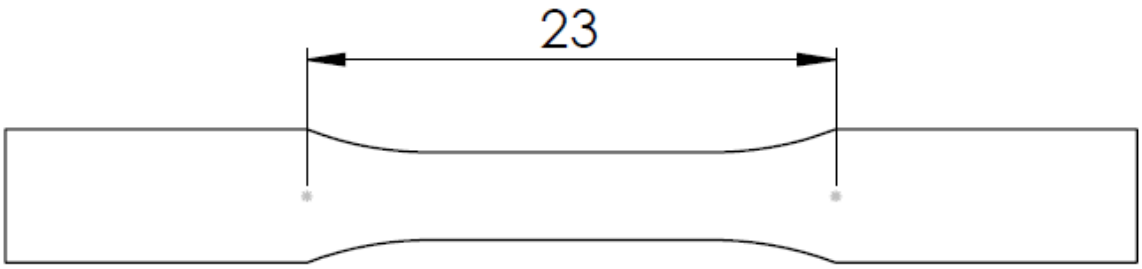

Figure 35: The locations for where to grip the sample during testing. The grips should be 23 mm apart during testing according to our adjustment of ASTM 638-14 [53].

Table 5 shows the measured material properties of the 3D printed materials used in this study. The tensile and compressive moduli for each material were determined by Hooke's law. When using **Eq. 6** for the dog-bone samples, the area was calculated from the width at the center of the sample and the overall thickness, 3.8 mm and 2 mm respectively, as seen in **Figure 26**. Also, the original length used to calculate the strain for

Table 5: The average moduli resulting from the uniaxial compression testing of the cube samples and uniaxial tensile testing of the dog-bone samples. Note: The FLX9770 samples were tested at a later date, and the material samples were taken from the beam models. Therefore, only compression tests were run on this material.

Material Moduli Values (MPa)		
Material	**Compressive Modulus**	**Tensile Modulus**
Tango Plus	0.9	0.3
FLX9750	2.0	0.7
FLX 9770	10	-
FLX9795	30	70
VeroWhite	77	480

the uniaxial tensile test corresponds with the gauge length of the samples, 10 mm. Hooke's law was then used to determine the moduli of the materials.

There were no reported data on the Young's Moduli of the printer materials with the exception of VeroWhite [54]. Consequently, we measured the Young's Modulus for the TangoPlus, FLX9750, FLX9770 FLX9795, and VeroWhite materials. The results in **Table 5** reveal the bimodularity of the materials, meaning the moduli are different in compression and tension. This is not an uncommon characteristic and can be seen in natural rubbers and silicone, in addition to other materials [55]. In the cases of the TangoPlus and FLX9750 materials, the stiffness is slightly higher in compression than in tension. In contrast, the FLX9795 and VeroWhite materials are more stiff in tension than compression. One of the factors likely contributing to the bimodularity of the samples is the orientation of the layers during printing. Since the samples were produced using a PolyJet 3D printer rather than being cut from a single block of material, there are multiple layers of the material that are all aligned within the sample. To minimize the influence of the layering effect on the results, consistency in the orientation of testing was maintained, and all of the

samples were tested parallel to the orientation of the layers. As with the rectangular beams discussed above, the models were printed with the longest edge of the model laying flat on the surface of the build platform. This orientation was chosen due to the inefficiency and cost that would have been associated with printing the tensile dog-bone in a manner that would have allowed for testing perpendicular to the layer orientation. Consequently, to maintain consistency, both the tensile dog-bone and the compression cubes were tested in the same orientation.

3.5 MODULUS APPROXIMATION

The apparent moduli for the multicomponent layers of the beams were approximated using four separate techniques. The first approximation was through the use of the Voigt model for the rule of mixtures (**Eq. 1**). The second was through the use of the Reuss model for the rule of mixtures:

$$\frac{1}{E_{AB}} = \frac{V_A}{E_A} + \frac{V_B}{E_B}, \quad \text{(Eq. 8)}$$

where *E_{AB}: equivalent component modulus [MPa], E_A: modulus of material A [MPa], V_A: volume fraction of material A [mm^3], E_B: modulus of material B [MPa], V_B: volume fraction of material B [mm]^3*

The Voigt and Reuss models assume a homogenous mixture of the components and provide upper and lower bounds, respectively, for approximate moduli values. However, these are not the most accurate representations. Therefore, we used two additional methods

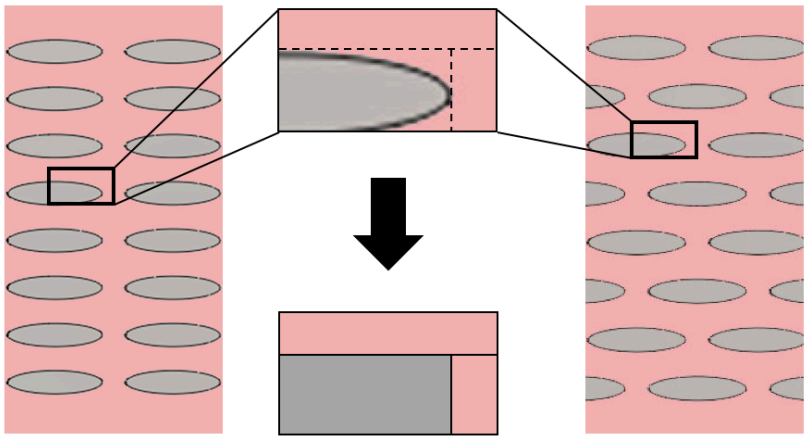

Figure 36: The representative volume element (RVE) is the smallest repeating unit. Parallel and staggered patterns share the same RVE.

that combined the Voigt and Reuss models to determine the moduli of the multicomponent layers to compensate for the nonhomogeneous nature of the models. To use a combination of the Voigt and Reuss models, the multicomponent layer had to be simplified into a representative volume element (RVE) (**Figure 36**). The RVE can then be simplified into a geometric approximation of the components. This idea was inspired by the work done by Jayasankar et al [56]. The sections of the RVE can be oriented in two different ways, as seen in **Figure 37**.

RVE(1) and RVE(2) (**Figure 37**) were used to model the parallel and staggered dentition patterns, respectively. The orientation of the regions in RVE(1) best matched that response of the parallel dentition pattern, while RVE(2) better modeled the response of the staggered pattern. Looking at RVE(1) in **Figure 37A**, the element is divided into two regions perpendicular to the direction of the force. Region 1 is simply the dental ligament and Region 2 is comprised of two elements in parallel and was modeled using the Voigt model (**Eq. 1**).

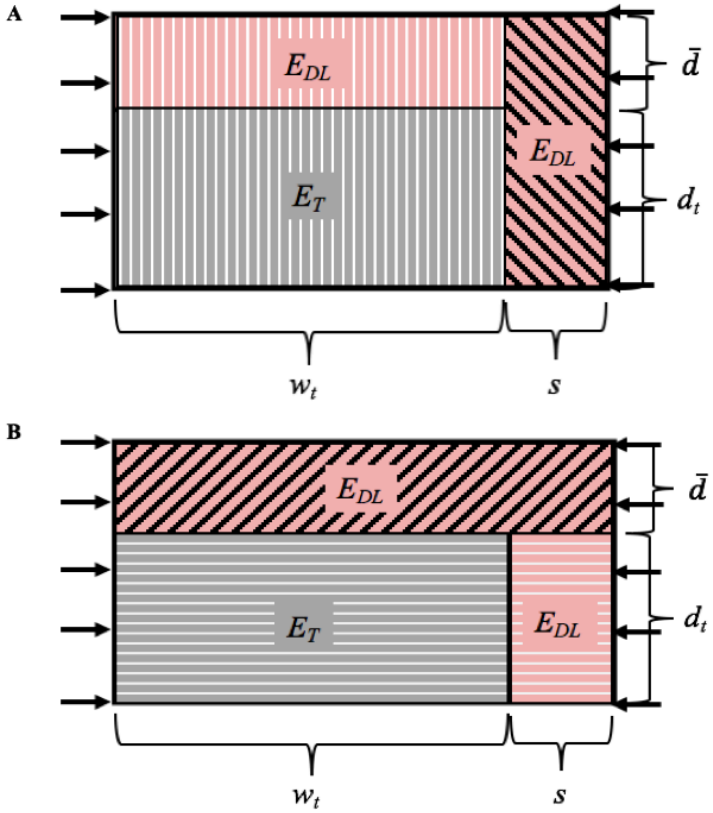

Figure 37: The two orientations of the compressive forces experienced during bending. **A:** RVE(1) is divided into two vertically oriented regions. Region 1 is the right most region with the diagonal bars. Region 2 is the left most region with vertical bars. **B:** RVE(2) is divided into two horizontally oriented regions. Region 1 is the top region with the diagonal bars. Region 2 is the bottom region with the horizontal bars. w_t: width of the tooth section in the RVE (half of the total tooth width); s: half the width of the gap between teeth; d_t: thickness of the tooth; $\bar{d}$: half the average distance between teeth in a single file. Each RVE has a prescribed thickness, t, as defined by the depth of the tooth in the feeding mechanism.

Region 1:

$$E_1 = E_{DL}$$

$$V_1 = st(d_t + \bar{d}) \quad \text{(Eq. 9)}$$

Region 2:

$$E_2 = (\phi_T)(E_T) + (\phi_{DL})(E_{DL})$$

$$V_2 = w_t t(d_t + \bar{d}) \quad \text{(Eq. 10)}$$

when,

$$\phi_T = \frac{w_t d_t t}{V_2} \quad \text{(Eq. 11)}$$

$$\phi_{DL} = \frac{w_t \bar{d} t}{V_2} \quad \text{(Eq. 12)}$$

where *E_1: modulus of Region 1; E_{DL}: modulus of the dental ligament; V_1: Volume of Region 1; E_2: modulus of Region 2; E_T: modulus of the teeth; V_2: Volume of Region 2; s: half the width of the gap between teeth; t: thickness of RVE(1); d_t: thickness of the tooth; $\bar{d}$: half the average distance between teeth in a single file. w_t: width of the tooth section in RVE(1) (half of the total tooth width); ϕ_T: volume fraction of the teeth in Region 2; ϕ_{DL}: volume fraction of the dental ligament in Region 2*

These two regions are in series with each other and were modeled using the Reuss model (**Eq. 8**).

RVE(1):

$$\frac{1}{E_{RVE(1)}} = \frac{\phi_1}{E_1} + \frac{\phi_2}{E_2}$$

where,

$$\phi_1 = \frac{V_1}{V_1 + V_2} \quad \text{(Eq. 13)}$$

$$\phi_2 = \frac{V_2}{V_1+V_2} \quad \text{(Eq. 14)}$$

where *E_1: modulus of Region 1; V_1: volume of Region 1; E_2: modulus of Region 2; V_2: volume of Region 2; $E_{RVE(1)}$: modulus of the representative volume element; ϕ_1: volume fraction of Region 1; ϕ_2: volume fraction of Region 2*

The system of equations for calculating the modulus of RVE(1) simplifies to a function of $f(E_{DL}, E_T, \bar{d}, d_t, s, w_t)$:

$$E_{RVE(1)} = \frac{E_{DL}(s+w_t)(E_{DL}\bar{d}+E_T d_t)}{E_{DL}\bar{d}s+E_T d_t s+E_{DL}\bar{d}w_t+E_{DL}d_t w_t} \quad \text{(Eq. 15)}$$

where *$E_{RVE(1)}$: modulus of the representative volume element; E_{DL}: modulus of the dental ligament; E_T: modulus of the teeth; s: half the width of the gap between teeth; d_t: thickness of the tooth; $\bar{d}$: half the average distance between teeth in a single file. w_t: width of the tooth section in the RVE(1) (half of the total tooth width)*

Looking at RVE(2) in **Figure 37B**, the element is divided into two regions normal to the direction of the force. Again, Region 1 is simply the dental ligament and Region 2 is comprised of two elements in series and was modeled using the Reuss model for the rule of mixtures (**Eq. 8**).

Region 1:

$$E_1 = E_{DL}$$

$$V_1' = \bar{d}t(w_t + s) \quad \text{(Eq. 16)}$$

Region 2:

$$\frac{1}{E_2} = \frac{\phi_T'}{E_T} + \frac{\phi_{Dl}'}{E_{DL}}$$

$$V_2' = d_t t(w_t + s) \quad \text{(Eq. 17)}$$

when,

$$\phi_T' = \frac{w_t d_t t}{V_2'} \quad \text{(Eq. 18)}$$

$$\phi_{Dl}' = \frac{w_t \bar{d} t}{V_2'} \quad \text{(Eq. 19)}$$

where *E_1: modulus of Region 1; V_1': volume of Region 1; E_{DL}: modulus of the dental ligament; E_2: modulus of Region 2; V_2': volume of Region 2; E_T: modulus of the teeth; ϕ_T': volume fraction of the teeth in Region 2; ϕ_{Dl}': volume fraction of the dental ligament in Region 2; s: half the width of the gap between teeth; t: thickness of RVE(2); d_t: thickness of the tooth; $\bar{d}$: half the average distance between teeth in a single file. w_t: width of the tooth section in RVE(2) (half of the total tooth width)*

These two regions are in parallel with each other and were modeled using the Voigt model (**Eq. 1**).

RVE(2):

$$E_{RVE(2)} = (\phi_1')(E_1) + (\phi_2' E_2)$$

when,

$$\phi_1' = \frac{V_1'}{V_1' + V_2'} \quad \text{(Eq. 20)}$$

$$\phi_2' = \frac{V_2'}{V_1' + V_2'} \quad \text{(Eq. 21)}$$

where *E_1: modulus of Region 1; E_2: modulus of Region 2; $E_{RVE(2)}$: modulus of the representative volume element; ϕ_1': volume fraction of Region 1; ϕ_2': volume fraction of Region 2*

The system of equations for calculating the modulus of RVE(2) simplifies to a function of $f(E_{DL}, E_T, \bar{d}, d_t, s, w_t)$:

$$E_{RVE(2)} = \frac{E_{DL}(E_T \bar{d} s + E_T d_t s + E_{DL} \bar{d} w_t + E_T d_t w_t)}{(\bar{d} + d_t)(E_T s + E_{DL} w_t)} \quad \text{(Eq. 22)}$$

where *$E_{RVE(2)}$: modulus of the representative volume element; E_{DL}: modulus of the dental ligament; E_T: modulus of the teeth; s: half the width of the gap between teeth; d_t: thickness of the tooth; $\bar{d}$: half the average distance between teeth in a single file. w_t: width of the tooth section in the RVE (half of the total tooth width)*

After calculating the modulus using each of the four methods noted above, the value for the multicomponent layer was input into the Reuss model again, along with the moduli and volume fractions of the other layers of the model. The results are shown in **Table 6.**

Table 6: The moduli of the beam when each model was applied to calculate the modulus of the multicomponent layer.

	Parameters	Voigt Model	Composite Reuss and Voigt (1)	Composite Reuss and Voigt (2)	Reuss Model
Material	Soft (2 MPa)	2.58	2.27	1.65	1.61
	Medium (10 MPa)	10.47	6.79	3.19	3.04
	Hard (30 MPa)	21.38	10.16	3.78	3.57
File Spacing	0 mm	10.95	10.95	3.42	3.15
	1 mm	10.47	6.78	3.19	3.04
	2 mm	10.05	5.42	3.07	2.98
Depth	+1 mm	3.17	3.07	2.86	2.79
	0 mm	10.47	6.78	3.19	3.04
	-1 mm	6.82	5.63	2.80	2.78

3.6 THEORETICAL STIFFNESS CALCULATIONS

A secondary reason for modeling the chondrichthyan feeding mechanism as simplistic rectangular beams was to enable the calculation of the theoretical stress distribution through the beams. It was possible to approximate the stress distribution through the models using the neutral axis, the moment of the model, the proportional area moment of inertia of the models, and the known material properties of the model components. This was done by developing an equivalent single-material, homogeneous beam model through the use of scaling factors. The stress distribution can then be used to show the role of jaw material, tooth depth, and file spacing in stress distribution in the homologous equivalent beams, and it will also reveal if there should be any theoretical difference between parallel and staggered orientation as it relates to the different model for the rule of mixtures for the loading conditions.

3.6.1 SCALING COMPONENT STIFFNESS

The first step in determining the stress distribution in the models, is to model the system as a layered system where each layer is made of a single homogenous material. To appropriately determine the value of the average modulus of elasticity of the models and develop a homogenous beam, the known moduli for the teeth (E_1), dental ligament (E_2), and jaw cartilage (E_3) are scaled to the dental ligament, the least stiff material, using the scaling factor n_i in **Eq. 23**.

$$n_i = \frac{E_B}{E_A} \qquad \text{(Eq. 23)}$$

where n_i *: scaling factor [unitless]* E_A*: is the least stiff material in the system [MPa],* E_B*: modulus of material with greater stiffness [MPa]*

The values used for these moduli came from the material model compression results reported in **Table 5**. The variable of interest, dentition patterning, occurs on the compressive side of the beam in bending. Consequently, due to the bimodularity of the materials, we decided that the use of the compressive modulus would provide the best representation for the theoretical calculations. For each of the variable tooth depths, the models were constructed as seen in **Figure 38**: teeth and dental ligament (E_{12}), dental ligament (E_2), teeth and jaw cartilage (E_{13}) , and just jaw cartilage (E_3). All other models will use a variation of the 0 mm tooth depth model and vary either the jaw material, or the volume fraction of the teeth as appropriate. The values for E_{12} and E_{13} were calculated using the methods outlined in Section 3.5 for modeling RVE(1) and RVE(2).

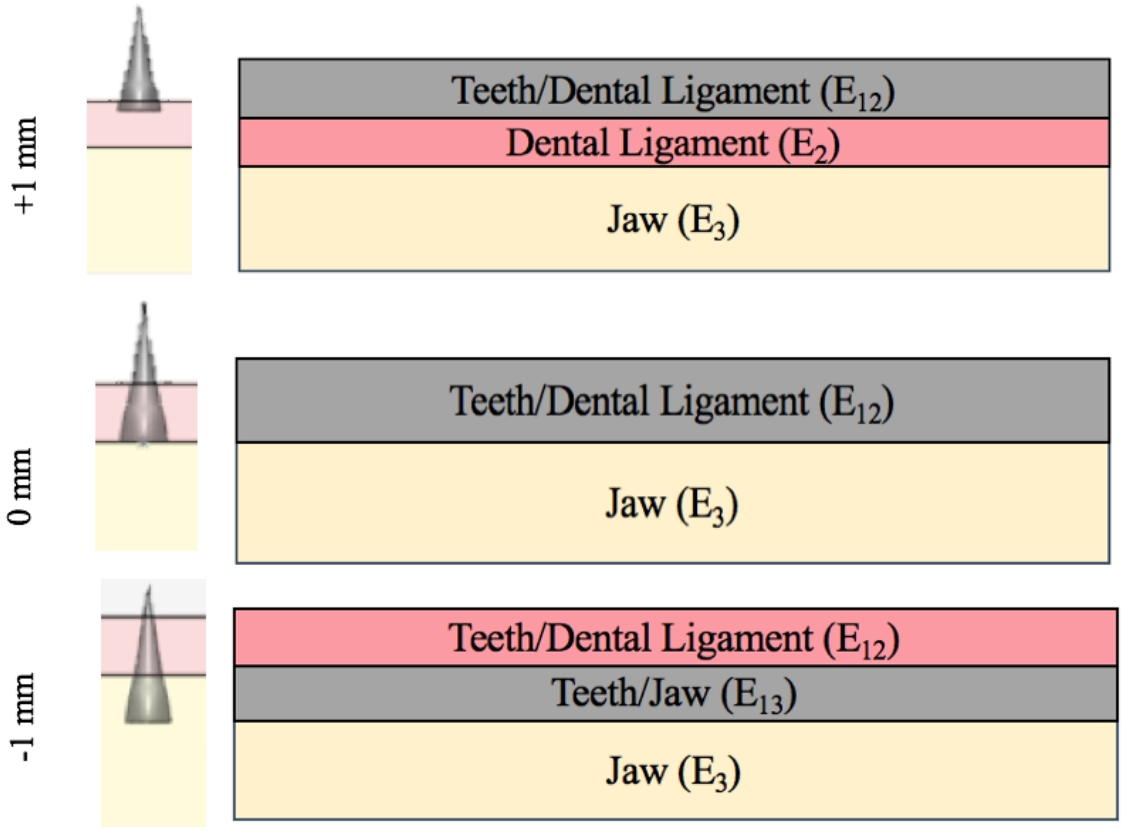

Figure 38: Fundamental composite structure for the three variable tooth depths of the rectangular beam models.

With these variables now established, **Eq. 23** was used to produce the homogenous beams for the models shown in **Figure 39**. When scaling the layers in the rectangular composite system, the thickness was held constant and just the width was adjusted by the scaling factor. The additional width of the scaled layers changes the area moment of inertia for the composite model, because the scaled widths account for the differences in the flexural moduli. The wider layers with the lower moduli are directly comparable to the originally sized layers with their original moduli.

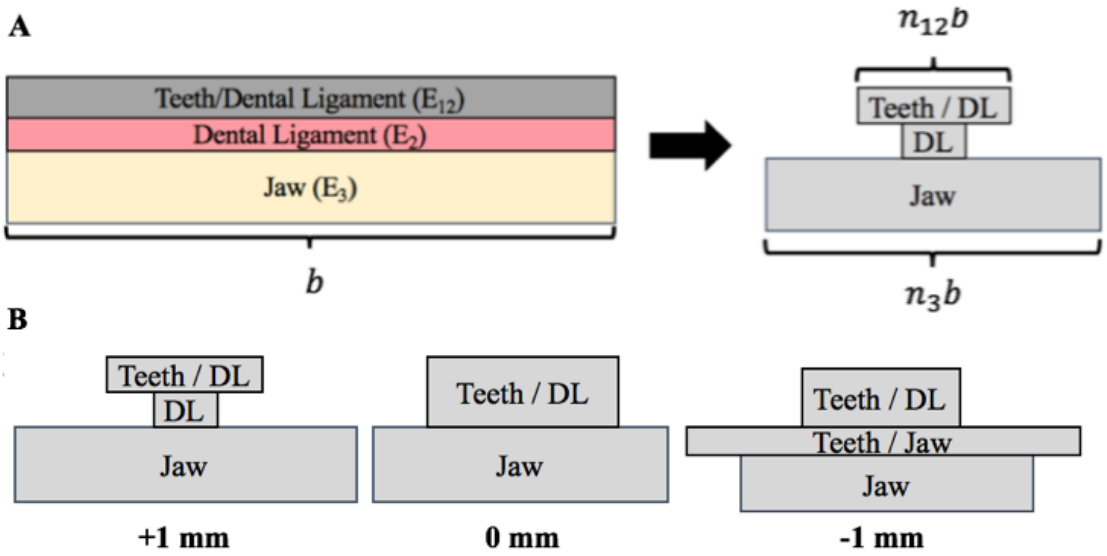

Figure 39: Scaling the composite component geometry to account for the variable Young's Moduli. **A:** The three layered composite for the +1 mm rectangular beam is converted into a scaled homogenous system. **B:** The homogenous beams for the rectangular beam models. **Note:** The areas of the beams are not drawn to scale.

3.6.2 ESTABLISHING THE NEUTRAL AXIS

Having created homogenous representative beams, it is now possible to calculate the neutral axis, area moment of inertia, and moment for each of the beams. The neutral axis will shift due to the positing of the teeth within the feeding mechanism, and this will be a major factor in influencing how stresses are distributed throughout the models. The neutral axis can be determined through the use of **Eq. 24**.

$$\bar{y} = \frac{\sum n_i y_i A_i}{\sum n_i A_i}, \qquad \text{(Eq. 24)}$$

where $\bar{y}$*: neutral axis [mm],* y_i*: the distance from the base of the model to the center of the layer* ***Figure 40*** *[mm],* A_i*: the area of the layer (base x height) [mm*^{2}*],* n_i*: scaling factor*

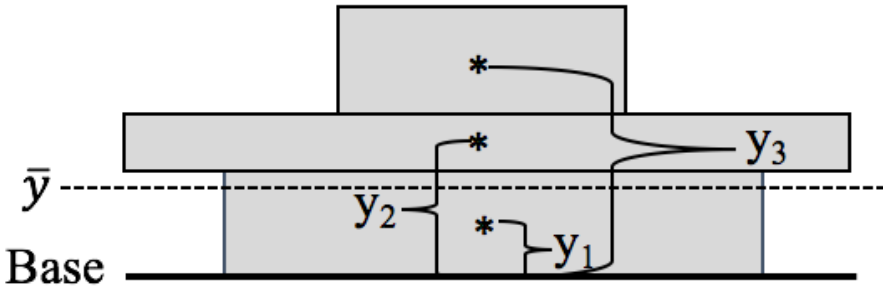

Figure 40: The variable y_i is equivalent to y_1, y_2, and y_3 respectively within the summation. The resulting neutral axis, $\bar{y}$, is represented by the hashed line.

The parameters and results for calculating the scaling factor and neutral axis can be seen in **Table 7** and **Table 8**. When varying the material, the neutral axis shifts closer to the base as the stiffness of the representative jaw material is increased. The variable file spacing also shifted the neutral axis closer to the base as the spacing between the files was

Table 7: Parameters and results for calculating the scaling factor and neutral axis for each set of variables using RVE(1).

	Parameters	Layers	Component Modulus [MPa]	Volume Fraction	Scaling Factor	Neutral Axis [mm]
Material	Soft (2 MPa)	Teeth/Dental Ligament	3.62	0.2682	4.02	2.634
		Jaw	2	0.7318	2.22	
	Medium (10 MPa)	Teeth/Dental Ligament	3.62	0.2682	4.02	1.978
		Jaw	10	0.7318	11.11	
	Hard (30 MPa)	Teeth/Dental Ligament	3.62	0.2682	4.02	1.803
		Jaw	30	0.7318	33.33	
File Spacing	0 mm	Teeth/Dental Ligament	14.82	0.2682	16.47	2.525
		Jaw	10	0.7318	11.11	
	1 mm	Teeth/Dental Ligament	3.62	0.2682	4.02	1.978
		Jaw	10	0.7318	11.11	
	2 mm	Teeth/Dental Ligament	2.41	0.2682	2.68	1.894
		Jaw	10	0.7318	11.11	
Depth	+1 mm	Teeth/Dental Ligament	3.88	0.0536	4.31	1.836
		Dental Ligament	0.9	0.2146	1	
		Jaw	10	0.7318	11.11	
	0 mm	Teeth/Dental Ligament	3.62	0.2682	4.02	1.978
		Jaw	10	0.7318	11.11	
	-1 mm	Teeth/Dental Ligament	2.34	0.2682	2.61	2.61
		Teeth/Jaw	18.78	0.2146	20.87	
		Jaw	10	0.5172	11.11	

Table 8: Parameters and results for calculating the scaling factor and neutral axis for each set of variables using RVE(2).

	Parameters	Layers	Component Modulus [MPa]	Volume Fraction	Scaling Factor	Neutral Axis [mm]
Material	Soft (2 MPa)	Teeth/Dental Ligament	1.12	0.2682	1.23	2.100
		Jaw	2	0.7318	2.22	
	Medium (10 MPa)	Teeth/Dental Ligament	1.12	0.2682	1.24	1.797
		Jaw	10	0.7318	11.11	
	Hard (30 MPa)	Teeth/Dental Ligament	1.12	0.2682	1.23	1.736
		Jaw	30	0.7318	33.33	
File Spacing	0 mm	Teeth/Dental Ligament	1.22	0.2682	1.18	1.805
		Jaw	10	0.7318	11.11	
	1 mm	Teeth/Dental Ligament	1.12	0.2682	1.24	1.797
		Jaw	10	0.7318	11.11	
	2 mm	Teeth/Dental Ligament	1.06	0.2682	1.36	1.792
		Jaw	10	0.7318	11.11	
Depth	+1 mm	Teeth/Dental Ligament	1.42	0.0536	1.57	1.789
		Dental Ligament	0.9	0.2146	1	
		Jaw	10	0.7318	11.11	
	0 mm	Teeth/Dental Ligament	1.12	0.2682	1.24	1.797
		Jaw	10	0.7318	11.11	
	-1 mm	Teeth/Dental Ligament	0.93	0.2682	1.38	2.33
		Teeth/Jaw	12.44	0.2146	13.83	
		Jaw	10	0.5172	11.11	

increased. Finally, for the variable tooth depth, it was calculated that the neutral axis increased as the teeth were moved closer to and embedded in the jaw. The reason the -1 mm models create an upward shift in the neutral axis is due to the influence of the scaling factors, that are directly proportional to the material stiffness, have over the geometry of models. The upward shift of the neutral axis compensates for the larger areas associated with the teeth/dental ligament and teeth/jaw regions respectively found in these models.

3.6.3 AREA MOMENT OF INERTIA CALCULATION

Now that the neutral axis has been calculated, the next step is to determine the area moment of inertia of the cross-sectional area with respect to the neutral axis, through the

use of the parallel-axis theorem. For the rectangular models, **Eq. 25** and **Eq. 26** should be used to calculate the area moment of inertia.

$$\bar{I} = \sum n_i(\overline{I_i} + A_i d_i^2) \ , \qquad \text{(Eq. 25)}$$

where $\bar{I}$: *area moment of inertia for the model [mm^4],* $\overline{I_i}$*: is the area-moment of inertia for each section [mm^4],* A_i*: the area of the layer [mm^2],* $d_i = (\bar{y} - \overline{y_i})$ [mm], $\bar{y}$*: neutral axis [mm],* $\overline{y_i}$*: the distance from the base of the model to the center of the layer [mm],* n_i*: scaling factor*

For a rectangular cross-section, **Eq. 26** can be applied to calculate $\overline{I_i}$ for each of the sections:

$$I_i = \frac{bh^3}{12}, \qquad \text{(Eq. 26)}$$

where $\overline{I_i}$*: the area moment of inertia [mm^4], b: the length of the base for the section [mm], h: the height of the section [mm]*

3.6.4 MOMENT CALCULATION

The fourth step in determining the stress distribution within the beams is calculating the moment for each beam. Each case was modeled as a simply supported beam with a concentrated load at the middle of the span. This is representative of the three-point bend testing that was conducted on the models. Solving for the moment requires data from the three-point bend testing in terms of the maximum force applied during testing. These data were used in **Eq. 27** to give the modulus for each of the scenarios.

$$M = \frac{n_i FL}{4}, \quad \text{(Eq. 27)}$$

Where *M: moment [N*mm], F: maximum force registered during three-point bend testing [N], L: length of the beam (60 mm) [mm], n_i: scaling factor*

3.6.5 STRESS DISTRIBUTION CALCULATION

Now that the neutral axis, area moments of inertia, and moments are known, **Eq. 28** can be used to calculate the stress distribution at the top and bottom surfaces of each layer of the models.

$$\sigma_i = \frac{n_i M y_i}{I} \quad \text{(Eq. 28)}$$

where σ_i*: maximum stress at designated point)[MPa], M: moment [N*mm], y_i: distance of point from neutral axis [mm],* ***Figure 41,*** *(negative values will result in compressive forces at that point and positive values will result in tensile forces at that point), I: area moment of inertia [mm^4], n_i: scaling factor*

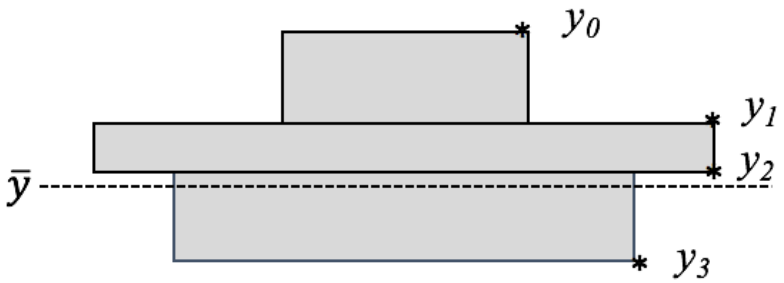

Figure 41: The maximum stress was calculated at each of the points above. The value for each point is equivalent to its distance from the neutral axis, $(\bar{y} - y_i)$. Negative values will result in compressive forces and positive values will be tensile forces.

4. RESULTS AND DISCUSSION

The third phase of the project consisted of three-point bend testing of the anatomical cross-section models, three-point bend and compression testing of the simplified rectangular cross-section models, and theoretical stress distribution calculations. The theoretical analysis in conjunction with the mechanical testing will provide a comprehensive understanding of the variables influencing the apparent flexural modulus, maximum flexural strength, and compressive modulus of the feeding mechanism of chondrichthyans. In addition, it is our hope that the results will provide information and inspiration for use with engineering applications and spawn ideas for further testing and understanding of this system.

4.1 ANATOMICAL CROSS-SECTION MODEL RESULTS

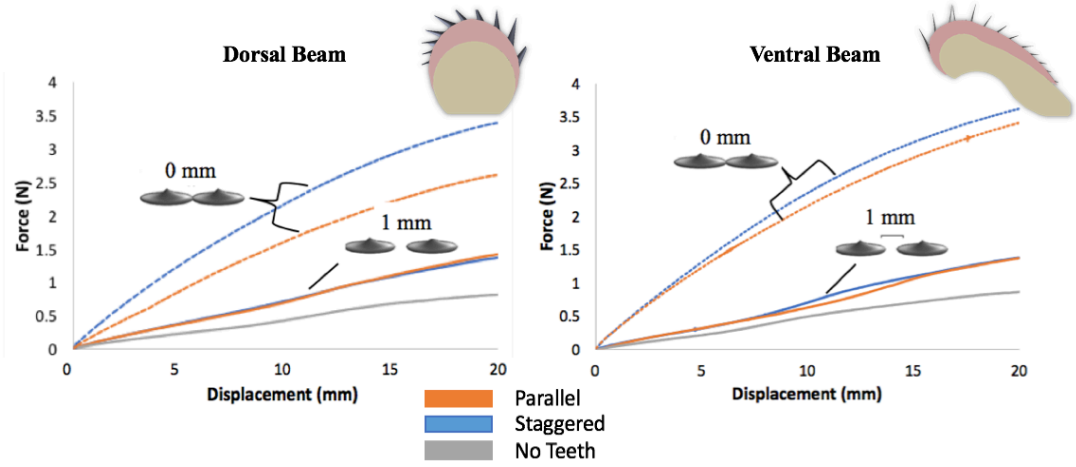

Figure 42: The results from three-point bend testing of the anatomical cross-section samples. The tests were run with a jaw cartilage material with a Young's Modulus of approximately 2 MPa **Left:** This dorsal beam section was tested with files spaced at 0 mm and 1 mm for both parallel and staggered dentition patterns and with no teeth. **Right:** Likewise, this ventral beam section was tested with files spaced at 0 mm and 1 mm for both parallel and staggered dentition patterns and with no teeth.

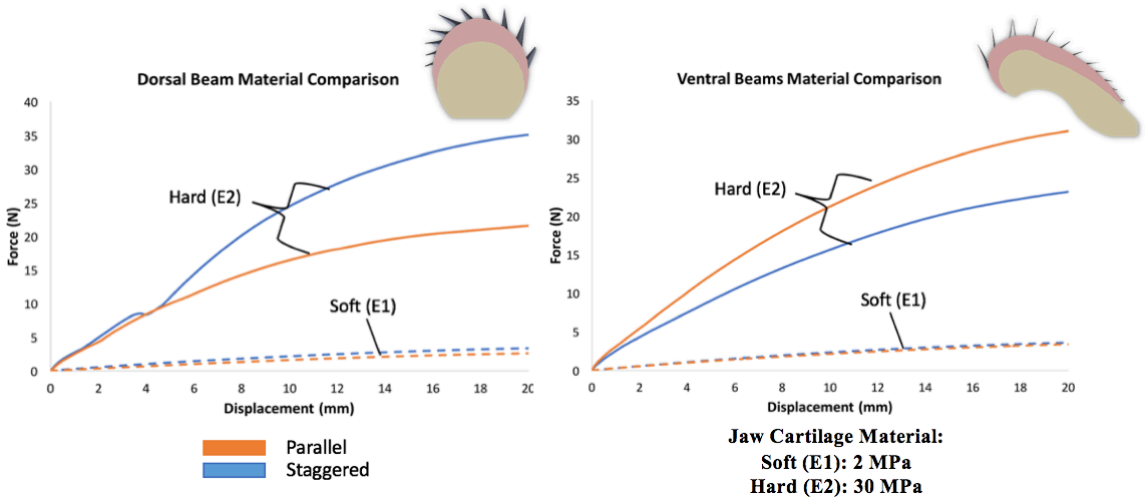

Figure 43: The results from three-point bend testing of the anatomical cross-section samples. The tests were run with a jaw cartilage material with a variable Young's Modulus and a set file spacing of 0 mm **Left:** This dorsal beam section was tested with parallel and staggered dentition patterns for a hard and soft material. **Right:** Likewise, this ventral beam section was tested with parallel and staggered dentition patterns for a hard and soft material.

To gather a basic understanding of how the anatomical cross-section models would perform during testing, a single specimen was printed for each case and analyzed for preliminary results. The three-point bend test results for the anatomical cross-section models are shown in **Figure 42** and **Figure 43** above. The first comparison, shown in **Figure 40**, investigates how the presence of teeth and their spacing within the feeding mechanism influences the stiffness of the model. The test results reveal that adding teeth and decreasing their spacing increases the overall apparent flexural stiffness of the model. The teeth are the stiffest material in the model, so merely adding them will logically increase the stiffness when compared to the case with no teeth. In the case of the 1 mm file spacing, there is little tooth-tooth interaction during bending and only primarily tooth-dental ligament interaction. However, in the case of the 0 mm file spacing, there is a much

greater interaction between the teeth. As the beam is bent, the teeth will be in contact with one another. These contact points result in added resistance to bending and generate an additional stiffening effect. This explains how the decrease in file spacing causes an overall increase in the model stiffness outside of simply increasing the volume fraction of stiffer components. When comparing the parallel and staggered dentition patterns for these models, there is little differentiation between the two for the 1 mm file spacing. This is likely due to the minimal contact between the teeth. Thus, the orientation has very little effect on this set of variables during bending. As for the 0 mm file spacing, the staggered orientation does appear to provide an additional stiffening effect to the model, but there are not enough data from this set of tests to fully draw a conclusion from this result.

In **Figure 43**, the comparison was drawn between a soft (~2 MPa) and hard (~30 MPa) material for both dentition patterns for the representative dorsal and ventral beams. As would be expected, the harder material produced a stiffer beam. However, there was an interesting result when comparing the parallel and staggered orientations for the harder material. In the dorsal beam, as before with the comparison in **Figure 42**, the staggered orientation was slightly stiffer than the parallel. Contrarily, the parallel orientation produced the stiffer material for the ventral beam in **Figure 43**. This result led to the realization that there may be additional variables influencing these models outside of the dentition patterning, such as geometry, tooth depth, and file spacing. Therefore, in an attempt to further isolate the factors affecting the model's stiffness, we decided the best course of action would be to further simplify the models, allowing better control of a number of variables. Consequently, no true conclusions were drawn from these results

gathered, due to the minimal number of samples tested. Rather, these tests served as the preliminary data that guided the research toward more simplified models with better variable control.

4.2 RECTANGULAR MODEL RESULTS AND DISCUSSION

To further investigate the influence that dentition patterning has on the stiffness of the feeding mechanism, three-point bend and compression testing were performed on each of the rectangular beams according to the methods outlined in Section 3.4.1 and Section 3.4.2, respectively. All of the following results were from models that were printed in a single batch for like materials in an attempt to reduce variability. Therefore, there was a total of three batches consisting of the following materials: 1) FLX9770, TangoPlus, and VeroWhite; 2) FLX9750, TangoPlus, and VeroWhite; 3) FLX9795, TangoPlus, and VeroWhite. There were three samples for each variable that were tested in bending and compression. This gave a total of 14 unique variable combinations, 42 total samples, and 84 individual tests. Previous attempts were made to test some of the variables; however, not all of those models were printed in the same batch. Consequently, upon analysis of the results, there was a great deal of variability resulting from inconsistencies in the prints. This issue will be further discussed in Chapter 5, but it is important to note now as it was the reasoning behind the number of models we were able to test. Ideally, more than three specimens for each variable would be tested. However, this was the maximum number that could be printed in a single batch.

4.2.1 MATERIAL COMPARISON

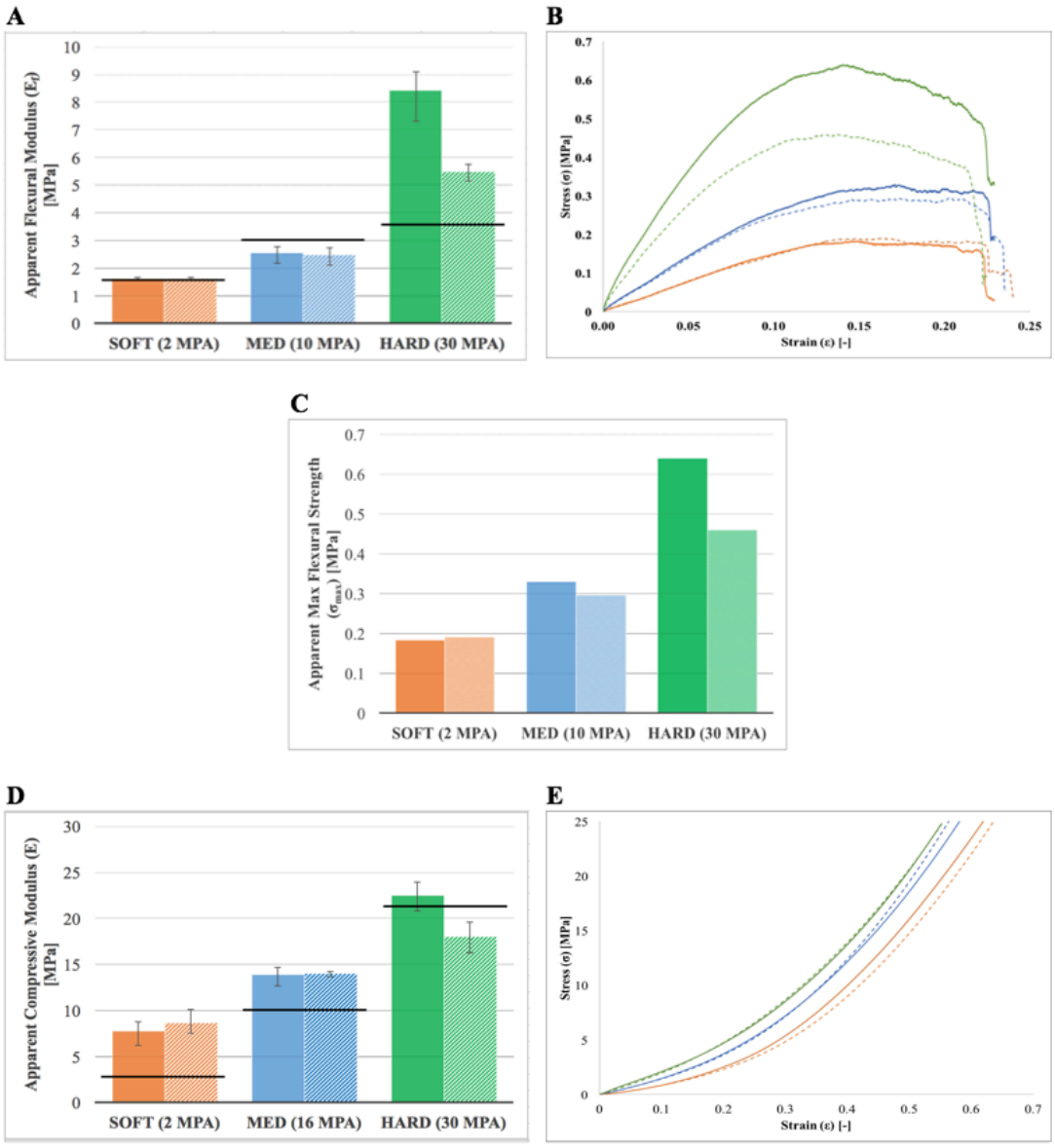

Figure 44: Averaged results for the variable representative jaw cartilage materials. Solid lines and columns are the parallel dentition patterns and the hashed lines and columns are the staggered dentition patterns. There were three samples for each variable. **Constants:** File spacing – 1 mm; Tooth depth – 0 mm. **Variable:** Representative jaw cartilage material **A:** The average apparent flexural modulus for each material compared against the approximated modulus using the Reuss model for the rule of mixtures (black bar) **B:** A representative stress-strain curve for the three-point bend testing of the variable material models. **C:** The average max flexural strength. **D:** The average compressive modulus for each material compared against the approximate modulus using the Voigt model for the rule of mixtures. **E:** A representative stress-strain curve for the compression testing of each of the materials. Error bars denote the range of the results.

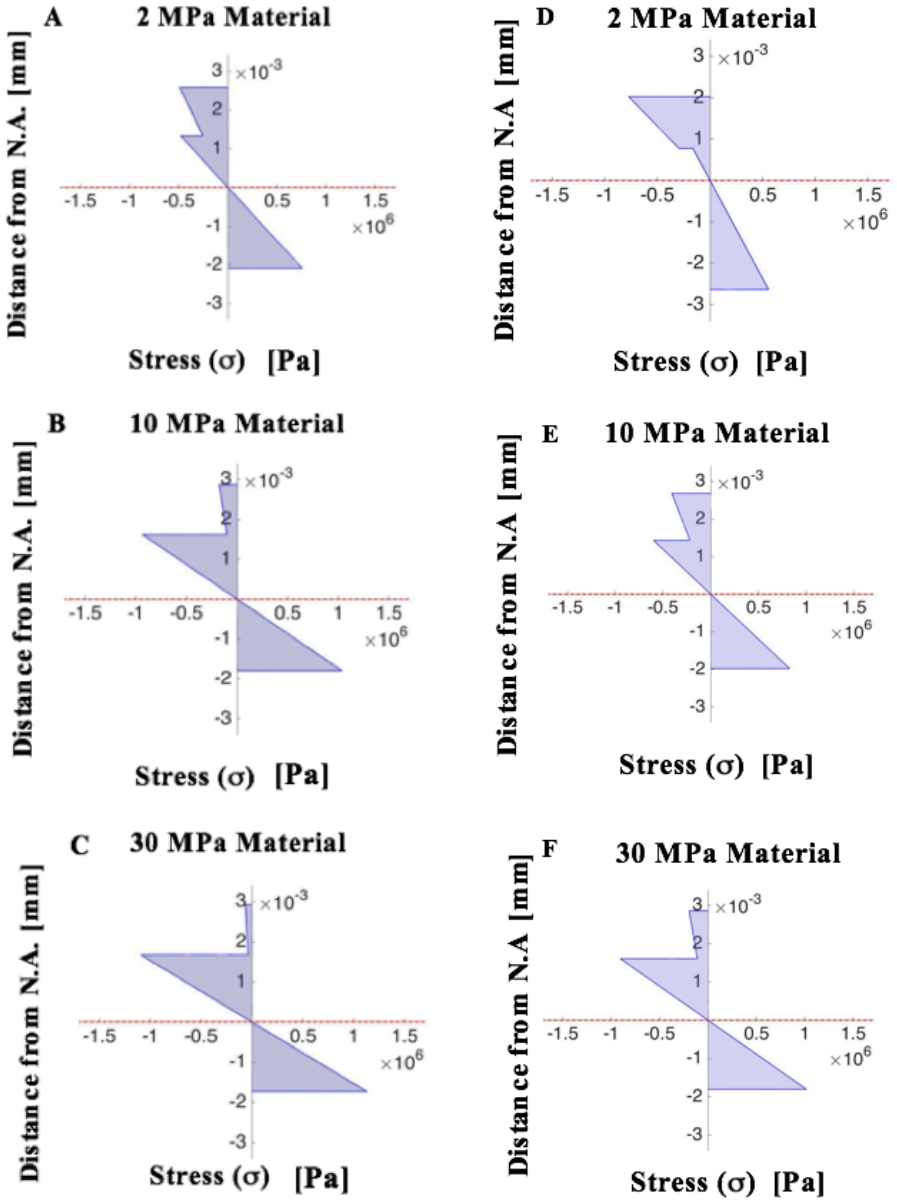

Figure 45: Theoretical stress distribution calculations for the variable jaw cartilage material. The x-axis is the neutral axis for each case. The parallel and staggered dentition patterns were modeled using representative volume element model RVE(1) and RVE(2), respectively. **A:** Approximation of the stress-distribution for the 2 MPa jaw cartilage material with a staggered dentition pattern. **B:** Approximation of the stress-distribution for the 10 MPa jaw cartilage material with a staggered dentition pattern. **C:** Approximation of the stress-distribution for the 30 MPa jaw cartilage material with a staggered dentition pattern. **D:** Approximation of the stress-distribution for the 2 MPa jaw cartilage material with a parallel dentition pattern. **E:** Approximation of the stress-distribution for the 10 MPa jaw cartilage material with a parallel dentition pattern. **F:** Approximation of the stress-distribution for the 30 MPa jaw cartilage material with a parallel dentition pattern.

The results from the three-point bend and compression testing of the variable representative jaw material can be seen in **Figure 44**. These results were similar to those seen in the anatomical cross-sectional models in Section 4.1. The apparent flexural modulus of the models increases as the modulus of the jaw material increases. It would be expected that increasing the stiffness of a component would subsequently increase the stiffness of the system. Likewise, the maximum flexural strength mirrored these results. The same trend occurred in the compression testing results in **Figure 44D.** However, the increase in moduli from the soft to the hard material was less dramatic in the compression testing. This is due to the differences in the stress distributions between bending and compression. Only compressive forces are experienced during compression testing. However, in bending there are compressive forces above the neutral axis and tensile forces below. These vary linearly through the system with abrupt changes at material interfaces.

Figure 45 shows the stress distribution for each of the cases. There is a piecewise linear distribution of stress throughout the models, where the stress through each material has the linear distribution. The area moment of inertia plays an important role in the stress distribution. As can be seen from **Eq. 28**, the stress is inversely proportional to the area moment of inertia, $\sigma \propto I^{-1}$. Therefore, an increase in the area moment of inertia will result in a subsequent decrease in the stress for that particular region. As the stiffness of the jaw cartilage material is increased, the jaw region of the model experiences a decrease in its area moment of inertia and a subsequent increase in stress. Subsequently, the 2 MPa material model experiences a comparatively large compressive stress on the top surface of the tooth/dental ligament layer and a lower compressive stress and tensile stress on the top

and bottom surface of the jaw layer, respectively. This effect is very apparent for the parallel dentition pattern shown in **Figure 45D**, where the modulus of the tooth/dental ligament layer was approximated using RVE(1), which gave this layer a higher modulus value. Consequently, higher levels of stress were experienced in this region.

4.2.2 FILE SPACING COMPARISON

The results from the three-point bend and compression testing of the variable tooth file spacing can be seen in **Figure 46**. These results show that the flexural modulus and the maximum flexural strength were the greatest for the 0 mm file spacing. Also, there was little discernable difference between the flexural modulus and maximum flexural strength of the 1 mm and 2 mm file spacing scenarios. The reasoning behind these results is the interaction between the teeth causes a stiffening effect, as was described above for the anatomical cross-sectional models, in Section 4.1. Consequently, in the case of the 0 mm file spacing, there is a constant contact between teeth in adjacent files. This contact between the stiff material of the teeth causes additional stiffening of the whole system. However, for the files spaced at 1 mm and 2 mm, there is enough space between the teeth that there is very minimal interaction between adjacent files. The primary interaction is between the teeth and the dental ligament. Since the stiffness of the dental ligament is much less than that of the teeth, its interaction has a much less dramatic effect on the stiffness of the system. In analyzing the results of the compressive modulus, it is interesting to note that

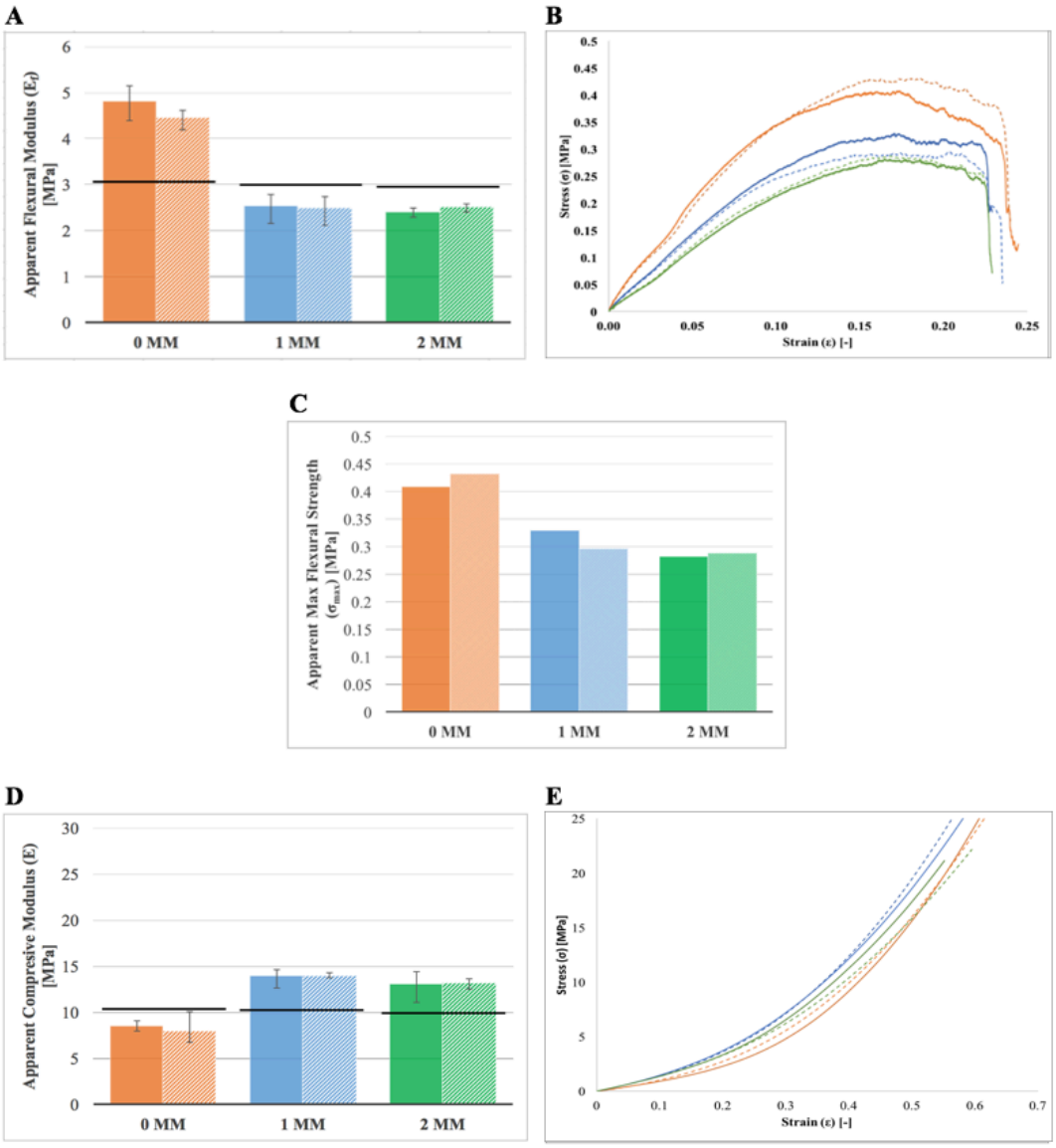

Figure 46: Averaged results for the variable tooth file spacings. Solid lines and columns are the parallel dentition patterns and the hashed lines and columns are the staggered dentition patterns. There were three samples for each variable. **Constants:** Jaw material – FLX9770; Tooth depth – 0 mm. **Variable:** File spacing **A:** The average apparent flexural modulus for each file spacing compared against the approximated modulus using the Reuss model for the rule of mixtures (black bar) **B:** A representative stress-strain curve for the three-point bend testing of the variable file spacing models. **C:** The average max flexural strength. **D:** The average compressive modulus for each file spacing compared against the approximate modulus using the Voigt model for the rule of mixtures. **E:** A representative stress-strain curve for the compression testing of each of the file spacings. Error bars denote the range of the results.

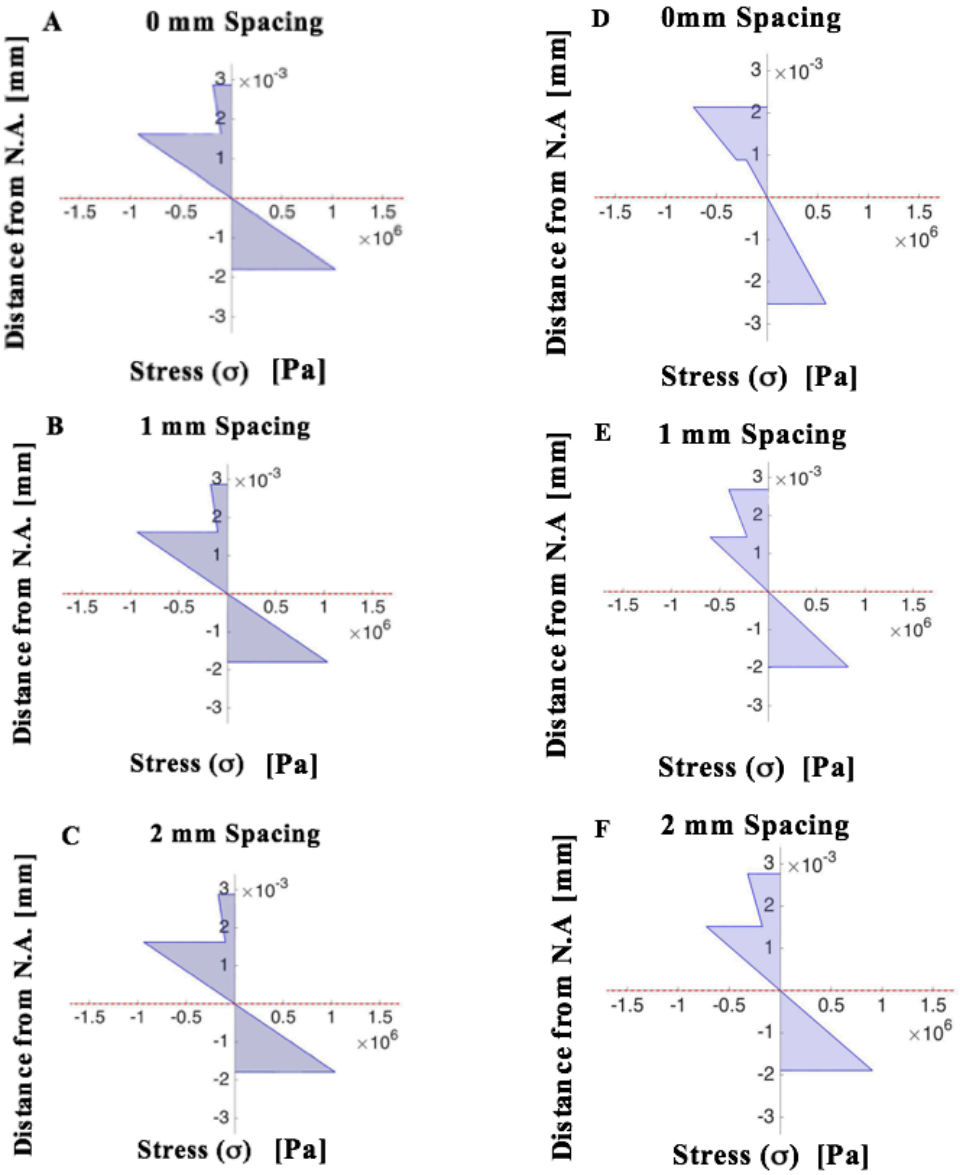

Figure 47: Theoretical stress distribution calculations for the variable jaw cartilage material. The x-axis is the neutral axis for each case. The parallel and staggered dentition patterns were modeled using representative volume element model RVE(1) and RVE(2), respectively. **A:** Approximation of the stress-distribution for the files spaced at 0 mm with a staggered dentition pattern. **B:** Approximation of the stress-distribution for the files spaced at 1 mm with a staggered dentition pattern. **C:** Approximation of the stress-distribution for the files spaced at 2 mm with a staggered dentition pattern. **D:** Approximation of the stress-distribution for the files spaced at 0 mm with a parallel dentition pattern. **E:** Approximation of the stress-distribution for the files spaced at 1 mm with a parallel dentition pattern. **F:** Approximation of the stress-distribution for the files spaced at 2 mm with a parallel dentition pattern.

the 0 mm file spacing had the lowest compressive modulus. However, again the 1 mm and 2 mm file spacing shared very similar results. The reason the compression results do not follow the same trend as the bending results is due to non-uniform compressive forces in the model. During compression, localized tensile and shear forces occur at material interfaces. Consequently, stress is concentrated around the teeth creating a reduction of apparent area. This effect is amplified as the file spacing is decreased and the number of teeth in the model increases.

For this case, the variations between the stress distributions were minuscule and generally insignificant for the staggered dentition patterning seen in, **Figure 47A-C**. As noted above, the stress distribution is largely influenced by the area moment of inertia, which is, in turn, influenced mainly by the positioning of the neutral axis. Since there was almost no change in the positioning of the neutral axis for these cases, there was subsequently very little difference in the distribution of stresses. Similar results were also seen for the parallel dentition pattern in **Figure 47E-F**. However, for **Figure 47D**, the use of RVE(2) to model the 0 mm file spacing creates a relatively large increase in the modulus of the tooth/dental ligament region. This creates an upward shift in the neutral axis and an increase in stress distributed through the tooth/dental ligament region.

4.2.3 DEPTH COMPARISON

The results from the three-point bend and compression testing of the variable tooth depth can be seen in **Figure 48**. These results appear to signify that the depth of the teeth

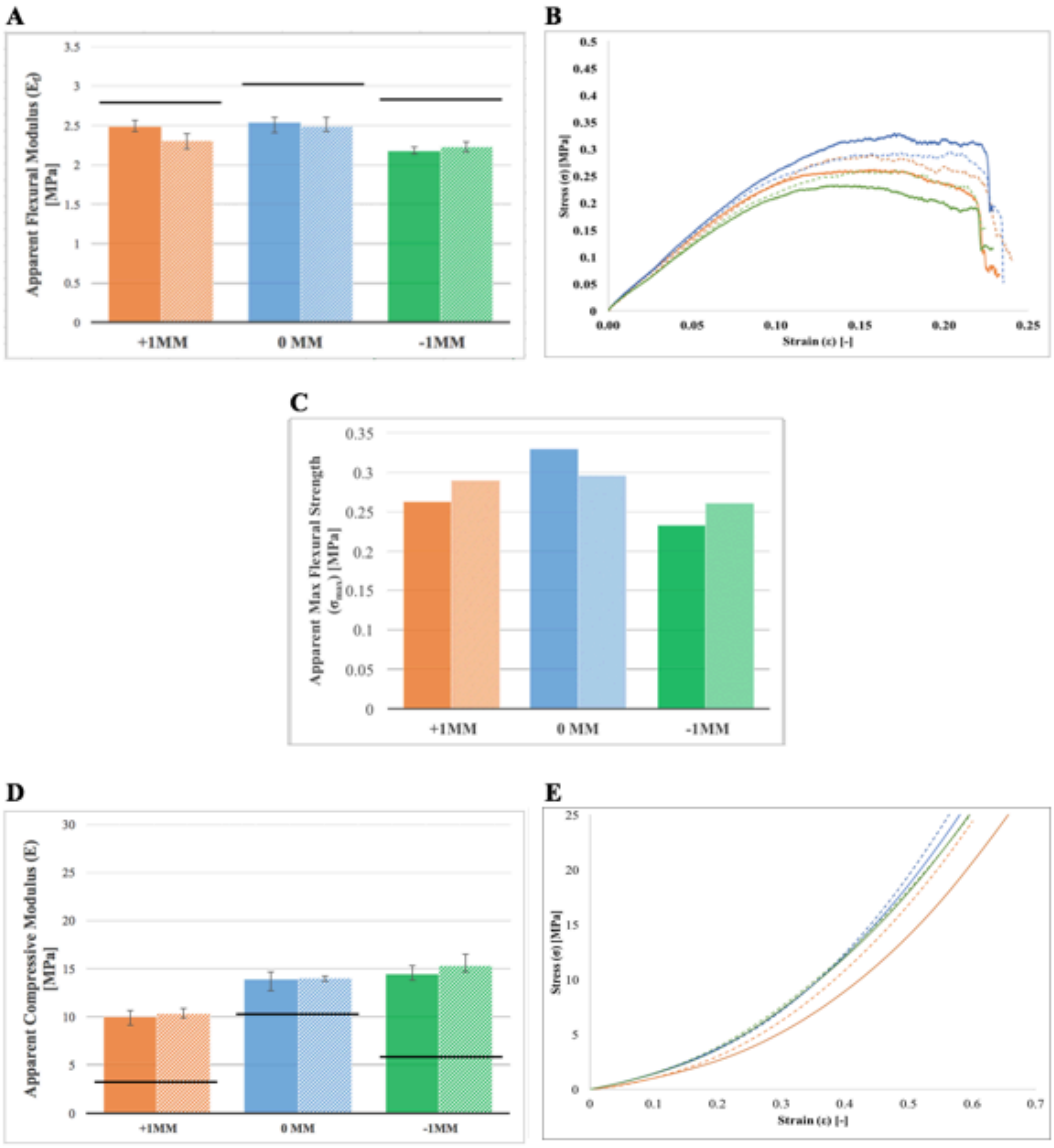

Figure 48: Averaged results for the variable tooth depths. Solid lines and columns are the parallel file orientations and the hashed lines and columns are the staggered file orientation. There were three samples for each variable. **Constants:** Jaw material – FLX9770; File spacing – 1 mm. **Variable:** Tooth depth **A:** The average apparent flexural modulus for each tooth depth compared against the approximated modulus using the Reuss model for the rule of mixtures (black bar) **B:** A representative stress-strain curve for the three-point bend testing of the variable tooth depth models. **C:** The average max flexural strength. **D:** The average compressive modulus for each tooth depth compared against the approximated modulus using the Voigt model for the rule of mixtures (black bar). **E:** A representative stress-strain curve for the compression testing of each of the tooth depths.

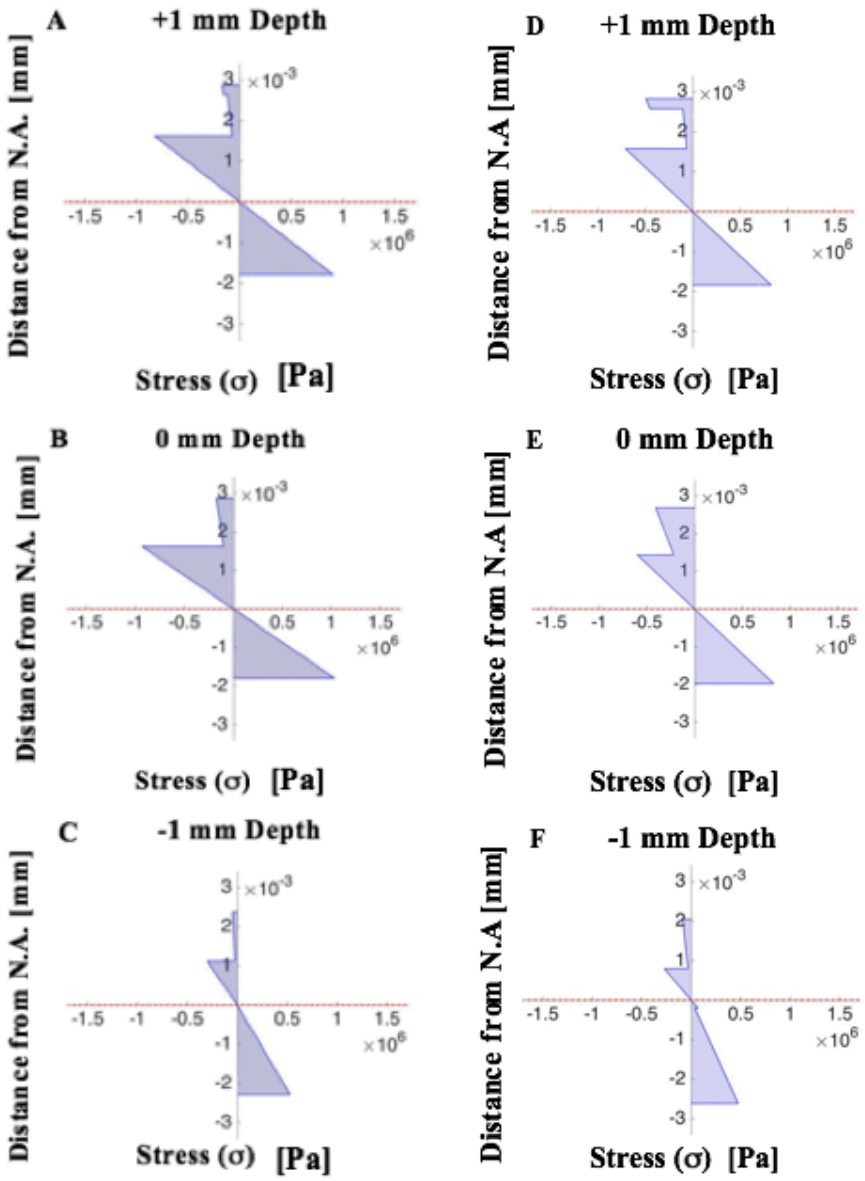

Figure 49: Theoretical stress distribution calculations for the variable jaw cartilage material. The x-axis is the neutral axis for each case. The parallel and staggered dentition patterns were modeled using representative volume element model RVE(1) and RVE(2), respectively. **A:** Approximation of the stress-distribution for the +1 mm tooth depth with a staggered dentition pattern. **B:** Approximation of the stress-distribution for the 0 mm tooth depth with a staggered dentition pattern. **C:** Approximation of the stress-distribution for the -1 mm tooth depth with a staggered dentition pattern. **D:** Approximation of the stress-distribution for the +1mm tooth depth with a parallel dentition pattern. **E:** Approximation of the stress-distribution for the 0 mm tooth depth with a parallel dentition pattern. **F:** Approximation of the stress-distribution for the -1 mm tooth depth with a parallel dentition pattern.

had a minimal influence on the apparent flexural modulus and maximum flexural strength. However, there was a distinct difference between the compressive modulus of the +1 mm depth and the 0 mm and -1 mm depth cases. For the +1 mm case, the dental ligament is the main component in the system being compressed. The teeth and jaws can be thought of as rigid bodies distributing the load through the much softer material of the dental ligament. For the other two cases, there is very little compression of the dental ligament. Since the teeth rest on or are embedded in the jaw, there is a large amount of contact between the materials. This creates abrupt changes in material properties between two relatively stiff components. Consequently, these contact interactions between the teeth and jaw, increase the overall compressive modulus of the system through the same contact stiffening mechanism described previously.

Again, the area moment of inertia plays the largest role in influencing the stress distribution. The greatest compressive force occurs at the top edge of the jaw in each of the scenarios. Likewise, the greatest tensile force occurs at the bottom edge of the jaw. Consequently, the jaw is bearing almost all of the stress. Upon investigating the graphs in **Figure 49**, it is apparent that the -1 mm tooth depth has the lowest compressive and tensile stress values at the edges of the jaw. Inherently, it is desirable to avoid large peaks in stress, especially since the cartilaginous jaws of chondrichthyans lacks the ability to repair itself upon damage [39]. However, it was the socketed teeth that had the lowest tensile and compressive stress in the jaw. This could mean that the loose attachment of teeth is more related to the feeding behavior of chondrichthyans rather than any mechanical advantage associated with the location of the teeth within the feeding mechanism.

4.2.4 PARALLEL VERSUS STAGGERED DENTITION PATTERNS

Finally, the last variables analyzed, and the primary focus of the research was the parallel and staggered tooth file orientations. The effects can be seen in **Figure 44**, **Figure 46**, and **Figure 48**. It appears that the orientation of the files has a minimal influence on the properties of the feeding mechanism. Only for one case, the hard (~30 MPa) material in the rectangular beams, did the values for the parallel and staggered orientations not occupy the same range of values. This same result also occurred in the ventral anatomical cross-section model. The result can be explained by the localized forces that occur at the material interfaces. The forces are better distributed in soft (~2 MPa) material and medium (~10 MPa) material, so the effects are not as obvious. However, with the hard (~30 MPa) material, stresses become localized around the teeth. With the parallel dentition pattern, the majority of the force is localized around the teeth, the stiffest part of the model. Consequently, the model behaves as a stiffer system than if the forces were more evenly distributed throughout the model, as occurs with the staggered dentition pattern.

Also, by applying the information learned from the results of the variable file spacings, it can be hypothesized that tooth-tooth contact interaction is a primary factor in model stiffness. Applying this concept to the parallel and staggered file arrangements, it can be determined that, during pure bending with the force normal to the teeth, there will be the same number of contact points between the teeth per file. Consequently, the orientation of the files will not have a major influence on flexural stiffness or compressive stiffness under these loading conditions.

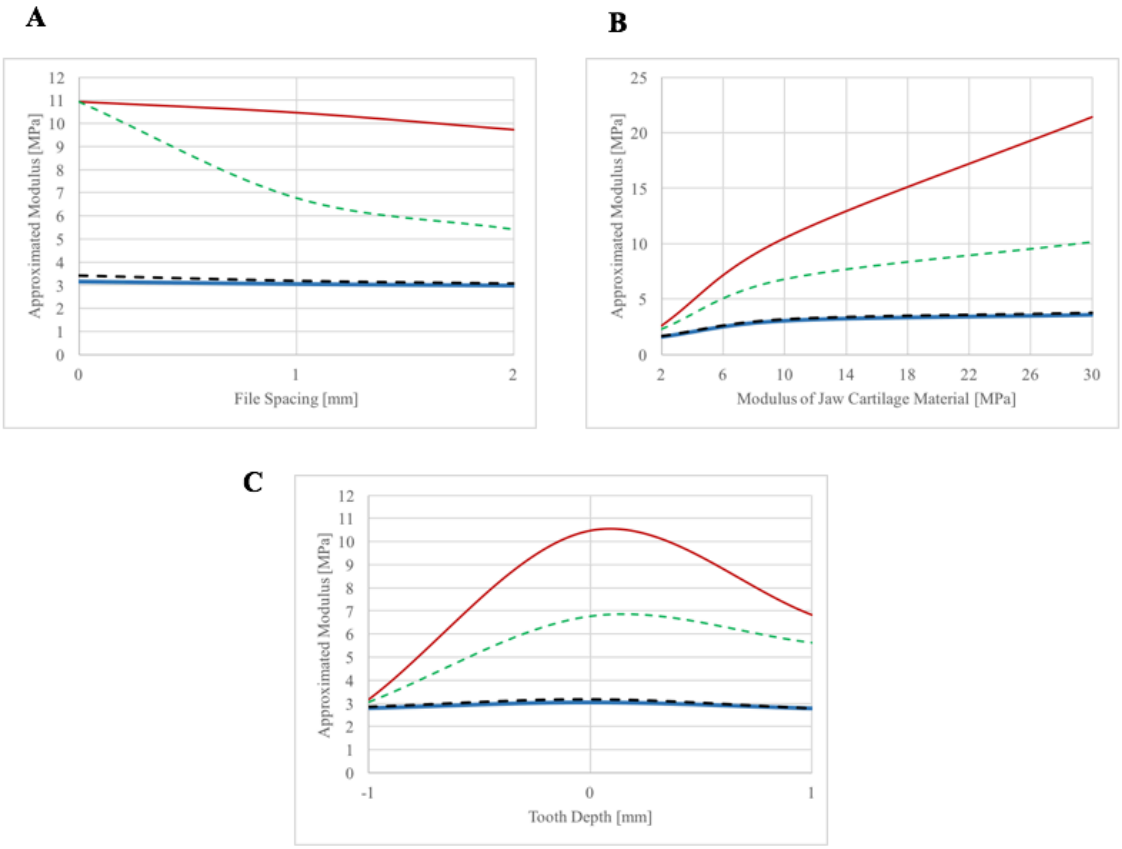

Figure 50: The approximated moduli for each of the four models: Voigt – red; RVE(1) – green, RVE(2) – black; Reuss – blue. **A:** The approximated moduli values for the variable file spacings. **B:** The approximated moduli for the variable jaw cartilage material. **C:** The approximated moduli for the variable tooth depth

RVE(1) and RVE(2) models predicted that the modulus for the parallel dentition pattern would be greater than the modulus for the staggered pattern. However, the results from mechanical testing thus far suggest that, for most cases, there is an insignificant difference in the apparent flexural moduli between parallel and staggered dentition patterns. RVE(1) and RVE(2) provide better models for approximation of the results when compared to the Voigt and Reuss models alone. The Voigt and Reuss models provide upper and lower bounds for the approximations, while RVE(1) and RVE(2) provide approximations that are between the two (**Figure 50**). RVE(1) and RVE(2) account for

some of the nonhomogeneous nature of the multicomponent layers. However, it is still a simplistic model that requires assumptions that cause it to over predict the effects of dentition patterning on the models.

5. CONCLUSIONS

Upon analysis of the results, we were able to draw several conclusions relating to the factors influencing jaw rigidity and our general experimental methods. Overall, we failed to find evidence to support our original hypothesis that the staggered dentition pattern within the chondrichthyan feeding mechanism would produce a more rigid structure in bending and compression. Thus, there are differences between the overlapping elements seen in abalone nacre, mineralized collagen fibrils, and multilayered silica glass sponges, compared to the rigid staggered element patterning of the chondrichthyan dentitions [8,10,18]. Therefore, the chondrichthyan feeding mechanism does not provide a more macro-level understanding of the structural rigidity of the brick-and-mortar structure of abalone nacre in pure bending and compression, as was hoped. **Figure 44**, **Figure 46**, and **Figure 48** show that there is little discernable difference between the parallel and staggered patterning. The only instance where the results of the parallel dentition patterning fell outside the range of the staggered was for the hard (~30 MPa) material in **Figure 44**. During bending and compression, the forces become localized around the teeth. In the case of the hard (~30 MPa) material, it does not disperse these localized forces as well as the other two, less stiff, materials. Consequently, the localization of the forces around the teeth, the stiffest material in the model, results in the system being stiffer than if the forces were evenly distributed. Subsequently, the staggered dentition pattern has less of this stiffening effect as it more evenly distributes the forces through the model. In addition, during bending, the staggered dentition pattern has fewer teeth in the central file that is directly experiencing the load. Consequently, the staggered dentition pattern exhibits a lower

stiffness in bending. Even upon examination of the stress-strain curves, it can be seen that the bending and compression curves for the staggered patterning are relatively equivalent to that of the parallel pattern for almost every case. Consequently, we can say with a degree of confidence that the patterning of the teeth has a minimal influence over the apparent flexural modulus, apparent flexural strength, and compressive modulus of the models.

While the dentition patterning failed to have a major impact on the rigidity of the feeding mechanism during bending and compression, there were several factors that did. The representative jaw cartilage material and file spacing had an impact on the apparent flexural modulus, maximum flexural strength, and compressive modulus. This is linked to the volume fractions of stiff materials and contact interactions at the material interfaces. In addition, the tooth depth also had an influence on the compressive modulus. From these results, it appears that the volume fraction of stiff components, contact interactions between the rigid component materials, and localization of forces are the factors largely responsible for the increases in the stiffness of the models. As the files of teeth are brought closer together and as the teeth are placed adjacent to and then embedded in the jaw, the amount of contact between rigid components increases. This, consequently, creates a stiffening effect in the models. Likewise, the concentration of forces around the teeth results in the model behaving as a stiffer system.

5.1 IMPACT OF RESULTS

Overlapping elements, found in systems such as abalone nacre and silica glass sponges, have increased rigidities as a result of the overlapping nature of the components

[8,10,17,18]. This is largely due to the constraints brought about by impermeable rigid elements [66]. When overlapping layers are present, contact during bending occurs between plates within a single layer and between plates in adjacent layers. The overlapping nature of these layers causes them to interact with one another during bending, in addition to the added benefit of crack deflection that leads to increased toughness. If the structures were, rather, oriented in parallel, there would be uninterrupted lines of the less rigid organic bonding matrix running completely through the system. Upon loading, the system would initially bend along these lines of the less rigid material. There would be some stiffening of the system as the plates within a single layer began to contact one another; however, the interaction between adjacent layers would still be lost.

It is possible to relate the importance of contact interactions of the overlapping elements to its importance in rigid staggered element patterning. As seen from the results of this study, the instances that displayed an increase in flexural moduli were those that had increase tooth-tooth or tooth-jaw contact. This demonstrates the importance of contact interactions of surface patterns as they relate to the properties of the system. However, when comparing the parallel and staggered dentition patterns, there is no difference in the number of contact points. Unlike the overlapping layer, in which adjacent layers are interacting with one another, the surface pattern of the teeth only interacts with adjacent teeth on a single layer. The only influence that dentition patterning had on the results was through the differences of localized force dispersion. However, this only proved to be an important factor when the teeth were in direct contact with the hardest jaw material, which does not occur naturally in chondrichthyans as the teeth are embedded in the dental

ligament above the surface of the jaw. Therefore, the dentition patterning should play a very minimal role in the mechanical properties associated with pure bending and compression.

Though we originally hypothesized the staggered orientation would out perform the parallel, positive conclusions can still be drawn from the fact this hypothesis was incorrect. Primarily, both parallel and staggered dentition patterns are found in nature in chondrichthyans and sometimes even within the same feeding mechanism. Consequently, these results show that the two perform relatively equally as well under bending and compressive loads, thus neither is at a mechanical disadvantage under these loading conditions.

The lack of impact the file orientation exhibited in this research leads to new questions relating to the reasons for parallel or staggered dentition patterns in the feeding mechanism. Due to the elongated oval shape of the base of the tooth, the staggered orientation does have the potential for a higher degree of packing. However, it has yet to be determined whether the file orientation is related to growth and development, feeding, the mechanical behavior of the system, or a combination of the three. In terms of growth and development, the higher degree of packing allows more teeth to fit in the feeding mechanism. This would be a very advantageous characteristic of chondrichthyans that either preyed on hard food and frequently lost teeth or had a slow replacement rate of teeth. The greater degree of packing would, thus, reduce the effects felt by losing or damaging a tooth, as the greater number of teeth would better be able to compensate for the loss. Also, during feeding, the teeth passively depress and rotate inward when contacting an

impenetrable surface to create a flat crushing surface [27,34,35]. The staggered dentition pattern could theoretically be more efficient in passively depressing as there would be less interference from surrounding teeth in the same file. Instead, the dentition pattern could still be more related to the forces undergone during feeding. There are three primary types of feeding methods for elasmobranchs: suction feeding, biting, and ram feeding [58]. With each of these feeding methods, the feeding mechanism of elasmobranchs are experiencing a number of loading conditions. They can experience compression [59,60], shear [61,62], and torsional forces from biting and tearing at prey [58]. The results from this research revealed that the dentition patterning had very little influence on the stiffness of the system in relation to pure compressive forces. However, there is the possibility that the other loading conditions could reveal some advantages and disadvantages associated with the different dentition patterns. It is possible that the staggered dentition pattern provides better resistance to torsional forces or has better force distributions with fewer areas of stress concentration. For now, these can only be hypothesized and would need to be verified through future work and testing.

The only major conclusion drawn from the results of the stress distribution calculations was how the socketed tooth had the best stress distribution with lower peak tensile and compressive forces in the jaw. This suggests that the chondrichthyan feeding mechanism is not solely optimized for mechanical performance. Rather, these data suggest that the ability of the teeth to move within the feeding mechanism outweighs the mechanical advantages that would be associated with having socketed teeth.

5.2 IMPACT OF TESTING PARAMETERS

In order to isolate individual variables associated with chondrichthyan dentitions and their positioning within the feeding mechanism, it was necessary to generate our own models rather than test natural specimens. In addition, due to the complex nature of the feeding mechanism geometry, it was necessary to use models based on simple geometric shapes to adequately control variables and relate their tested values to their theoretical approximations. There are pros and cons that can be associated with this procedure.

For the positive outcomes, modeling and 3D printing our own samples provided access to an unlimited number of samples without having to harvest any animals for testing. This characteristic allowed us to collect enough data to model the system with a range of variables while not harming any sharks. However, most importantly, solid body modeling and printing our own samples allowed for very precise control over variable and allowed for the testing of parameters outside of those found in nature. If we had tested samples of actual chondrichthyan feeding mechanisms, we would have needed numerous samples from multiple species to encompass the necessary parameters. By doing so, a great deal of variability would have been introduced in terms of variable material properties, geometries, patterning of teeth, and spacing of the teeth, among others. Producing our own models allowed for precise control of each of these variables and allowed a better means to establish trends associated with a single variable.

However, due to the complex geometry of the feeding mechanism, the geometry had to be greatly simplified during the modeling process. During this process, the influences of tooth size, tooth angle, and jaw geometry are all lost. These are characteristics

that have the potential to also play a role in the mechanical properties of the system, but the removal of these characteristics was necessary to reduce the variability in the models. Nevertheless, we hypothesize this should only prove to be a minor drawback of the modeling process and should not have a major influence on the trends we established for the different variables in the previous chapter; however, these variables will be reintroduced in future work to confirm this fact. The major source of issue with creating our own models was with the 3D prints themselves. Printing all of the models became an expensive process, and we realized that there was a relatively high amount of variability between different batches of prints. We attempted to limit the variables to which the models were exposed, such as time from print to testing, storing temperature, and orientation of the models during printing. However, UV exposure [63,64], space between models during printing [63], location on the build platform [64], and variability in the photopolymer material properties [54] are all characteristics that have an effect on the material properties of the final print. Stratasys reports a fairly wide range of material properties in their material data sheets, thus acknowledging the variability in the material properties of the photopolymers [54]. We noticed this directly when testing models that were printed in separate batches. The apparent flexural modulus of the first batch was almost double that of the second batch of models. Therefore, a third set was printed, and all of the models of like materials were printed in the same batch. This did greatly reduce the degree of variability, but it also limited the number of samples due to the size of the build platform. Therefore, only three models for each set of variables could be printed. While this number

of samples is less than ideal, it is what needed to be done to limit the variability of the models.

5.3 IMPACT OF MODELING METHODS

In this research, we approximated the moduli of the multicomponent layers using four different methods: Reuss model for the rule of mixtures, RVE(1) model, RVE(2) model, and the Voigt model for the rule of mixtures. The Reuss model acts as the lower bound of the approximations, while the Voigt model is the upper bound. These two are very simplistic approximations that do not take the nonhomogeneity of the multicomponent layer into account. RVE(1) and RVE(2) attempt to compensate for this by dividing the layers into representative volume elements and combining the Voigt and Reuss models to approximate the moduli of each element. Due to the orientation of force during testing, it was found that the first three modes of approximation best model the flexural moduli, while the Voigt model best models the compressive moduli. However, there are a several shortcomings associated with these approximations. The materials being tested are not perfect. There is porosity in the material, roughness at surface interfaces (results in incomplete bonding of the materials), and minor imperfects of the part related to dimensional tolerances. These are some of the major factors that cause the apparent flexural modulus to be lower than approximated. In compression, the models do not account for the localization of stresses around the teeth. Therefore, the approximated moduli tend to be lower than the values reported from testing. Finally, RVE(1) and RVE(2) attempt to account for the nonhomogeneous nature of the multicomponent layers and account for the

dentition patterning. While these are better approximations than the Voigt and Reuss modes alone, they still have shortcomings in terms of geometric oversimplification and the inability to account for non-compressive forces and material imperfections.

5.4 INTELLECTUAL MERIT

Bio-inspired design is a growing field that has provided benefits to both the biology and engineering fields. This research provided a novel investigation into rigid staggered element patterning and worked to bridge the research gap between the nano- and macro-scale research on the chondrichthyan feeding mechanism. The research gave a better understanding of the principal factors influencing the flexural and compressive modulus of a composite system with rigid element patterns. In addition, previous dietary and feeding studies on chondrichthyans only investigated single tooth models [25,27]. Consequently, this research of a polydontic model provides novel insight into the influences of dentition patterning and spacing as they relate to the overall rigidity of the feeding mechanism.

5.5 BROADER IMPACT

The chondrichthyan feeding mechanism can be thought of as a composite system composed of a semi-rigid base (jaw), a soft core (dental ligament), and a series of rigid tiles (teeth) on the surface. Consequently, the knowledge gained through this study may be applied to engineering systems, such as methods for stiffening beams or flexible body armor designs. Other biological systems, have been studied for use with bio-inspired body

armor, and two of the results from this study could potentially add to this field of bio-inspired body armor [65].

The first is the relationship between the spacing of the rigid surface elements and the apparent flexural modulus and compressive modulus of the system. According to the results from **Figure 46** in Section 4.2.2, the spacing of the elements has a great influence on the flexural modulus of the models; however, they exhibit very little influence over the compressive strength. Therefore, the spacing of the rigid surface elements can be manipulated and tailored to allow for the desired flexibility of the armor without having a major impact on the compressive modulus of the system. In addition, the spacing between elements could be varied in different regions of the armor to increase or decrease flexibility as desired for the application. Also, the variable file spacing has little influence over the stress distribution through the layers of the armor. Therefore, there is less worry of stress concentration and added risk of failure in the the different layers of this composite system.

The other result that could impact the field is the depth of the rigid elements in the system. Embedding the rigid tiles in the semi-rigid base raises the neutral axis of the system and subsequently raises the area moment of inertia for the system. This increase in the area moment of inertia results in decreased stress throughout the system when a force is applied normal to the surface of the tiles. The reduced stresses would reduce the likelihood of failure when compared to cases where the rigid tiles lie above or adjacent to the surface of the semi-rigid base.

5.6 FUTURE WORK

The work presented in this research provided a novel investigation of chondrichthyan dentitions as rigid patterned elements. Due to the novelty of this study, there remains a wide array of variables and testing methods that should be investigated to develop a complete understanding of the system.

Pending work includes investigating the effects of geometry on the system. A cylindrical beam was modeled using the same methods established in Section 3.1.3 with the dimensions seen in **Figure 51** and parameters in **Table 3**. The models were tested using the three-point bending methods outlined in Section 3.4.1, and the preliminary results were analyzed using **Eq. 4**, **Eq. 5**, and **Eq. 29**.

$$\sigma_f = \frac{PL}{\pi r^3}, \qquad \text{(Eq. 29)}$$

where σ_f*: flexural stress [MPa], P: load at a given point on the load-defection curve [N], L: span of support [mm], r: the average radius of the specimen (5.73 mm) [mm].*

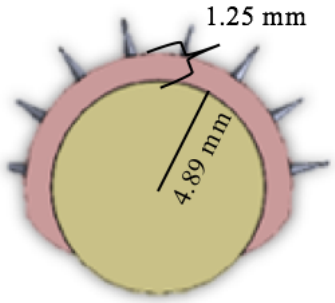

Figure 51: The cylindrical cross-section representative of the dorsal jaw region. The cross-section has a jaw radius of 4.89 mm and a dental ligament thickness of 1.25 mm that spans over a 22 mm arc length. These dimensions give the model the same total volume as the rectangular cross-section models.

These preliminary results, **Figure 52**, display the same trends that were seen in the rectangular beam in Chapter 4. Consequently, we expect to see the same general result for the stress distribution through the beams. The stress distribution will be calculated using the same basic process outlined in Section 3.6. However, the neutral axis and area moment of inertia will be calculated with **Eq. 30** and **Eq. 31**, respectively.

$$\bar{y} = \frac{\sum n_i \int y_i \, dA}{\sum n_i \int dA}, \qquad \text{(Eq. 30)}$$

$$y_i = r\sin(\theta)$$

$$dA = r \, dr \, d\theta$$

where $\bar{y}$*: neutral axis [mm],* y_i*: distance to the center of the model [mm], r: radius of each layer [mm],* θ*: angle [radians],* dA_i*: the area of the layer [mm*^{2}*]:* n_i*: scaling factor*

$$\bar{I} = \sum n_i (\overline{I_\iota} + A_i d_i^2) \ , \qquad \text{(Eq. 31)}$$

which is equivalent to: $\bar{I} = \sum n_i \int y_i^2 \, dA$

$$y_i = r\sin(\theta)$$

$$dA = r \, dr \, d\theta$$

where $\overline{I_\iota}$ *is the area-moment of inertia for each section [mm*^{4}*], r: radius of each layer [mm],* θ*: angle [radians],* dA_i*: the area of the layer,* n_i*: scaling factor*

Then, after gaining a better understanding of the contact mechanics of cylindrical beams, compression tests will be performed. Based on the results that are seen here, there is no evidence to support any variation in the trends. Therefore, we hypothesize that the

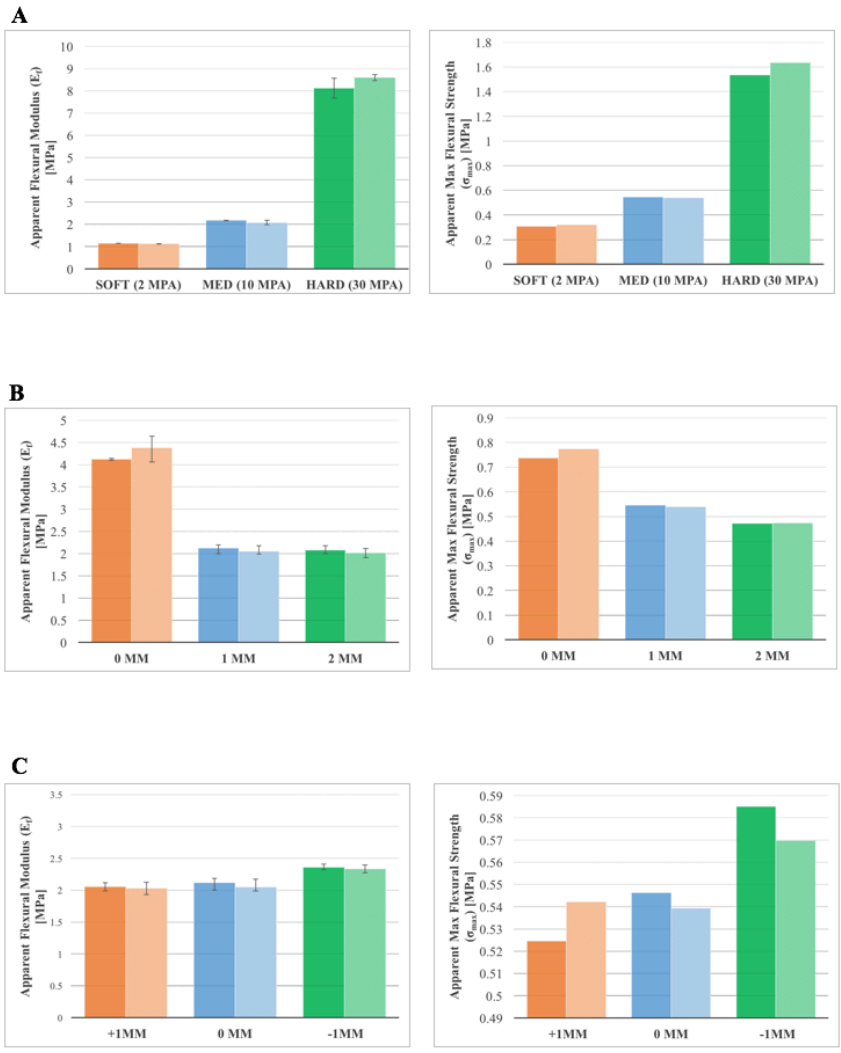

Figure 52: Preliminary results from the three-point bend of cylindrical models. There were three models tested for each combination of variables. The solid bars are the parallel dentition pattern, while the hashed (lighter colored) bars are the staggered dentition pattern. **A:** Apparent flexural modulus (left) and max flexural strength (right) for the variable representative jaw cartilage materials. **B:** Apparent flexural modulus (left) and max flexural strength (right) for the variable file spacing. **C:** Apparent flexural modulus (left) and max flexural strength (right) for the variable tooth depth.

cylindrical beams will also display the same trends in compression as the rectangular models.

Future work will begin with developing a system of equations better capable of approximating the apparent flexural and compressive moduli of this system. This model would need to account for the nonhomogeneous nature of the multicomponent layer, dentition patterning, and the compressive and tensile forces experienced during bending. The next step would be to run additional mechanical tests for the same variables tested in bending and compression. These additional tests will aim to gather data related to the wide array of forces the jaw is exposed to during feeding. Torsion testing, shear testing, and bending of the beam normal to the face of the teeth are all tests that should provide beneficial data and lead to a more complete understanding of the influences of dentition patterning. It is the ultimate goal to use the simplified beam models to determine the variables related to the patterning and orientation of the teeth that influence the properties of the feeding mechanism for use with engineering applications. Finally, after determining the influential variables, we would like to model them on the representative anatomical model described in Section 3.1.1. This would reintroduce variable tooth size and angle, and it should give a more accurate representation of how the variables influence a biological system.

REFERENCES:

1. Barthelat, F., 2015, "Architectured Materials in Engineering and Biology: Fabrication, Structure, Mechanics and Performance," International Materials Reviews, 60(8) pp. 413-430.

2. Wegst, U. G., Bai, H., Saiz, E., 2015, "Bioinspired Structural Materials," Nature Materials, 14(1) pp. 23-36.

3. Bar-Cohen, Y., 2005, "Biomimetics: biologically inspired technology," Pasadena, CA: Jet Propulsion Laboratory, National Aeronautics and Space Administration, .

4. Chen, P., McKittrick, J., and Meyers, M. A., 2012, "Biological Materials: Functional Adaptations and Bioinspired Designs," Progress in Materials Science, 57(8) pp. 1492-1704.

5. Porter, M. M., Ravikumar, N., Barthelat, F., 2016, "3D-Printing and Mechanics of Bio-Inspired Articulated and Multi-Material Structures," Journal of the Mechanical Behavior of Biomedical Materials, .

6. Studart, A. R., 2012, "Towards high-performance Bioinspired Composites," Advanced Materials, 24(37) pp. 5024-5044.

7. Chen, P., Schirer, J., Simpson, A., 2012, "Predation Versus Protection: Fish Teeth and Scales Evaluated by Nanoindentation," Journal of Materials Research, 27(01) pp. 100-112.

8. Naleway, S. E., Porter, M. M., McKittrick, J., 2015, "Structural Design Elements in Biological Materials: Application to Bioinspiration," Advanced Materials, 27(37) pp. 5455-5476.

9. Ritchie, R. O., 2011, "The Conflicts between Strength and Toughness," Nature Materials, 10(11) pp. 817-822.

10. Bar-On, B., and Wagner, H. D., 2013, "Structural Motifs and Elastic Properties of Hierarchical Biological tissues–A Review," Journal of Structural Biology, 183(2) pp. 149-164.

11. Dutta, A., and Tekalur, S. A., 2013, "Synthetic Staggered Architecture Composites," Materials & Design, 46pp. 802-808

12. Barthelat, F., Tang, H., Zavattieri, P., 2007, "On the Mechanics of Mother-of-Pearl: A Key Feature in the Material Hierarchical Structure," Journal of the Mechanics and Physics of Solids, 55(2) pp. 306-337.

13. Barthelat, F., and Espinosa, H., 2007, "An Experimental Investigation of Deformation and Fracture of nacre–mother of Pearl," Experimental Mechanics, 47(3) pp. 311-324.

14. Meyers, M. A., McKittrick, J., and Chen, P. Y., 2013, "Structural Biological Materials: Critical Mechanics-Materials Connections," Science (New York, N.Y.), 339(6121) pp. 773-779.

15. Sun, J., and Bhushan, B., 2012, "Hierarchical Structure and Mechanical Properties of Nacre: A Review," Rsc Advances, 2(20) pp. 7617-7632.

16. Aizenberg, J., Weaver, J. C., Thanawala, M. S., 2005, "Skeleton of Euplectella Sp.: Structural Hierarchy from the Nanoscale to the Macroscale," Science (New York, N.Y.), 309(5732) pp. 275-278.

17. Miserez, A., Weaver, J. C., Thurner, P. J., 2008, "Effects of Laminate Architecture on Fracture Resistance of Sponge Biosilica: Lessons from Nature," Advanced Functional Materials, 18(8) pp. 1241-1248.

18. Jackson, A., Vincent, J., and Turner, R., 1988, "The Mechanical Design of Nacre," Proceedings of the Royal Society of London B: Biological Sciences, 234(1277) pp. 415-440.

19. Bouligand, Y., 1972, "Twisted Fibrous Arrangements in Biological Materials and Cholesteric Mesophases," Tissue and Cell, 4(2) pp. 189192-190217.

20. Raabe, D., Sachs, C., and Romano, P., 2005, "The Crustacean Exoskeleton as an Example of a Structurally and Mechanically Graded Biological Nanocomposite Material," Acta Materialia, 53(15) pp. 4281-4292.

21. Wen, L., Weaver, J. C., and Lauder, G. V., 2014, "Biomimetic Shark Skin: Design, Fabrication and Hydrodynamic Function," The Journal of Experimental Biology, 217(Pt 10) pp. 1656-1666.

22. Wen, L., Weaver, J. C., Thornycroft, P. J., 2015, "Hydrodynamic Function of Biomimetic Shark Skin: Effect of Denticle Pattern and Spacing," Bioinspiration & Biomimetics, 10(6) pp. 066010.

23. Dean, M. N., and Summers, A. P., 2006, "Mineralized Cartilage in the Skeleton of Chondrichthyan Fishes," Zoology, 109(2) pp. 164-168.

24. Porter, M. E., Beltran, J. L., Kajiura, S. M., 2013, Stiffness without Mineral: Material Properties and Biochemical Components of Jaws and Chondrocrania in the Elasmobranchii (Sharks, Skates, and Rays), .

25. Whitenack, L. B., and Motta, P. J., 2010, "Performance of Shark Teeth during Puncture and Draw: Implications for the Mechanics of Cutting," Biological Journal of the Linnean Society, 100(2) pp. 271-286.

26. Moss, S. A., 1972, "The Feeding Mechanism of Sharks of the Family Carcharhinidae," Journal of Zoology, 167(4) pp. 423-436.

27. Ramsay, J. B., and Wilga, C. D., 2007, "Morphology and Mechanics of the Teeth and Jaws of white-spotted Bamboo Sharks (Chiloscyllium Plagiosum)," Journal of Morphology, 268(8) pp. 664-682.

28. Wroe, S., Huber, D., Lowry, M., 2008, "Three-dimensional Computer Analysis of White Shark Jaw Mechanics: How Hard can a Great White Bite?" Journal of Zoology, 276(4) pp. 336-342.

29. Whitenack, L. B., Simkins, D. C., Motta, P. J., 2010, "Young's Modulus and Hardness of Shark Tooth Biomaterials," Archives of Oral Biology, 55(3) pp. 203-209.

30. Liu, X., Dean, M. N., Youssefpour, H., 2014, "Stress Relaxation Behavior of Tessellated Cartilage from the Jaws of Blue Sharks," Journal of the Mechanical Behavior of Biomedical Materials, 29pp. 68-80.

31. Huber, D. R., Eason, T. G., Hueter, R. E., 2005, "Analysis of the Bite Force and Mechanical Design of the Feeding Mechanism of the Durophagous Horn Shark Heterodontus Francisci," The Journal of Experimental Biology, 208(Pt 18) pp. 3553-3571.

32. Moyer, J. K., Riccio, M. L., and Bemis, W. E., 2015, "Development and Microstructure of Tooth Histotypes in the Blue Shark, Prionace Glauca (Carcharhiniformes: Carcharhinidae) and the Great White Shark, Carcharodon Carcharias (Lamniformes: Lamnidae)," Journal of Morphology, 276(7) pp. 797-817.

33. Dean, M. N., Ramsay, J. B., and Schaefer, J. T., 2008, "Tooth Reorientation Affects Tooth Function during Prey Processing and Tooth Ontogeny in the Lesser Electric Ray, Narcine Brasiliensis," Zoology,111(2) pp. 123-134.

34. Powlik JJ. 1995. On the geometry and mechanics of tooth position in the white shark. Carcharodon carcharias. J Morphol 226:277–288.

35. Frazzetta TH, Prange CD. 1987. Movements of cephalic components during feeding in some requiem sharks (Carchariformes:Carcharhinidae). Copeia 4:979–993.

36. Williams, M.E., 2001. Tooth retention in cladodont sharks: with a comparison between primitive grasping and swallowing, and modern cutting and gouging feeding mechanisms. J. Vert. Paleontol. 21, 214–226.

37. Ferrara, T., Clausen, P., Huber, D., 2011, "Mechanics of Biting in Great White and Sandtiger Sharks," Journal of Biomechanics, 44(3) pp. 430-435.

38. Summers, A. P., 2000, "Stiffening the Stingray Skeleton - an Investigation of Durophagy in Myliobatid Stingrays (Chondrichthyes, Batoidea, Myliobatidae)," Journal of Morphology, 243(2) pp. 113-126.

39. Ashhurst, D. E., 2004. The cartilaginous skeleton of an elasmobranch fish does not heal. Matrix Bio. 23, 15-22.

40. Myers, E. R. & Mow, V. C., 1983. Biomechanics of cartilage and its response to biomechanical stimuli. Cartilage, Academic Press, New York, pp. 313–314.

41. Poole, C. A., 1992. The structure and function of articular cartilage matrices. In Joint Cartilage Degradation, Basic and Clinical Aspects, vol. (ed.^eds. Woessner, J. F., Jr. &Howell, D. S.). New York. pp. 1-35.

42. Kemp, N. E., and Westrin, S. K., 1979, "Ultrastructure of Calcified Cartilage in the Endoskeletal Tesserae of Sharks," Journal of Morphology, 160(1) pp. 75-101.

43. Summers, A. P., and Long, J. H., 2005, "Skin and Bones, Sinew and Gristle: The Mechanical Behavior of Fish Skeletal Tissues," Fish Physiology, 23pp. 141-177.

44. France, R.C., 2009, "Introduction to Physical Education and Sport Science,"Delmar, Cengage Learning, pp. 59.

45. Phulari, B.S., 2011, "Orthodontics: Principles and Practice,"Jaypee Brothers Medical Publishers (P) Ltd, New Delhi, pp. 129.

46. Shellis, R.P., 1982. Comparative anatomy of tooth attachment. In: Berkowitz, B.K.B., Maxham, B.J., Newman, H.N. (Eds.), The Periodontal Ligament in Health and Disease. Pergamon Press, pp. 3–24.

47. Enax, J., Prymak, O., Raabe, D., 2012, "Structure, Composition, and Mechanical Properties of Shark Teeth," Journal of Structural Biology, 178(3) pp. 290-299.

48. Bertin L. 1958. Denticules Cutan_es et Dentes. In: Grass_e P, editor. Trait_e de Zoologie: Anatomie, Syst_ematique, Biologie. Tome XIII, Agnathes et Poissons, Anatomie, _Ethologie, Syst_ematique. Paris: Masson et Cie. pp 505–531.

49. Cappetta H. 2012. Handbook of Paleoichthyology: Chondrichthyes.—Mesozoic and Cenozoic Elasmobranchii: Teeth, Vol. 3E. In: Schultze H-P, editor. Munich: Pfeil. 512 p.

50. Wroe, S., Moreno, K., Clausen, P., 2007, "High-Resolution Three-Dimensional Computer Simulation of Hominid Cranial Mechanics," The Anatomical Record, 290(10) pp. 1248-1255.

51. McHenry, C. R., Wroe, S., Clausen, P. D., 2007, "Supermodeled Sabercat, Predatory Behavior in Smilodon Fatalis Revealed by High-Resolution 3D Computer Simulation," Proceedings of the National Academy of Sciences of the United States of America, 104(41) pp. 16010-16015.

52. Chen, J., Ahmad, R., Li, W., 2015, "Biomechanics of Oral Mucosa," Journal of the Royal Society, Interface, 12(109) pp. 20150325.

53. ASTM D638-14 Standard Test Method for Tensile Properties of Plastics, ASTM International, West Conshohocken, PA, 2014

54. Stratasys Digital Materials Data Sheet, Stratasys, Ltd. Eden Prairie, MN, http://usglobalimages.stratasys.com/Main/Files/Material_Spec_Sheets/MSS_PJ_DigitalMaterialsDataSheet.pdf?v=635796522191362278, Oct. 24, 2016

55. Destrade, M., Murphy, J. G., and Rashid, B., 2013, "Differences in Tension and Compression in the Nonlinearly Elastic Bending of Beams," ArXiv Preprint arXiv:1303.1901.

56. ASTM D790-03, Standard Test Methods for Flexural Properties of Unreinforced and Reinforced Plastics and Electrical Insulating Materials, ASTM International, West Conshohocken, PA, 2003

57. Jayasankar, A., Seidel, R., Naumann, J., 2017, "Mechanical Behavior of Idealized, Stingray-Skeleton-Inspired Tiled Composites as a Function of Geometry and Material Properties," Journal of the Mechanical Behavior of Biomedical Materials, .

58. McNeil, B., Lowry, D., Larson, S., 2016, "Feeding Behavior of Subadult Sixgill Sharks (Hexanchus Griseus) at a Bait Station," PloS One, 11(5) pp. e0156730.

59. Norton, S. F., and Brainerd, E. L., 1993, "Convergence in the Feeding Mechanics of Ecomorphologically Similar Species in the Centrarchidae and Cichlidae," Journal of Experimental Biology, 176(1) pp. 11-29.

60. Motta, P., Tricas, T., and Summers, R., 1997, "Feeding Mechanism and Functional Morphology of the Jaws of the Lemon Shark Negaprion Brevirostris (Chondrichthyes, Carcharhinidae)," The Journal of Experimental Biology, 200(Pt 21) pp. 2765-2780.

61. Ferry-Graham, L., 1997, "Feeding Kinematics of Juvenile Swellsharks, Cephaloscyllium Ventriosum," The Journal of Experimental Biology, 200(Pt 8) pp. 1255-1269.

62. Wilga, C., and Motta, P., 1998, "Conservation and Variation in the Feeding Mechanism of the Spiny Dogfish Squalus Acanthias," The Journal of Experimental Biology, 201 (Pt 9)(Pt 9) pp. 1345-1358.

63. Barclift, M. W., and Williams, C. B., 2012, "Examining variability in the mechanical properties of parts manufactured via polyjet direct 3D printing," International Solid Freeform Fabrication Symposium, August, Anonymous pp. 6-8.

64. Beltrán, N., Carriles, F., Álvarez, B., 2015, "Characterization of Factors Influencing Dimensional and Geometric Errors in PolyJet Manufacturing of Cylindrical Features," Procedia Engineering, 132pp. 62-69.

65. Yang, W., Naleway, S. E., Porter, M. M., 2015, "The Armored Carapace of the Boxfish," Acta Biomaterialia, 23pp. 1-10.

66. Shao, C., and Keten, S., 2015, "Stiffness Enhancement in Nacre-Inspired Nanocomposites due to Nanoconfinement," Scientific Reports, 5pp. 16452.